MANEUVER AND CONTROL OF FLEXIBLE SPACECRAFT

by

Roger D. Quinn

Dissertation submitted to the faculty of the

Virginia Polytechnic Institute and State University

in partial fulfillment of the requirements for the degree of

DOCTOR OF PHILOSOPHY

in

Engineering Mechanics

APPROVED:

L. Meirovitch, Chairman

J. N. Reddy

L. G. Kraige

J. F. VanLandingham

S. L. Hendricks

December, 1985

Blacksburg, Virginia

MANEUVER AND CONTROL OF FLEXIBLE SPACECRAFT

by

Roger D. Quinn

Committee Chairman: L. Meirovitch

Engineering Mechanics

(ABSTRACT)

This dissertation is concerned with the problem of slewing large flexible structures in space and simultaneously suppressing any vibrations. The equations of motion for a three-dimensional spacecraft undergoing large rigid-body maneuvers are derived. The elastic motions are assumed to remain in the linear range. A method of substructure synthesis is presented which spatially discretizes the equations of motion. A perturbation approach is used to solve the equations of motion. The zero-order equations describing the rigid-body maneuver are independent of the first-order vibration problem which includes small rigid-body motions. The vibration problem is described by linear nonself-adjoint equations with time-dependent coefficients. Minimum-time, single-axis rotational maneuvers are considered. The axis of rotation is not necessarily a principal axis. The optimal maneuver force distribution is proportional to the corresponding rigid-body modes with the mass acting as the control gain. The premaneuver eigenvectors are used as admissible vectors to reduce the degrees of freedom describing the vibration of the spacecraft during the maneuver. Natural control and uniform damping control are used to suppress the vibrations

during the maneuver. Actuator dynamics cause a degradation of control performance. The inclusion of the actuator dynamics in the control formulation partially offsets this effect. The performance of these control techniques is adversely affected by actuator saturation but they remain effective. Numerical results are presented for a spacecraft in orbit and in an earth-based laboratory.

ACKNOWLEDGMENTS

I am deeply indebted to Professor Leonard Meirovitch for the many opportunities, guidance and support he has provided me in the course of my graduate studies at V.P.I. All of his labor on my behalf is most sincerely appreciated.

I am grateful to Drs. J. N. Reddy, L. G. Kraige, H. F. VanLandingham and S. L. Hendricks for serving on my examining committee and for their review of this dissertation. I would also like to thank Drs. J. L. Junkins and D. T. Mook for serving on my preliminary examination committee.

To , my beloved wife, I cannot begin to express my appreciation for her patience and emotional support.

My thanks extend to my friends, especially and , for the beneficial discussions and pleasant times we shared. Last but not least, I would like to thank and for their patience in typing this dissertation.

TABLE OF CONTENTS

LIST OF FIGURES

LIST OF TABLES

CHAPTER I

INTRODUCTION

1.1 PRELIMINARY REMARKS

This dissertation is concerned with the problem of slewing a large flexible structure in space. Maneuvering of a spacecraft causes elastic motion for which vibration control may be necessary. The main purposes of this dissertation are to demonstrate the vibrations caused by rotational maneuvers of a flexible spacecraft and to develop ways of suppressing these undesirable motions by means of active control.

The placing of a large space station in an earth orbit is planned for the next decade. To minimize lifting expenses, this structure must be designed with a minimum of mass, and hence with a significant degree of flexibility, making it susceptible to vibration problems. Active control will be necessary to maneuver the spacecraft as well as to contain the ensuing vibrations within acceptable levels.

The National Aeronautics and Space Administration (NASA) is conducting two experimental programs to test techniques for active vibration suppression of space structures. Ground-based experimentation, such as the Spacecraft Control Laboratory Experiment (SCOLE), has its limitations because it is almost impossible to duplicate the space environment in a laboratory. The Control Of Flexible Spacecraft (COFS) project involves experiments consisting of the control of flexible bodies carried by a shuttle in an earth orbit. The same project also includes laboratory simulations of similar experiments, which will precede the space experiments. Actually, these

programs are extensions of previous experimentation (Ref. 22). Testing a control scheme in space is expensive and deploying an unproven system could be disastrous. Hence, computer modeling and simulation is valuable to the success of both SCOLE and COFS, as well as to aid in the design of a space station and the corresponding control systems.

1.2 LITERATURE SURVEY

Turner and Junkins presented a paper concerning single-axis rotational maneuvering and simultaneous vibration suppression of flexible spacecraft (Ref. 26). Independently, Breakwell addressed the same problem in a similar manner, extended the method to include feedback control and offered experimental verification (Ref. 4). The problem formulation and solution technique is an extended version of the method first used by Junkins and Turner for the maneuvering of rigid spacecraft (Ref. 8). The model of the flexible spacecraft considered in Ref. 26 consisted of a rigid hub with four identical elastic beams attached symmetrically about the hub. A single torque-producing actuator was located at the hub. Turner and Chun extended the results to a two input system by adding torquers, which obeyed the same control law, at the midpoints of each appendage (Ref. 27). In all cases, elastic motion was restricted to the plane normal to the axis of rotation and only antisymmetric deformation modes were considered. Hence, centrifugal disturbance forces were precluded, leaving only tangential forces to excite the elastic modes. Turner extended the formulation to include three dimensional motion but numerical difficulties prevented a solution (Ref. 25).

The problem formulation included terminal constraints so that all controlled modes ceased motion at the final time. These constraints tended to take precedence over the vibration suppression during the maneuver as shown by the results in the cited papers. The numerical difficulties encountered in solving the associated two point boundary value problem for systems of increasing order are pointed out by Breakwell. More efficient numerical methods, suggested by Junkins in a technical note, extend the applicability of the method but the difficulties for higher-order systems remain (Ref. 9).

The terminal constraints are not necessary if the vibration is suppressed during the maneuver. Removal of these constraints permits separation of the control problem into two problems, maneuver control and vibration suppression. Baruh and Silverberg first suggested this solution method (Ref. 3). Their technique was also applied to a simple model which did not include the dynamic effects considered here. Although a number of extra actuators were required, equal to the number of rigid-body modes, the rigid-body modes were not included in the closed-loop, vibration control.

The equations of motion governing the maneuvering of a rigid-body are well known (Refs. 8, 12). Also, the equations of motion governing the vibrational motion of a flexible body have received considerable attention in the literature (Refs. 6, 13). On the other hand, the equations governing the motion of a flexible spacecraft during a maneuver are not as well documented, being available only for special cases (Refs. 3, 4, 26).

1.3 OUTLINE

The object of Chapter 2 is to produce the equations of motion of a maneuvering flexible spacecraft which are useful both for modeling ground based experiments and orbiting spacecraft. To this end, Lagrange's equations of motion are first derived for the spacecraft of Fig. 2.1 regarding the structure as orbiting around the earth, and then modified so as to describe the laboratory experiment of Fig. 2.2. In the derivation, the shuttle is treated as a rigid body and the mast and antenna as flexible, distributed-parameter members.

The equations describing the motion of a rigid spacecraft are nonlinear ordinary differential equations. On the other hand, the equations describing the small elastic displacements of a flexible spacecraft relative to a frame embedded in the undeformed spacecraft are linear partial differential equations. Hence, the complete equations describing a flexible spacecraft during a certain maneuver represent a set of nonlinear hybrid differential equations.

In general, hybrid systems of equations do not permit closed-form solution, so that one must consider an approximate solution, which implies truncation. Spatial discretization and truncation can be carried out by representing the motion in terms of a finite set of admissible functions, which is done in Chapter 2 (Ref. 13). Substructure synthesis proves useful as a method of discretization and truncation to aid in the premaneuver eigensolution (Refs. 5, 13). A subset of the premaneuver eigenvectors can then be used as admissible vectors during the maneuver to further reduce the number of degrees of

freedom of the model. Chapter 4 contains a development of substructure synthesis as well as an original and efficient method of substructure assembly. For future reference, the linear model is generalized in this chapter to allow for multiple appendages. It is shown that the nonlinear model can also easily be generalized to include multiple appendages. An INTELSAT satellite is modeled to demonstrate the method of substructure synthesis.

The discretized equations of motion of a spacecraft during a maneuver are nonlinear, even when the elastic deformations are in the linear range. The nonlinear terms result from the large rigid-body motions. A first-order perturbation approach is introduced in Chapter 3 to solve the equations of motion. This technique amounts to transforming the equations of motion into a set of zero-order equations governing the rigid-body motions and a set of first-order time-varying linear equations governing small elastic motions and deviations from the prescribed rigid-body maneuver. The perturbation technique permits a maneuver strategy that is independent of the elastic analysis. Regarding the rigid-body maneuver as known, the perturbation equations for the vibration control reduce to a set of linear ordinary differential equations with known time-varying coefficients.

An open-loop control strategy for minimum-time, single-axis rotational maneuvers of a rigid body is discussed in Chapter 5. The control strategy is first developed for continuous time and then adapted to discrete-time control. The analysis considers actuator dynamics.

The force distribution, which produces the moment required for the maneuver, is discussed for the case of a flexible structure.

In Chapter 6, the premaneuver eigenvectors are used as admissible vectors to reduce the order of the perturbation equations. These eigenvectors do not decouple the equations of motion, but they do diagonalize the mass matrix for the situations of interest. Hence, the inversion of the reduced-order mass matrix is trivial and the formulation of the equations in state-space form can be carried out with little effort. The time-dependent coefficient matrices are simplified by making use of the fact that the maneuvers of interest are single-axis rotations.

Chapter 7 deals with the computation and application of control forces that suppress the vibration caused by the maneuver and other disturbance forces. Optimal control techniques are discussed along with pole placement methods. Inclusion of the actuator's dynamics along with the structure's dynamics for control force computation is found to be beneficial. In fact, all of the control techniques presented are adapted to include actuator dynamics. The premaneuver eigenvectors are used as admissible vectors for control formulation as they were for simulation. Shape control, which is needed to oppose large steady-state disturbance forces, is also discussed.

Chapter 8 contains numerical results demonstrating the maneuver formulation of Chapter 5, the simulation technique of Chapter 6 and the control techniques of Chapter 7. The SCOLE configuration (as of 9/85) is used as the model for these computations.

Chapter 9 contains summaries of the solution techniques, the numerical results and the conclusions. Also, recommendations are included to help assure the success of the SCOLE project and for future work.

CHAPTER II

DERIVATION OF THE EQUATIONS OF MOTION

2.1 INTRODUCTION

In this chapter, Lagrange's equations of motion are first derived for the spacecraft of Fig. 2.1 regarding the structure as orbiting about the earth and then modified so as to describe the laboratory experiment of Fig. 2.2. In the derivation, the shuttle is treated as a rigid-body and the mast and antenna as flexible, distributed-parameter members.

The equations describing the motion of a rigid spacecraft are nonlinear ordinary differential equations. On the other hand, the equations describing the small elastic displacements of a flexible spacecraft relative to a frame embedded in the undeformed spacecraft are linear partial differential equations. Hence, the complete equations of motion describing a flexible spacecraft during a certain maneuver represent a set of nonlinear hybrid differential equations.

In general hybrid systems of equations do not permit closed-form solution, so that one must consider an approximate solution, which implies truncation. Spatial discretization and truncation can be carried out by representing the motion in terms of admissible functions. Chapter 4 contains a variation on a discretization procedure representing a type of discrete substructure synthesis.

2.2 Equations of Motion of the Spacecraft

It is convenient to refer the motion of the spacecraft to a given reference frame $x_0y_0z_0$, where the frame can be regarded as being

embedded in the rigid shuttle. The reference frame has six degrees of freedom, three rigid-body translations and three rigid-body rotations.

We propose to derive the equations of motion by means of the Lagrangian approach. To this end, we must first obtain expressions for the kinetic energy, the potential energy and the virtual work. Considering Fig. 2.1 and denoting the position of the origin O of the frame $x_0y_0z_0$ by the vector $\underset{\sim}{R}$ and the position of a point S in the shuttle relative to O by $\underset{\sim}{r}$, the position of S relative to the inertial frame XYZ is $\underset{\sim}{R}_S = \underset{\sim}{R} + \underset{\sim}{r}$. Moreover, denoting by $\underset{\sim}{a}$ the vector from O to a nominal point A on the appendage and by $\underset{\sim}{u}$ the elastic displacement vector of the point, the position of A in the displaced configuration is $\underset{\sim}{R}_A = \underset{\sim}{R} + \underset{\sim}{a} + \underset{\sim}{u}$. It must be noted that the vectors $\underset{\sim}{r}$, $\underset{\sim}{a}$ and $\underset{\sim}{u}$ are likely to be measured relative to axes $x_0y_0z_0$. In view of the above, the velocity of a point S in the shuttle is

$$\dot{\underset{\sim}{R}}_S = \dot{\underset{\sim}{R}} + \underset{\sim}{\omega} \times \underset{\sim}{r} \tag{2.1}$$

where $\dot{\underset{\sim}{R}}$ is the translational velocity and $\underset{\sim}{\omega}$ is the angular velocity of the frame $x_0y_0z_0$ with respect to the inertial frame. Similarly, the velocity of a point A in the appendage is

$$\dot{\underset{\sim}{R}}_A = \dot{\underset{\sim}{R}} + \underset{\sim}{\omega} \times (\underset{\sim}{a} + \underset{\sim}{u}) + \dot{\underset{\sim}{u}} \tag{2.2}$$

where $\dot{\underset{\sim}{u}}$ is the elastic velocity of the point relative to the $x_0y_0z_0$ frame. Hence, the kinetic energy of the spacecraft is

$$T = \frac{1}{2}\int_{m_S} |\dot{\underset{\sim}{R}}_S|^2 dm_S + \frac{1}{2}\int_{m_A} |\dot{\underset{\sim}{R}}_A|^2 dm_A$$

$$= \frac{1}{2}\int_{m_S} |\dot{\underset{\sim}{R}} + \underset{\sim}{\omega} \times \underset{\sim}{r}|^2 dm_S + \frac{1}{2}\int_{m_A} |\dot{\underset{\sim}{R}} + \underset{\sim}{\omega} \times (\underset{\sim}{a} + \underset{\sim}{u}) + \dot{\underset{\sim}{u}}|^2 dm_A$$

$$= \frac{1}{2} m|\dot{\underset{\sim}{R}}|^2 + \frac{1}{2}\underset{\sim}{\omega}^T I_0 \underset{\sim}{\omega} + \dot{\underset{\sim}{R}}\cdot(\underset{\sim}{\omega} \times \underset{\sim}{S}_0) + \frac{1}{2}\int_{m_A} |\dot{\underset{\sim}{u}}|^2 dm_A$$

$$+ \dot{\underset{\sim}{R}}\cdot\left[\int_{m_A} \dot{\underset{\sim}{u}}\, dm_A + \underset{\sim}{\omega} \times \int_{m_A} \underset{\sim}{u}\, dm_A\right] + \int_{m_A} \dot{\underset{\sim}{u}}\cdot(\underset{\sim}{\omega} \times \underset{\sim}{a}) dm_A$$

$$+ \int_{m_A} (\underset{\sim}{\omega} \times \underset{\sim}{a})\cdot(\underset{\sim}{\omega} \times \underset{\sim}{u}) dm_A + \frac{1}{2}\int_{m_A} |\underset{\sim}{\omega} \times \underset{\sim}{u}|^2 dm_A$$

$$+ \int_{m_A} \dot{\underset{\sim}{u}}\cdot(\underset{\sim}{\omega} \times \underset{\sim}{u}) dm_A \qquad (2.3)$$

where

$$\underset{\sim}{S}_0 = \int_{m_S} \underset{\sim}{r}\, dm_S + \int_{m_A} \underset{\sim}{a}\, dm_A \qquad (2.4)$$

and m_S, m_A and m are the masses of the shuttle, the appendage and the entire spacecraft, respectively. Also, I_0 is the total mass moment of inertia matrix of the undeformed structure about point O. Note that $|\underset{\sim}{x}|^2$ denotes the inner product $\underset{\sim}{x}\cdot\underset{\sim}{x}$.

The potential energy is due to the combined effects of gravity and strain energy. Assuming that the origin of the inertial coordinate system coincides with the center of the gravitational field, the gravitational potential can be expressed as

$$V_g = -Gm_e\left[\int_{m_S} |\underset{\sim}{R} + \underset{\sim}{r}|^{-1} dm_S + \int_{m_A} |\underset{\sim}{R} + \underset{\sim}{a} + \underset{\sim}{u}|^{-1} dm_A\right] \qquad (2.5)$$

where m_e is the mass of the earth and G is the universal gravitational constant.

The strain energy can be expressed as an energy inner product denoted by [,] (Ref. 13). This includes the potential energy which is a function of the first spatial derivative of the elastic displacement $\underset{\sim}{u}'$. Hence, both centrifugal and gravitational stiffening effects are included in the elastic energy. The total potential energy then becomes

$$V = \frac{1}{2}[\underset{\sim}{u},\underset{\sim}{u}] + V_g \tag{2.6}$$

The virtual work is due to external forces, including control forces. Denoting by $\underset{\sim}{f}_S$ the force vector per unit volume of the shuttle and by $\underset{\sim}{f}_A$ the force vector per unit volume of the appendage, we can write the virtual work as

$$\delta W = \int_{D_S} \underset{\sim}{f}_S \cdot \delta \underset{\sim}{R}_S \, dD_S + \int_{D_A} \underset{\sim}{f}_A \cdot \delta \underset{\sim}{R}_A \, dD_A \tag{2.7}$$

where D_S and D_A are the domains of the shuttle and appendage, respectively.

Next, we propose to discretize the system in space. To this end, we express the elastic displacements in the form of linear combinations of admissible functions, or

$$\underset{\sim}{u} = \Phi \underset{\sim}{q} \tag{2.8}$$

where Φ is a matrix of space-dependent admissible functions and $\underset{\sim}{q}$ is a vector of time-dependent generalized coordinates. Introducing Eq. (2.8) into Eq. (2.3), the kinetic energy takes the matrix form

$$T = \frac{1}{2} m \dot{\underset{\sim}{R}}^T \dot{\underset{\sim}{R}} + \frac{1}{2} \underset{\sim}{\omega}^T I_O \underset{\sim}{\omega} + \dot{\underset{\sim}{R}}^T C^T \tilde{S}_O \underset{\sim}{\omega} + \frac{1}{2} \dot{\underset{\sim}{q}}^T M_A \dot{\underset{\sim}{q}} + \dot{\underset{\sim}{R}}^T C^T \bar{\Phi} \dot{\underset{\sim}{q}} + \dot{\underset{\sim}{R}}^T C^T \tilde{\omega}^T \bar{\Phi} \underset{\sim}{q}$$

$$+ \dot{\underset{\sim}{q}}^T \bar{\Phi}^T \underset{\sim}{\omega} + \underset{\sim}{\omega}^T \int_{m_A} \tilde{a}^T \tilde{\omega}^T \Phi \, dm_A \underset{\sim}{q} - \frac{1}{2} \underset{\sim}{q}^T \bar{L}_A(\underset{\sim}{\omega}) \underset{\sim}{q} + \dot{\underset{\sim}{q}}^T \tilde{L}_A(\underset{\sim}{\omega}) \underset{\sim}{q} \tag{2.9}$$

where

$$\bar{\Phi} = \int_{m_A} \Phi \, dm_A, \quad \tilde{\Phi}^T = \int_{m_A} \Phi^T \tilde{a} \, dm_A \tag{2.10a,b}$$

$$\tilde{L}_A(\underset{\sim}{\omega}) = \int_{m_A} \Phi^T \tilde{\omega}^T \Phi \, dm_A, \quad \bar{L}_A(\underset{\sim}{\omega}) = \int_{m_A} \Phi^T \tilde{\omega}^2 \Phi \, dm_A \tag{2.10c,d}$$

and

$$M_A = \int_{m_A} \Phi^T \Phi \, dm_A \tag{2.10e}$$

is the mass matrix of the appendage. The symbol C represents a rotation matrix from the inertial frame XYZ to the $x_0y_0z_0$ frame and its elements are nonlinear functions of Euler's angles $\underset{\sim}{\alpha}$. The tilde over a typical vector $\underset{\sim}{v}$ denotes a skew symmetric matrix of the form

$$\tilde{v} = \begin{bmatrix} 0 & v_z & -v_y \\ -v_z & 0 & v_x \\ v_y & -v_x & 0 \end{bmatrix} \tag{2.11}$$

Recognizing that the magnitude of $\underset{\sim}{R}$ is large and $\underset{\sim}{u}$ is small in comparison with the other vectors in Eq. (2.5) and ignoring terms of order higher than three, a binomial expansion permits us to write

$$V_g \cong - Gm_e\left[m|\underset{\sim}{R}|^{-1} - \underset{\sim}{R}\cdot(\underset{\sim}{S}_0 + \int_{m_A} \underset{\sim}{u} \, dm_A)|\underset{\sim}{R}|^{-3}\right] \tag{2.12}$$

Introducing Eq. (2.12) into Eq. (2.6) and considering Eq. (2.8), the potential energy can be written in the form

$$V = \frac{1}{2}\underset{\sim}{q}^T K_A \underset{\sim}{q} - \frac{Gm_e m}{|\underset{\sim}{R}|} + \frac{Gm_e}{|\underset{\sim}{R}|^3}\underset{\sim}{R}^T C^T(\underset{\sim}{S}_0 + \bar{\Phi}\underset{\sim}{q}) \tag{2.13}$$

where

$$K_A = [\Phi, \Phi] \tag{2.14}$$

is the stiffness matrix of the appendage. The virtual work can be shown to have the expression

$$\delta W = \underset{\sim}{F}^T C \delta \underset{\sim}{R} + \underset{\sim}{M}^T D(\underset{\sim}{\alpha}) \delta \underset{\sim}{\alpha} + \underset{\sim}{Q}^T \delta \underset{\sim}{q} \tag{2.15}$$

where

$$\underset{\sim}{F} = \int_{D_S} \underset{\sim}{f}_S \, dD_S + \int_{D_A} \underset{\sim}{f}_A \, dD_A \tag{2.16a}$$

$$\underset{\sim}{M} = \int_{D_S} \tilde{r}^T \underset{\sim}{f}_S \, dD_S + \int_{D_A} \tilde{a}^T \underset{\sim}{f}_A \, dD_A + \int_{D_A} \tilde{f}_A \Phi \, dD_A \underset{\sim}{q} \tag{2.16b}$$

$$\underset{\sim}{Q} = \int_{D_A} \Phi^T \underset{\sim}{f}_A \, dD_A \tag{2.16c}$$

are generalized force vectors in terms of components about x_0, y_0 and z_0 and $D(\underset{\sim}{\alpha})$ is a matrix of trigonometric functions of the Euler angles defined by the expression

$$\underset{\sim}{\omega} = D(\underset{\sim}{\alpha}) \dot{\underset{\sim}{\alpha}} \tag{2.16d}$$

Lagrange's equations of motion can be written in the symbolic form

$$\frac{d}{dt} \left(\frac{\partial T}{\partial \dot{\underset{\sim}{R}}} \right) + \frac{\partial V}{\partial \underset{\sim}{R}} = C^T \underset{\sim}{F} \tag{2.17a}$$

$$\frac{d}{dt} \left(\frac{\partial T}{\partial \dot{\underset{\sim}{\alpha}}} \right) - \frac{\partial T}{\partial \underset{\sim}{\alpha}} + \frac{\partial V}{\partial \underset{\sim}{\alpha}} = D^T \underset{\sim}{M} \tag{2.17b}$$

$$\frac{d}{dt} \left(\frac{\partial T}{\partial \dot{\underset{\sim}{q}}} \right) - \frac{\partial T}{\partial \underset{\sim}{q}} + \frac{\partial V}{\partial \underset{\sim}{q}} = \underset{\sim}{Q} \tag{2.17c}$$

so that, considering Eqs. (2.9), (2.13) and (2.15) and premultiplying Eq. (2.17b) by D^{-T}, the equations of motion for the spacecraft in orbit are

$$m\ddot{\underset{\sim}{R}} + C^T\tilde{S}_0\dot{\underset{\sim}{\omega}} + C^T\bar{\Phi}\ddot{\underset{\sim}{q}} + C^T\tilde{\omega}^T\tilde{S}_0\underset{\sim}{\omega} + 2C^T\tilde{\omega}^T\bar{\Phi}\dot{\underset{\sim}{q}} + C^T(\tilde{\omega}^2 + \dot{\tilde{\omega}}^T)\bar{\Phi}\underset{\sim}{q}$$

$$+ \frac{Gm_e}{|\underset{\sim}{R}|^3}\{m\underset{\sim}{R} + C^T(\underset{\sim}{S}_0 + \bar{\Phi}\underset{\sim}{q}) - 3[\hat{\underset{\sim}{R}}\,\hat{\underset{\sim}{R}}^T\,C^T(\underset{\sim}{S}_0 + \bar{\Phi}\underset{\sim}{q})]\} = C^T\underset{\sim}{F} \quad (2.18a)$$

$$I_0\dot{\underset{\sim}{\omega}} + \tilde{\omega}^T I_0\underset{\sim}{\omega} + \tilde{S}_0^T C\ddot{\underset{\sim}{R}} + \tilde{\Phi}\ddot{\underset{\sim}{q}} + [\widetilde{[C\ddot{\underset{\sim}{R}}]}\bar{\Phi} + J(\dot{\underset{\sim}{\omega}}) + \tilde{\omega}^T J(\underset{\sim}{\omega}) + \frac{Gm_e}{|\underset{\sim}{R}|^3}\widetilde{[C\underset{\sim}{R}]}\bar{\Phi}]\underset{\sim}{q}$$

$$+ [\tilde{\omega}^T\tilde{\Phi} + J(\underset{\sim}{\omega})]\dot{\underset{\sim}{q}} + \frac{Gm_e}{|\underset{\sim}{R}|^3}\widetilde{[C\underset{\sim}{R}]}\underset{\sim}{S}_0 = \underset{\sim}{M} \quad (2.18b)$$

$$M_A\ddot{\underset{\sim}{q}} + \bar{\Phi}^T C\ddot{\underset{\sim}{R}} + \tilde{\Phi}^T\dot{\underset{\sim}{\omega}} + \int_{m_A}\Phi^T\tilde{\omega}^T\tilde{a}\underset{\sim}{\omega}\,dm_A + \frac{Gm_e}{|\underset{\sim}{R}|^3}\bar{\Phi}^T C\underset{\sim}{R}$$

$$+ \tilde{L}_A(\underset{\sim}{\omega})\dot{\underset{\sim}{q}} + [\bar{L}_A(\underset{\sim}{\omega}) + \tilde{L}_A(\dot{\underset{\sim}{\omega}}) + K_A]\underset{\sim}{q} = \underset{\sim}{Q} \quad (2.18c)$$

where

$$J(\underset{\sim}{\omega}) = \int_{m_A}(\tilde{a}\tilde{\omega} + \widetilde{[\tilde{a}\underset{\sim}{\omega}]})\Phi\,dm_A \quad (2.18d)$$

and

$$\hat{\underset{\sim}{R}} = \frac{\underset{\sim}{R}}{|\underset{\sim}{R}|} \quad (2.18e)$$

Premultiplying Eq. (2.17b) by D^{-T} is equivalent to considering Lagrange's equations in terms of quasi-coordinates (Ref. 12). Note that the position vector $\underset{\sim}{R}$, its time derivatives, and the Euler angles $\underset{\sim}{\alpha}$ have been considered to be of arbitrary magnitude, with the result that many nonlinear terms appear in Eqs. (2.18).

2.3. Equations of Motion for the Laboratory Experiment

In the laboratory experiment, the spacecraft is not actually free in space, but suspended from the ceiling by means of a cable or a beam. The following analysis applies to either case. The support is likely to affect the dynamic characteristics of the system. Hence, in the sequel, the support is added to the free model in the form of an elastic member.

Considering Fig. 2.2, the position vector for an arbitrary point C on the cable is $\underset{\sim}{R}_C = \underset{\sim}{c} + \underset{\sim}{w}$, where $\underset{\sim}{c}$ is a position vector and $\underset{\sim}{w}$ is the elastic displacement of the cable, both of which are measured with respect to the inertial frame. The position vector for the point 0 is

$$\underset{\sim}{R} = \underset{\sim}{c}_B + \underset{\sim}{w}_B + \underset{\sim}{e} \tag{2.19}$$

where the subscript B denotes evaluation at the point B and $\underset{\sim}{e}$ is the vector from point B (ball joint) to the point 0 fixed on the shuttle, measured with respect to the $x_0y_0z_0$ frame. The velocity vector of an arbitrary point C on the cable is then

$$\dot{\underset{\sim}{R}}_C = \dot{\underset{\sim}{w}} \tag{2.20}$$

and the velocity of point 0 is

$$\dot{\underset{\sim}{R}} = \dot{\underset{\sim}{w}}_B + \underset{\sim}{\omega} \times \underset{\sim}{e} \tag{2.21}$$

The kinematics for the shuttle body and appendage remain the same as for the unrestrained spacecraft in space. Hence, the kinetic energy for the entire structure is

$$T = \frac{1}{2}\int_{m_C} |\dot{\underset{\sim}{R}}_C|^2 dm_C + \frac{1}{2}\int_{m_S} |\dot{\underset{\sim}{R}}_S|^2 dm_S + \frac{1}{2}\int_{m_A} |\dot{\underset{\sim}{R}}_A|^2 dm_A$$

$$= \frac{1}{2}\int_{m_C} |\dot{\underset{\sim}{w}}|^2 dm_C + \frac{1}{2}\int_{m_S} |\dot{\underset{\sim}{w}}_B + \underset{\sim}{\omega} \times (\underset{\sim}{e} + \underset{\sim}{r})|^2 dm_S$$

$$+ \frac{1}{2}\int_{m_A} |\dot{\underset{\sim}{w}}_B + \underset{\sim}{\omega} \times (\underset{\sim}{e} + \underset{\sim}{a} + \underset{\sim}{u}) + \dot{\underset{\sim}{u}}|^2 dm_A$$

$$= \frac{1}{2}\int_{m_C} |\dot{\underset{\sim}{w}}|^2 dm_C + \frac{1}{2} m|\dot{\underset{\sim}{w}}_B|^2 + \frac{1}{2}\,\underset{\sim}{\omega}^T I_O \underset{\sim}{\omega} + \frac{1}{2} m(\underset{\sim}{\omega} \times \underset{\sim}{e})\cdot(\underset{\sim}{\omega} \times \underset{\sim}{e})$$

$$+ \dot{\underset{\sim}{w}}_B \cdot (\underset{\sim}{\omega} \times \underset{\sim}{S}_B) + (\underset{\sim}{\omega} \times \underset{\sim}{e})\cdot(\underset{\sim}{\omega} \times \underset{\sim}{S}_O) + \frac{1}{2}\int_{m_A} |\dot{\underset{\sim}{u}}|^2 dm_A$$

$$+ \dot{\underset{\sim}{w}}_B \cdot \int_{m_A} \dot{\underset{\sim}{u}}\, dm_A + \int_{m_A} \dot{\underset{\sim}{u}}\cdot(\underset{\sim}{\omega} \times \underset{\sim}{b}) dm_A + \int_{m_A} (\underset{\sim}{\omega} \times \underset{\sim}{b})\cdot(\underset{\sim}{\omega} \times \underset{\sim}{u})\, dm_A$$

$$+ \frac{1}{2}\int_{m_A} |\underset{\sim}{\omega} \times \underset{\sim}{u}|^2\, dm_A + \int_{m_A} \dot{\underset{\sim}{u}}\cdot(\underset{\sim}{\omega} \times \underset{\sim}{u})\, dm_A \qquad (2.22)$$

where

$$\underset{\sim}{S}_B = \underset{\sim}{S}_O + m\underset{\sim}{e},\ \underset{\sim}{b} = \underset{\sim}{a} + \underset{\sim}{e} \qquad (2.23)$$

The elastic displacement vectors $\underset{\sim}{u}$ and $\underset{\sim}{w}$ have been assumed to be small.

The expression for the virtual work is given by Eq. (2.7), but the potential energy must be modified. The acceleration of gravity will be assumed to be constant and can be expressed as $\underset{\sim}{g} = -g\underset{\sim}{u}_Z$ so that the gravitational potential is

$$V_g = \int_{m_C} (\underset{\sim}{c} + \underset{\sim}{w})\cdot\underset{\sim}{g}\, dm_C + \int_{m_S} (\underset{\sim}{R} + \underset{\sim}{r})\cdot\underset{\sim}{g}\, dm_S + \int_{m_A} (\underset{\sim}{R} + \underset{\sim}{a} + \underset{\sim}{u})\cdot\underset{\sim}{g}\, dm_A \qquad (2.24)$$

where $\underset{\sim}{R}$ is defined by Eq. (2.19) and $\underset{\sim}{u}_Z$ is a unit vector in the Z direction. The elastic potential energy for the system can be expressed as

$$V_E = \frac{1}{2}[\underset{\sim}{u},\underset{\sim}{u}] + \frac{1}{2}[\underset{\sim}{w},\underset{\sim}{w}] \qquad (2.25)$$

where $[\underset{\sim}{w},\underset{\sim}{w}]$ is the energy inner product for the cable.

As with the appendage in the preceding section, the elastic displacement of the cable can be approximated by a linear combination of admissible functions, or

$$\underset{\sim}{w} = \psi \underset{\sim}{\eta} \tag{2.26}$$

where ψ is a matrix of space-dependent admissible functions and $\underset{\sim}{\eta}$ is a vector of time-dependent generalized coordinates. Introducing Eqs. (2.8) and (2.26) into Eq. (2.22), the kinetic energy takes the matrix form

$$\begin{aligned} T = {} & \frac{1}{2}\dot{\underset{\sim}{\eta}}^T M_C \dot{\underset{\sim}{\eta}} + \frac{1}{2}\underset{\sim}{\omega}^T (I_0 + m\tilde{e}^T\tilde{e} + 2\tilde{e}^T\tilde{S}_0)\underset{\sim}{\omega} + \dot{\underset{\sim}{\eta}}^T \psi_B^T C^T \tilde{S}_B \underset{\sim}{\omega} + \frac{1}{2}\dot{\underset{\sim}{q}}^T M_A \dot{\underset{\sim}{q}} \\ & + \dot{\underset{\sim}{\eta}}^T \psi_B^T C^T \bar{\Phi}\dot{\underset{\sim}{q}} + \dot{\underset{\sim}{\eta}}^T \psi_B^T C^T \tilde{\omega}^T \bar{\Phi}\underset{\sim}{q} + \dot{\underset{\sim}{q}}^T \tilde{\Phi}^T \underset{\sim}{\omega} \\ & + \underset{\sim}{\omega}^T \int_{m_A} \tilde{b}\tilde{\omega}\Phi \, dm_A \, \underset{\sim}{q} + \dot{\underset{\sim}{q}}^T \tilde{L}_A(\underset{\sim}{\omega})\underset{\sim}{q} - \frac{1}{2}\underset{\sim}{q}^T \bar{L}_A(\underset{\sim}{\omega})\underset{\sim}{q} \end{aligned} \tag{2.27a}$$

where

$$\tilde{\Phi}^T = \int_{m_A} \Phi^T \tilde{b} \, dm_A \tag{2.27b}$$

has been redefined and

$$M_C = \int_{m_C} \psi^T \psi \, dm_C + m\psi_B^T \psi_B \tag{2.27c}$$

is the combined mass matrix of the cable and of the structure lumped at the end of the cable, in which ψ_B denotes the matrix ψ evaluated at B. Introducing Eqs. (2.8) and (2.26) into Eqs. (2.24) and (2.25) the potential energy can be written in the matrix form

$$V = \underset{\sim}{\eta}^T \bar{\psi}^T \underset{\sim}{g} + S_B^T C \underset{\sim}{g} + m\underset{\sim}{\eta}^T \psi_B^T \underset{\sim}{g} + \underset{\sim}{q}^T \bar{\Phi}^T C \underset{\sim}{g} + \frac{1}{2}\underset{\sim}{q}^T K_A \underset{\sim}{q} + \frac{1}{2}\underset{\sim}{\eta}^T K_C \underset{\sim}{\eta} \tag{2.28}$$

where

$$\bar{\psi} = \int_{m_C} \psi \, dm_C \tag{2.29a}$$

and

$$K_C = [\psi, \psi] \tag{2.29b}$$

is the stiffness matrix of the support. Considering Eqs. (2.19) and (2.25), the virtual work can be expressed as

$$\delta W = \underset{\sim}{F}^T C \psi_B \delta \underset{\sim}{\eta} + \underset{\sim}{M}^T D(\underset{\sim}{\alpha}) \delta \underset{\sim}{\alpha} + \underset{\sim}{Q}^T \delta \underset{\sim}{q} \tag{2.30}$$

where all the terms have been defined previously. The effect of the friction of the ball joint can be assumed in the form of an external torque.

Lagrange's equations remain in the symbolic form of Eqs. (2.17), with the exception of Eq. (2.17a) which must be replaced by

$$\frac{d}{dt}\left(\frac{\partial T}{\partial \dot{\underset{\sim}{\eta}}}\right) + \frac{\partial V}{\partial \underset{\sim}{\eta}} = \psi_B^T C^T \underset{\sim}{F} \tag{2.31}$$

Using the same approach as in Sec. 2.2, the equations of motion for the laboratory experiment can be shown to have the form

$$\begin{aligned} M_C \ddot{\underset{\sim}{\eta}} &+ \psi_B^T C^T \tilde{S}_B \dot{\underset{\sim}{\omega}} + \psi_B^T C^T \tilde{\omega}^T \tilde{S}_B \underset{\sim}{\omega} + \psi_B^T C^T \bar{\Phi} \dot{\underset{\sim}{q}} + 2\psi_B^T C^T \tilde{\omega}^T \bar{\Phi} \dot{\underset{\sim}{q}} \\ &+ \psi_B^T C^T (\tilde{\omega}^2 + \dot{\tilde{\omega}}^T) \bar{\Phi} \underset{\sim}{q} + (m \psi_B^T + \bar{\psi}^T) \underset{\sim}{g} + K_C \underset{\sim}{\eta} = \psi_B^T C^T \underset{\sim}{F} \end{aligned} \tag{2.32a}$$

$$\begin{aligned} I_B \dot{\underset{\sim}{\omega}} &+ \tilde{\omega}^T I_B \underset{\sim}{\omega} + \tilde{S}_B^T C \psi_B \ddot{\underset{\sim}{\eta}} + \tilde{\Phi} \ddot{\underset{\sim}{q}} + [J(\dot{\underset{\sim}{\omega}}) + \tilde{\omega}^T J(\underset{\sim}{\omega}) \\ &+ \widetilde{[C\underset{\sim}{g}]} \bar{\Phi}] \underset{\sim}{q} + [\tilde{\omega}^T \tilde{\Phi} + J(\underset{\sim}{\omega})] \dot{\underset{\sim}{q}} + \widetilde{[C\underset{\sim}{g}]} \underset{\sim}{S}_B = \underset{\sim}{M} \end{aligned} \tag{2.32b}$$

$$M_A \ddot{\underset{\sim}{q}} + \bar{\Phi}^T C \psi_B \ddot{\underset{\sim}{\eta}} + \tilde{\Phi}^T \dot{\underset{\sim}{\omega}} + \int_{m_A} \Phi^T \tilde{\omega}^T \tilde{b} \underset{\sim}{\omega} \, dm_A$$

$$+ \bar{\Phi}^T C\underset{\sim}{g} + \tilde{L}_A(\underset{\sim}{\omega})\dot{\underset{\sim}{q}} + [\bar{L}_A(\underset{\sim}{\omega}) + \tilde{L}_A(\dot{\underset{\sim}{\omega}}) + K_A]\underset{\sim}{q} = \underset{\sim}{Q} \qquad (2.32c)$$

where $J(\underset{\sim}{\omega})$ is redefined by replacing $\underset{\sim}{a}$ with $\underset{\sim}{b}$ in Eq. (2.18d) and

$$I_B = I_0 + m\tilde{e}^T\tilde{e} + \tilde{e}^T\tilde{S}_0 + \tilde{S}_0^T\tilde{e} \qquad (2.32d)$$

is the mass moment of inertia of the spacecraft about point B. In this case, the set of Euler angles $\underset{\sim}{\alpha}$ is assumed to be of arbitrary magnitude, which is responsible for many nonlinear terms in Eqs. (2.32).

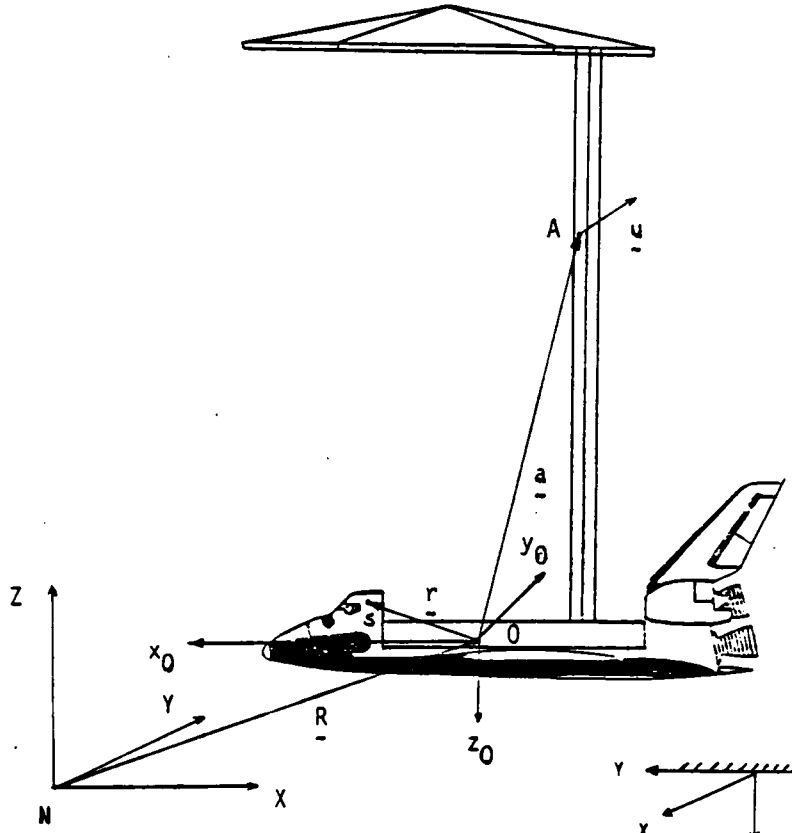

Figure 2.1 Earth orbiting spacecraft.

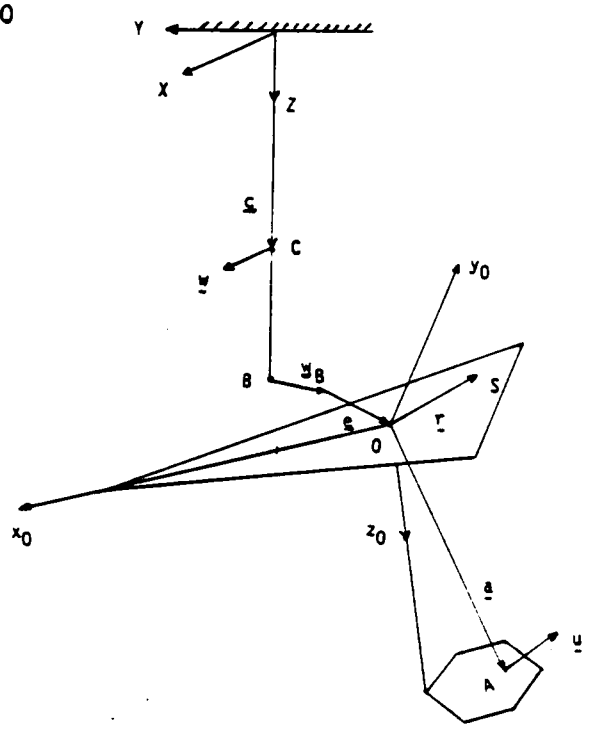

Figure 2.2 SCOLE configuration

CHAPTER III

PERTURBATION OF THE EQUATIONS OF MOTION

3.1 INTRODUCTION

The equations of motion derived in Chapter 2 both for a structure in an earth orbit and for one suspended in the laboratory are nonlinear. The nonlinear terms result from the large rigid-body maneuver. In this chapter a first-order perturbation approach is introduced to solve the equations of motion. This technique transforms the equations of motion into a set of zero-order equations governing the rigid-body motions and a set of first-order time-varying linear equations governing small elastic motions and deviations from the prescribed rigid-body maneuver.

The perturbation technique permits a maneuver strategy that is independent of the elastic analysis and is discussed in Chapter 5. The maneuver history introduces time-varying coefficients into the first-order equations of motion. These coefficients are known as soon as the desired maneuver history has been determined.

3.2 Perturbation Method

The nonlinear equations of motion for the orbiting spacecraft have the same basic form as for the laboratory experiment. Hence, the approach to the solution suggested here applies for both situations.

Consider a first-order perturbation on the quantities $\underset{\sim}{R}$ and $\underset{\sim}{\alpha}$.

$$\underset{\sim}{R} = \underset{\sim}{R}_0 + \underset{\sim}{R}_1 \ , \quad \underset{\sim}{\alpha} = \underset{\sim}{\alpha}_0 + \underset{\sim}{\alpha}_1 \qquad (3.1a,b)$$

where the first order terms $\underset{\sim}{R}_1$ and $\underset{\sim}{\alpha}_1$ are small compared to the zero order terms $\underset{\sim}{R}_0$ and $\underset{\sim}{\alpha}_0$. Introducing Eqs. (3.1) into the nonlinear equations of motion, Eqs. (2.18) or (2.32), and separating orders of magnitudes, we obtain zero-order and first-order perturbation equations. The zero-order equations can be used for the maneuvering of the spacecraft and the first-order equations for vibration suppression and rigid-body corrections. Before proceeding with this technique, we will first develop some expressions relating the perturbations in the Euler angles, $\underset{\sim}{\alpha}$, with small angular deflections, $\underset{\sim}{\beta}$, expressed in the body-fixed frame. This is done so that all the variables in the perturbation equations can be expressed in the body-fixed frame, the frame in which state measurements will be taken and actuating forces will be applied. Note that a set of Euler angles of arbitrary magnitude do not form a vector whereas the angles $\underset{\sim}{\beta}$, being small, can be thought of as a vector quantity.

First consider Eq. (2.16a) which relates the velocities of the Euler angles to the body fixed angular velocities, $\underset{\sim}{\omega}$. Introducing Eq. (3.1b) into Eq. (2.16a) and neglecting higher-order terms, we obtain the perturbed angular velocity vector

$$\underset{\sim}{\omega} \cong \underset{\sim}{\omega}_0 + \underset{\sim}{\omega}_1 \tag{3.2}$$

where

$$\underset{\sim}{\omega}_0 = D(\underset{\sim}{\alpha}_0)\dot{\underset{\sim}{\alpha}}_0 \ , \quad \underset{\sim}{\omega}_1 = D(\underset{\sim}{\alpha}_1)\dot{\underset{\sim}{\alpha}}_0 + D(\underset{\sim}{\alpha}_0)\dot{\underset{\sim}{\alpha}}_1 \tag{3.3a,b}$$

Using similar considerations, it can be shown that the body-fixed perturbation angles can be related to the perturbed Euler angles by the expression

$$\underset{\sim}{\beta} = D(\underset{\sim}{\alpha}_0)\underset{\sim}{\alpha}_1 \tag{3.4}$$

Note that the vector $\underset{\sim}{\beta}$ is a first-order perturbation of a set of quasi-coordinates (Ref. 12). Taking the time derivative of Eq. (3.4) and introducing into Eq. (3.3a), the perturbed angular velocity vector, $\underset{\sim}{\omega}_1$, is related to the angles $\underset{\sim}{\beta}$ by the expression

$$\underset{\sim}{\omega}_1 = \tilde{\omega}_0^T\underset{\sim}{\beta} + \dot{\underset{\sim}{\beta}} \tag{3.5}$$

Taking the time derivative of Eq. (3.5), the perturbed angular acceleration becomes

$$\dot{\underset{\sim}{\omega}}_1 = \dot{\tilde{\omega}}_0^T\underset{\sim}{\beta} + \tilde{\omega}_0^T\dot{\underset{\sim}{\beta}} + \ddot{\underset{\sim}{\beta}} \tag{3.6}$$

Recall that the elements of the transformation matrix C from the body-fixed frame to the inertial frame consist of trigonometric functions of the Euler angles, so that a perturbation of this matrix will also involve the vector $\underset{\sim}{\beta}$. This relation can be derived using Eq. (3.4). Instead, consider the frame O' which differs from the O frame by the angles $\underset{\sim}{\beta}$. Then, the transformation from the O' frame to the O frame is $[I + \tilde{\beta}]$ where I is an identity matrix. Letting C_0 be the transformation matrix from the O frame to the inertial frame, the total transformation matrix, C, from the O' frame to the inertial frame can be expressed as

$$C \cong C_0 + C_1 \tag{3.7}$$

where

$$C_1 = \tilde{\beta} C_0 \tag{3.8}$$

In keeping with our objective of expressing the first-order perturbation equations in the body fixed frame, Eq. (3.1a) is replaced by

$$\underset{\sim}{R} = \underset{\sim}{R}_0 + C_0^T \underset{\sim}{R}_1 \tag{3.9}$$

where $\underset{\sim}{R}_1$ is now a vector measured with respect to the 0 frame. The control forces and moments can also be expressed in first-order perturbed form as follows:

$$\underset{\sim}{F} = \underset{\sim}{F}_0 + \underset{\sim}{F}_1 \ , \quad \underset{\sim}{M} = \underset{\sim}{M}_0 + \underset{\sim}{M}_1 \tag{3.10a,b}$$

Spacecraft

Introducing Eqs. (3.1) through (3.10) into Eqs. (2.18) and neglecting higher-order terms, we obtain two sets of equations of motion for the spacecraft in orbit. The zero-order equations, which govern the motion of the structure as if it were rigid, can be expressed as

$$m\ddot{\underset{\sim}{R}}_0 + C_0^T \tilde{S}_0 \dot{\underset{\sim}{\omega}}_0 + C_0^T \tilde{\omega}_0^T \tilde{S}_0 \underset{\sim}{\omega}_0 + \frac{Gm_e'}{|\underset{\sim}{R}_0|^3} [m\underset{\sim}{R}_0 + (I - 3\hat{\underset{\sim}{R}}_0 \hat{\underset{\sim}{R}}_0^T) C_0^T \underset{\sim}{S}_0] = C_0^T \underset{\sim}{F}_0 \tag{3.11a}$$

$$\tilde{S}_0^T C_0 \ddot{\underset{\sim}{R}}_0 + \frac{Gm_e}{|\underset{\sim}{R}_0|^3} \tilde{S}_0^T C_0 \underset{\sim}{R}_0 + I_0 \dot{\underset{\sim}{\omega}}_0 + \tilde{\omega}_0^T I_0 \underset{\sim}{\omega}_0 = \underset{\sim}{M}_0 \tag{3.11b}$$

where $\hat{\underset{\sim}{R}}_0$ is a unit vector in the direction of $\underset{\sim}{R}_0$. The first-order equations, which govern the small scale motions of the structure, can be expressed as

$$m\ddot{\underset{\sim}{R}}_1 + 2m\tilde{\omega}_0^T \dot{\underset{\sim}{R}}_1 + [\dot{\tilde{\omega}}_0^T + \tilde{\omega}_0^2 + \bar{H}] \underset{\sim}{R}_1 + \tilde{S}_0 \ddot{\underset{\sim}{\beta}} + 2\tilde{\omega}_0^T \tilde{S}_0 \dot{\underset{\sim}{\beta}} + [\dot{\tilde{\omega}}_0^T + \tilde{\omega}_0^2 + \bar{H}] \tilde{S}_0 \underset{\sim}{\beta}$$

$$+ \tilde{F}_0^T \underset{\sim}{\beta} + \bar{\Phi} \ddot{\underset{\sim}{q}} + 2\tilde{\omega}_0^T \bar{\Phi} \dot{\underset{\sim}{q}} + [\dot{\tilde{\omega}}_0^T + \tilde{\omega}_0^2 + \bar{H}] \bar{\Phi} \underset{\sim}{q} = \underset{\sim}{F}_1 \tag{3.12a}$$

$$\tilde{S}_0^T \ddot{R}_1 + 2\tilde{S}_0^T \tilde{\omega}_0^T \dot{R}_1 + \tilde{S}_0^T [\dot{\tilde{\omega}}_0^T + \tilde{\omega}_0^2 + \bar{H}] R_1 + \tilde{F}_0 R_1$$
$$+ I_0 \ddot{\beta} + [I\tilde{\omega}_0^T + \tilde{\omega}_0^T I_0 + [\widetilde{I_0 \omega_0}]] \dot{\beta}$$
$$+ [I_0 \dot{\tilde{\omega}}_0^T + \tilde{\omega}_0^T I_0 \tilde{\omega}_0^T + [\widetilde{I_0 \omega_0}] \tilde{\omega}_0^T + \tilde{S}_0 \tilde{H}] \beta + \tilde{\Phi} \ddot{q}$$
$$+ [\tilde{\omega}_0^T \tilde{\Phi} + J_0] \dot{q} + [\dot{J}_0 + \tilde{\omega}_0^T J_0 + \tilde{H\Phi}] q = M_1 \qquad (3.12b)$$

$$\bar{\Phi}^T \ddot{R}_1 + 2\bar{\Phi}^T \tilde{\omega}_0^T \dot{R}_1 + \bar{\Phi}^T [\dot{\tilde{\omega}}_0^T + \tilde{\omega}_0^2 + \bar{H}] R_1 + \tilde{\Phi}^T \ddot{\beta}$$
$$+ [\tilde{\Phi}^T \tilde{\omega}_0^T - J_0^T] \dot{\beta} + [\tilde{\Phi}^T \dot{\tilde{\omega}}_0^T - J_0^T \tilde{\omega}_0^T + \bar{\Phi}^T \tilde{H}] \beta$$
$$+ M_A \ddot{q} + \tilde{L}_A \dot{q} + [\bar{L}_A + \dot{\tilde{L}}_A + K_A] q = Q_0 + Q_1 \qquad (3.12c)$$

where

$$\bar{H} = \frac{Gm_e}{|R_0|^3} [I - 3C_0 \hat{R}_0 \hat{R}_0^T C_0^T] \qquad (3.12d)$$

$$\tilde{H} = [\widetilde{C_0 \ddot{R}_0}] + \frac{Gm_e}{|R_0|^3} [\widetilde{C_0 R_0}] \qquad (3.12e)$$

$$Q_0 = -[\bar{\Phi}^T C_0 \ddot{R}_0 + \frac{Gm_e}{|R_0|^3} \bar{\Phi}^T C_0 R_0 + \tilde{\Phi}^T \dot{\omega}_0 + \int_{m_A} \Phi^T \tilde{\omega}_0^T \tilde{a} \omega_0 \, dm_A] \qquad (3.12f)$$

Laboratory Experiment

For the laboratory experiment to be successful, the deflections of the cable (translation of the spacecraft) should be small. From purely rigid-body dynamic considerations, the point B (ball joint) must be close to the center of mass in the plane normal to the axis of rotation during a maneuver. Hence, the vector S_B can be considered to be small in the following analysis. Because the motion of the cable has been

assumed to be small, introducing Eq. (3.3) into Eq. (2.32b), the zero-order equations for the laboratory experiment are simply

$$I_B\dot{\tilde{\omega}}_0 + \tilde{\omega}_0^T I_B\tilde{\omega}_0 = M_0 \tag{3.13}$$

The motion of the cable, $\psi\eta$, can be expressed with respect to the body-fixed frame, as was done with the vector R_1 for the orbiting spacecraft. Introducing Eqs. (3.3), (3.6), (3.7), (3.8) and (3.10) into Eqs. (2.32) and neglecting higher-order terms, the first-order equations of motion for the laboratory experiment can be expressed as follows:

$$M_C\ddot{\eta} + 2\tilde{L}_C\dot{\eta} + [\dot{\tilde{L}}_C + \bar{L}_C + K_C]\eta + \psi_B^T\tilde{S}_B\ddot{\beta} + 2\psi_B^T\tilde{\omega}_0^T\tilde{S}_B\dot{\beta} + \psi_B^T[\dot{\tilde{\omega}}_0^T + \tilde{\omega}_0^2]\tilde{S}_B\beta$$
$$+ \psi_B^T\bar{\Phi}\ddot{q} + 2\psi_B^T\tilde{\omega}_0^T\bar{\Phi}\dot{q} + \psi_B^T[\dot{\tilde{\omega}}_0^T + \tilde{\omega}_0^2]\bar{\Phi}q = F_0 + \psi_B^T F \tag{3.14a}$$

$$\tilde{S}_B^T\psi_B\ddot{\eta} + 2\tilde{S}_B^T\tilde{\omega}_0^T\psi_B\dot{\eta} + \tilde{S}_B^T[\dot{\tilde{\omega}}_0^T + \tilde{\omega}_0^2]\psi_B\eta$$
$$+ I_B\ddot{\beta} + [I_B\tilde{\omega}_0^T + \tilde{\omega}_0^T I_B + \widetilde{[I_B\omega_0]}]\dot{\beta}$$
$$+ [I_B\dot{\tilde{\omega}}_0^T + \tilde{\omega}_0^T I_B\tilde{\omega}_0^T + \widetilde{[I_B\omega_0]}\tilde{\omega}_0^T + \tilde{S}_B\widetilde{[C_0 g]}]\beta$$
$$+ \tilde{\Phi}\ddot{q} + [\tilde{\omega}_0^T\tilde{\Phi} + J_0]\dot{q} + [\dot{J}_0 + \tilde{\omega}_0^T J_0 + \widetilde{[C_0 g]}\bar{\Phi}]q$$
$$= M_0' + M_1 \tag{3.14b}$$

$$\bar{\Phi}^T\psi_B\ddot{\eta} + 2\bar{\Phi}^T\tilde{\omega}_0^T\psi_B\dot{\eta} + \bar{\Phi}^T(\dot{\tilde{\omega}}_0^T + \tilde{\omega}_0^2)\psi_B\eta$$
$$+ \tilde{\Phi}^T\ddot{\beta} + [\tilde{\Phi}^T\tilde{\omega}_0^T - J_0^T]\dot{\beta} + [\tilde{\Phi}^T\dot{\tilde{\omega}}_0^T - J_0^T\tilde{\omega}_0^T + \bar{\Phi}^T\widetilde{[C_0 g]}^T]\beta$$
$$+ M_A\ddot{q} + \tilde{L}_A\dot{q} + [\bar{L}_A + \dot{\tilde{L}}_A + K_A]q = Q_0 + Q_1 \tag{3.14c}$$

where

$$\underset{\sim}{F}_0 = -\psi_B^T[\tilde{\underset{\sim}{\omega}}_0^T\tilde{S}_B\underset{\sim}{\omega}_0 + \tilde{S}_B\dot{\underset{\sim}{\omega}}_0] - (m\psi_B^T + \bar{\psi}^T)C_0\underset{\sim}{g} \tag{3.14d}$$

$$M_0' = \tilde{S}_B C_0 \underset{\sim}{g} \tag{3.14e}$$

$$\underset{\sim}{Q}_0 = -[\tilde{\Phi}^T\dot{\underset{\sim}{\omega}}_0 + \int_{m_A} \Phi^T\tilde{\underset{\sim}{\omega}}_0^T\tilde{b}\underset{\sim}{\omega}_0\, dm_A + \bar{\Phi}^T C_0\underset{\sim}{g}] \tag{3.14f}$$

3.3 First-Order Equations In Matrix Form

For the orbiting spacecraft, Eqs. (3.11) can be solved for $\underset{\sim}{F}_0(t)$ and $\underset{\sim}{M}_0(t)$ for any desired maneuver strategy $\underset{\sim}{R}_0(t)$ and $\underset{\sim}{\omega}_0(t)$. For the laboratory experiment, Eqs. (3.13) can be solved for $\underset{\sim}{M}_0(t)$ for any desired $\underset{\sim}{\omega}_0(t)$. In either case, these quantities can then be substituted into the first-order equations (Eqs. (3.12) or (3.14)) producing a set of linear equations with known time-varying coefficients which govern the small deviations from the rigid-body maneuver and elastic motions of the structure. These linear equations can be expressed in the matrix form

$$\underset{\sim}{M}\ddot{\underset{\sim}{x}} + \underset{\sim}{G}\dot{\underset{\sim}{x}} + (K_S + K_{NS})\underset{\sim}{x} = \underset{\sim}{F}^* \tag{3.15}$$

where for the orbiting case

$$\underset{\sim}{x}^T = [\underset{\sim}{R}_1^T \quad \underset{\sim}{\beta}^T \quad \underset{\sim}{q}^T] \tag{3.16a}$$

$$\underset{\sim}{F}^{*T} = [\underset{\sim}{F}_1^T \quad \underset{\sim}{M}_1^T \quad \underset{\sim}{Q}_0^T + \underset{\sim}{Q}_1^T] \tag{3.16b}$$

$$M = \begin{bmatrix} M_0 & \tilde{S}_0 & \bar{\Phi} \\ \tilde{S}_0^T & I_0 & \tilde{\Phi} \\ \bar{\Phi}^T & \tilde{\Phi}^T & M_A \end{bmatrix} \qquad M_0 = \begin{bmatrix} m & 0 & 0 \\ 0 & m & 0 \\ 0 & 0 & m \end{bmatrix} \tag{3.16c,d}$$

$$G = \begin{bmatrix} 2M_0\tilde{\omega}_0^T & 2\tilde{\omega}_0^T\tilde{S}_0 & 2\tilde{\omega}_0^T\bar{\Phi} \\ -2(\tilde{\omega}_0^T\tilde{S}_0)^T & I_0\tilde{\omega}_0^T + \tilde{\omega}_0^T I_0 + [\widetilde{I_{0\underset{\sim}{\omega}0}}] & \tilde{\omega}_0^T\tilde{\Phi} + J_0 \\ -2(\tilde{\omega}_0^T\bar{\Phi})^T & -[\tilde{\omega}_0^T\tilde{\Phi} + J_0]^T & 2\tilde{L}_A \end{bmatrix} \tag{3.16e}$$

$$K_s = \begin{bmatrix} M_0[\tilde{\omega}_0^2 + \bar{H}] & \tilde{F}_0^T + [\tilde{\omega}_0^2 + \bar{H}]\tilde{S}_0 & [\tilde{\omega}_0^2 + \bar{H}]\bar{\Phi} \\ \tilde{F}_0 + \tilde{S}_0^T[\tilde{\omega}_0^2 + \bar{H}] & \tilde{\omega}_0 I_0\tilde{\omega}_0 & \tilde{\omega}_0^T J_0 + \tilde{H}\bar{\Phi} \\ \bar{\Phi}^T[\tilde{\omega}_0^2 + \bar{H}] & J_0^T\tilde{\omega}_0 + \bar{\Phi}^T\tilde{H}^T & \bar{L}_A + K_A \end{bmatrix} \tag{3.16f}$$

$$K_{NS} = \begin{bmatrix} M_0\dot{\tilde{\omega}}_0^T & \dot{\tilde{\omega}}_0^T\tilde{S}_0 & \dot{\tilde{\omega}}_0^T\bar{\Phi} \\ -(\dot{\tilde{\omega}}_0^T\tilde{S}_0)^T & I_0\dot{\tilde{\omega}}_0^T + [\widetilde{I_{0\underset{\sim}{\omega}0}}]\tilde{\omega}_0^T + \tilde{S}_0\tilde{H} & \dot{J}_0 \\ -(\dot{\tilde{\omega}}_0^T\bar{\Phi})^T & \tilde{\Phi}^T\dot{\tilde{\omega}}_0^T & \dot{\tilde{L}}_A \end{bmatrix} \tag{3.16g}$$

and for the laboratory experiment

$$\underset{\sim}{x}^T = [\underset{\sim}{\eta}^T \quad \underset{\sim}{\beta}^T \quad \underset{\sim}{q}^T] \tag{3.17a}$$

$$\underset{\sim}{F}^{*T} = [\underset{\sim}{F}_0^T + \psi_B\underset{\sim}{F}_1^T \quad \underset{\sim}{M}_0'^T + \underset{\sim}{M}_1^T \quad \underset{\sim}{Q}_0^T + \underset{\sim}{Q}_1^T] \tag{3.17b}$$

$$M = \begin{bmatrix} M_C & \psi_B^T\tilde{S}_B & \psi_B^T\bar{\Phi} \\ \tilde{S}_B^T\psi_B & I_B & \tilde{\Phi} \\ \bar{\Phi}^T\psi_B & \tilde{\Phi}^T & M_A \end{bmatrix} \tag{3.17c}$$

$$G = \begin{bmatrix} 2\tilde{L}_C & 2\psi_B^T\tilde{\omega}_0^T\tilde{S}_B & 2\psi_B^T\tilde{\omega}_0^T\bar{\Phi} \\ -2(\psi_B^T\tilde{\omega}_0^T\tilde{S}_B)^T & I_B\tilde{\omega}_0^T + \tilde{\omega}_0^T I_B + [\widetilde{I_{B\underset{\sim}{\omega}0}}] & \tilde{\omega}_0^T\tilde{\Phi} + J_0 \\ -2(\psi_B^T\tilde{\omega}_0^T\bar{\Phi}) & -[\tilde{\omega}_0^T\tilde{\Phi} + J_0]^T & 2\tilde{L}_A \end{bmatrix} \tag{3.17d}$$

$$K_S = \begin{bmatrix} \bar{L}_C + K_C & \psi_B^T \tilde{\omega}_0^2 \tilde{S}_B & \psi_B^T \tilde{\omega}_0^2 \bar{\Phi} \\ \tilde{S}_B^T \tilde{\omega}_0^2 \psi_B & \tilde{\omega}_0 I_B \tilde{\omega}_0 & \tilde{\omega}_0^T J_0 + [\widetilde{C_0 g}] \bar{\Phi} \\ \bar{\Phi}^T \tilde{\omega}_0^2 \psi_B & J_0^T \tilde{\omega}_0 + \bar{\Phi}^T [\widetilde{C_0 g}]^T & \bar{L}_A + K_A \end{bmatrix} \tag{3.17e}$$

$$K_{NS} = \begin{bmatrix} \dot{\tilde{L}}_C & \psi_B^T \dot{\tilde{\omega}}_0^T \tilde{S}_B & \psi_B^T \dot{\tilde{\omega}}_0^T \bar{\Phi} \\ -(\psi_B^T \dot{\tilde{\omega}}_0^T \tilde{S}_B)^T & I_B \dot{\tilde{\omega}}_0^T + [\widetilde{I_B \omega_0}] \tilde{\omega}_0^T + \tilde{S}_B [\widetilde{C_0 g}] & \dot{J}_0 \\ -(\psi_B^T \dot{\tilde{\omega}}_0^T \bar{\Phi})^T & \bar{\Phi}^T \dot{\tilde{\omega}}_0^T & \tilde{L}_A \end{bmatrix} \tag{3.17f}$$

In both cases, the mass matrix is symmetric. For the orbiting structure, the mass matrix is time invariant, whereas for the laboratory configuration, it is not. This is the case because the mass matrix of the cable, M_C, is calculated with respect to the body-fixed frame, and hence it is a function of the transformation matrix $C_0(t)$. The matrix M_C, and hence M, can be considered as being time-invariant if the axis of rotation corresponds to the axis of the cable. Furthermore, because the mass of the cable is much smaller than the mass of the spacecraft (<0.8%), it can be regarded as negligible for some purposes. Under these circumstances, M becomes time-invariant for all maneuvers, as it is in the case of the orbiting spacecraft.

In both cases, the time varying matrix G, multiplying the velocity vector, is skew-symmetric. This matrix contains the Coriolis (gyroscopic) terms.

The stiffness matrix has been split into two parts, one part, K_S, with purely symmetric terms, the other, K_{NS}, with the terms which lead to nonsymmetries. Of course, K_{NS} can be separated into symmetric and skew-symmetric matrices if desired. As can be seen in Eqs. (3.16g) and

(3.17f), the terms containing the angular acceleration, $\dot{\underset{\sim}{\omega}}_0$, of the body-fixed frame lead to nonsymmetric terms in the stiffness matrix. In fact, many of these terms are skew-symmetric, and hence, circulatory. Note that the perturbation of the Euler equations resulted in some nonsymmetric terms containing only the angular velocity vector $\underset{\sim}{\omega}_0$. This is not surprising, because it is well known that a steady-state rigid-body rotation about the axis of intermediate inertia is unstable. Owing to the nonsymmetry of the stiffness matrices, the vibration problem is nonself-adjoint in both cases.

Because structural damping was ignored, the matrix G is due entirely to gyroscopic effects, and hence conservative in nature. On the other hand, the stiffness matrix contains circulatory, nonconservative terms. During the maneuver, the centrifugal, tangential and gravitational forces cause a change in the initial elastic deflection of the structure, which in turn affect the spacecraft's orientation. Therefore, the first-order vibration problem appears to be "self-excited" or, in a mathematical sense, non-self-adjoint. Hence, physical insight agrees with the mathematical results. Active control is then necessary to stabilize the zero-order maneuver, as well as to suppress the first-order vibrations. If the final orientation does not correspond to a stable equilibrium state, active control is also needed after the maneuver to maintain this final state. Thus, it is convenient if the maneuver begins and ends at a stable equilibrium state, especially for the laboratory experiment where gravity is much more significant.

CHAPTER IV

DISCRETE SUBSTRUCTURE SYNTHESIS: SPATIAL DISCRETIZATION

4.1 INTRODUCTION

In Chapter 2, we introduced admissible functions capable of spatially discretizing flexible appendages. In this chapter, a type of discrete substructure synthesis involving a particular method of satisfying substructure connectivity is discussed. Because discrete substructure synthesis does not involve large rigid-body motions, this chapter is confined to linear, constant coefficient, vibration problems.

One of the most versatile discretization procedures is the finite element method (FEM). Unfortunately, finite element models require in general a large number of degrees of freedom, so that an alternative is often desirable. In discrete substructure synthesis (DSS), a structure is regarded as an assemblage of substructures. As an example, the appendage attached to the shuttle in SCOLE can be regarded as consisting of two substructures, one being the mast and the other the antenna. Each substructure is discretized using the FEM and the number of degrees of freedom used to represent the substructure is reduced using admissible vectors defined over the domain of the substructure (Ref. 15). The mathematical models of the substructures are then assembled to form a model of the entire appendage. Previous methods of assembly have been somewhat inefficient in terms of necessary computer time. A new and much more efficient method of assembling the substructures is introduced which uses a least-squares technique. However, it is the

admissible vectors that are applied in a least-square sense, whereas the substructures are assembled completely and exactly.

The space structures considered until now consist of a rigid-body with a single flexible appendage attached. In this chapter, it is shown that the previous analysis can be readily generalized to allow for multiple appendages. Many existing spacecraft, as well as many planned for the future, can be modeled in this manner.

The equations of motion of Chapter 2 were derived on the basis of elastic members representing general distributed-parameter structures. The flexible appendage attached to the shuttle for SCOLE can be modeled as a collection of one dimensional beam elements. As such, in this chapter the equations of motion are modified to include such a case.

4.2 LINEARIZED EQUATIONS OF MOTION: MULTIPLE APPENDAGES

In this section, Lagrange's equations of motion are developed for a spacecraft consisting of a main rigidy-body with n appendages as in Fig. 4.1. The equations are linearized about a given equilibrium position and modified by considering structures containing one-dimensional beam elements. The object is to demonstrate that the nonlinear equations developed in Chapter 2 can be readily modified to include multiple appendages and beam elements. The procedure is very similar to that of Chapter 2, so that many details are excluded.

A few notational changes from Chapter 2 are needed to facilitate an efficient derivation of Lagrange's equations of motion. These changes are only for this chapter. Denoting by $\underset{\sim}{r}_{Ei}$ the radius vector from O to the root E_i of the appendage i, by $\underset{\sim}{\rho}_i$ the vector from E_i to a

nominal point in the appendage i and by $\underset{\sim}{u}_i$ the elastic displacement vector of the point, the position of the point in its displaced configuration is $\underset{\sim}{R} + \underset{\sim}{r}_{Ei} + \underset{\sim}{\rho}_i + \underset{\sim}{u}_i$. Note that, comparing with the kinematics of Chapter 2, the vector $\underset{\sim}{a}$ has been replaced by the notation $\underset{\sim}{r}_{Ei} + \underset{\sim}{\rho}_i$. The velocity of a point in the main rigid-body is

$$\underset{\sim}{v}_0 = \dot{\underset{\sim}{R}} + \dot{\underset{\sim}{r}} = \dot{\underset{\sim}{R}} + \underset{\sim}{\omega} \times \underset{\sim}{r} \tag{4.1}$$

where the notation is identical to that of Chapter 2. The velocity of a point in appendage i is

$$\underset{\sim}{v}_i = \dot{\underset{\sim}{R}} + \underset{\sim}{\omega} \times (\underset{\sim}{r}_{Ei} + \underset{\sim}{\rho}_i + \underset{\sim}{u}_i) + \dot{\underset{\sim}{u}}_i \cong \dot{\underset{\sim}{R}} + \underset{\sim}{\omega} \times (\underset{\sim}{r}_{Ei} + \underset{\sim}{\rho}_i) + \dot{\underset{\sim}{u}}_i \tag{4.2}$$

Note that in this linear analysis the term $\underset{\sim}{\omega} \times \underset{\sim}{u}_i$ has been ignored on the basis that it is of second order in magnitude. Hence, the kinetic energy of the spacecraft is

$$T = \frac{1}{2} \sum_{i=0}^{n} \int_{m_i} \underset{\sim}{v}_i \cdot \underset{\sim}{v}_i \, dm_i \tag{4.3}$$

In this chapter, the potential energy is assumed to be due entirely to elastic effects and is written in the symbolic form

$$V = \frac{1}{2} \sum_{i=1}^{n} [\underset{\sim}{u}_i, \underset{\sim}{u}_i] \tag{4.4}$$

Denoting the force vector per unit volume by $\underset{\sim}{f}_i$ $(i = 0,1,\ldots,n)$, we can write the virtual work

$$\delta W = \sum_{i=0}^{n} \int_{D_i} \underset{\sim}{f}_i \cdot \delta(\underset{\sim}{R}_0 + \underset{\sim}{r}_i) dD_i \tag{4.5}$$

where $\underset{\sim}{r}_0 = \underset{\sim}{r}$, $\underset{\sim}{r}_i = \underset{\sim}{r}_{Ei} + \underset{\sim}{\rho}_i + \underset{\sim}{u}_i$ $(i = 1,2,\ldots,n)$. Moreover, D_i is the domain of the body i and D_0 corresponds to the rigid-body.

The expressions above have been derived on the basis of a general distributed-parameter structure. For structures consisting of one-dimensional elements, it is convenient to consider differential elements with finite (rather than infinitesimal) mass moments of inertia. To account for this, the vectors $\underset{\sim}{\rho}_i$ and $\underset{\sim}{u}_i$ now denote the position and displacement, respectively, of the mass center of a beam's rigid cross section, as shown in Fig. 4.2. These changes of notation necessitate the addition of the rotational kinetic energy due to elastic effects to Eq. (4.3). This additional kinetic energy can be expressed as

$$T_\theta = \frac{1}{2} \sum_{i=1}^{n} \int_{m_i} (\underset{\sim}{\Omega}_i \times \underset{\sim}{b}_i) \cdot (\underset{\sim}{\Omega}_i \times \underset{\sim}{b}_i) dm_i \tag{4.6a}$$

where

$$\underset{\sim}{\Omega}_i = \underset{\sim}{\omega} + \dot{\underset{\sim}{\theta}}_i \tag{4.6b}$$

is the total angular velocity vector of a cross section, in which $\dot{\underset{\sim}{\theta}}_i$ is the angular velocity of the cross section due to elastic deformation, and $\underset{\sim}{b}_i$ is a position vector from the mass center to an arbitrary point on the cross section.

The elastic displacements can be expressed in the form of linear combinations of admissible functions, or

$$\begin{bmatrix} \underset{\sim}{u}_i \\ \underset{\sim}{\theta}_i \end{bmatrix} = \Phi_i \underset{\sim}{q}_i = \begin{bmatrix} \Phi_{ui} \\ \Phi_{\theta i} \end{bmatrix} \underset{\sim}{q}_i \qquad i = 1,2,\ldots,n \tag{4.7}$$

where Φ_{ui} and $\Phi_{\theta i}$ are matrices of space-dependent admissible functions corresponding to displacements and rotations, respectively, and $\underset{\sim}{q}_i$ are vectors of time-dependent generalized coordinates, as in Chapter 2.

Introducing Eq. (4.7) into the expressions for the kinetic energy, Eqs. (4.6) and (4.3), the potential energy, Eq. (4.4) and the virtual work, Eq. (4.5), the linearized Lagrange's equations of motion can be written in the symbolic form

$$\frac{d}{dt}\left(\frac{\partial \dot{T}}{\partial \underset{\sim}{\dot{R}}}\right) = \underset{\sim}{F}_0$$

$$\frac{d}{dt}\left(\frac{\partial T}{\partial \underset{\sim}{\omega}}\right) = \underset{\sim}{M}_0 \tag{4.8}$$

$$\frac{d}{dt}\left(\frac{\partial T}{\partial \underset{\sim}{\dot{q}}_i}\right) + \frac{\partial V}{\partial \underset{\sim}{q}_i} = \underset{\sim}{Q}_i \quad , \quad i = 1,2,\ldots,n$$

where

$$\underset{\sim}{F}_0 = \sum_{i=1}^{n} \int_{D_i} \underset{\sim}{f}_{ui} dD_i \tag{4.9a}$$

$$\underset{\sim}{M}_0 = \int_{D_0} \tilde{r}_0^T \underset{\sim}{f}_0 dD_0 + \sum_{i=1}^{n} \int_{D_i} (\tilde{r}_{Ei}^T + \tilde{o}_i^T) \underset{\sim}{f}_{ui} dD_i + \sum_{i=0}^{n} \int_{D_i} \underset{\sim}{f}_{\theta i} dD_i \tag{4.9b}$$

$$\underset{\sim}{Q}_i = \int_{D_i} \Phi_i^T \underset{\sim}{f}_i dD_i \tag{4.9c}$$

are generalized force vectors and

$$\underset{\sim}{f}_i = \begin{bmatrix} \underset{\sim}{f}_{ui} \\ \underset{\sim}{f}_{\theta i} \end{bmatrix} \tag{4.9d}$$

are distributed forces and moments per unit volume. Carrying out the differentiations indicated in Eqs. (4.8), the equations of motion for the flexible spacecraft with n appendages and beam elements take the form

$$m\ddot{\underset{\sim}{R}} + \tilde{\underset{\sim}{S}}\dot{\underset{\sim}{\omega}} + \sum_{i=1}^{n} \bar{\Phi}_{ui}\ddot{\underset{\sim}{q}}_i = \underset{\sim}{F}_0$$

$$\tilde{\underset{\sim}{S}}^T\ddot{\underset{\sim}{R}} + I_0\dot{\underset{\sim}{\omega}} + \sum_{i=1}^{n} (\bar{\Phi}_{\theta i} + \tilde{\Phi}_{ui})\ddot{\underset{\sim}{q}}_i = \underset{\sim}{M}_0 \qquad (4.10)$$

$$\bar{\Phi}_{ui}^T\ddot{\underset{\sim}{R}} + (\bar{\Phi}_{\theta i}^T + \tilde{\Phi}_{ui}^T)\dot{\underset{\sim}{\omega}} + M_i\ddot{\underset{\sim}{q}}_i + K_i\underset{\sim}{q}_i = \underset{\sim}{Q}_i \quad , \quad i = 1,2,\ldots,n$$

where

$$M_i = \int_{m_i} \Phi_i^T\Phi_i \, dm_i \qquad (4.11a)$$

$$K_i = [\Phi_i, \Phi_i] \quad , \quad i = 1,2,\ldots,n \qquad (4.11b)$$

are the mass and stiffness matrices of a typical appendage i and

$$\underset{\sim}{S} = \int_{m_0} \underset{\sim}{r}_0 \, dm_0 + \sum_{i=1}^{n} \int_{m_i} (\underset{\sim}{r}_{Ei} + \underset{\sim}{\rho}_i)dm_i \qquad (4.11c)$$

$$\bar{\Phi}_{ui} = \int_{m_i} \Phi_{ui} dm_i \qquad (4.11d)$$

$$\bar{\Phi}_{\theta i} = \int_{m_i} \Phi_{\theta i} \, dm_i \qquad (4.11e)$$

$$\tilde{\Phi}_{ui}^T = \int_{m_i} \Phi_{ui}^T \, [\tilde{r}_{Ei} + \tilde{\rho}_i]dm_i \qquad (4.11f)$$

It is instructive to compare the linear terms of Eqs. (2.32) with Eq. (4.10). The addition of n appendages merely results in n equations of the form of Eq. (2.32c), each of which describing the elastic deflection of a particular appendage relative to the body-fixed frame. The inclusion of a beam element analysis results in the addition of a matrix of admissible functions corresponding to beam rotations, $\Phi_{\theta i}$.

The matrices $\bar{\Phi}$ and $\tilde{\Phi}$ in Eqs. (2.32) correspond to $\bar{\Phi}_u$ and the matrix sum $\bar{\Phi}_\theta + \tilde{\Phi}_u$ in Eqs. (4.10), respectively. Hence, Eqs. (2.32) can be readily generalized to the case of multiple appendages containing beam elements.

4.3 ADMISSIBLE FUNCTIONS: A LEAST-SQUARES APPROACH TO DISCRETE SUBSTRUCTURE SYNTHESIS (DSS)

The admissible functions used here are combinations of typical finite element interpolation functions and admissible vectors, where the latter are discretized admissible functions. Admissible functions need satisfy only the geometric boundary conditions. For this structure the only geometric boundary conditions result from the fact that the arms are clamped at the hub. The use of admissible vectors results in little additional cost, yet the benefits can be great, i.e., a reduction of system order.

The derivation of Lagrange's equations of motion require matrix quantities for beam elements. As element interpolation functions, Hermite cubics are used for bending and linear functions are used for torsional and axial motions.

Considering a single element, ignoring rotatory inertia (see Fig. 4.3), where j and j-1 are nodal locations, and denoting the nodal displacement vector by $\underset{\sim}{V}$, we can write

$$\underset{\sim}{u}(x,y,z) = \begin{bmatrix} u_x \\ u_y \\ u_z \\ \theta_x \end{bmatrix} = L^T \begin{bmatrix} \underset{\sim}{a}_{j-1} \\ \underset{\sim}{a}_j \end{bmatrix} = L^T \underset{\sim}{V} \tag{4.12}$$

where

$$\underset{\sim}{a}_j = \left[u_{zj} \; \theta_{yj} \; \theta_{xj} \; u_{yj} \; \theta_{zj} \; u_{xj} \right]^T \tag{4.13}$$

and

$$L^T = \begin{bmatrix} L_u^T \\ L_\theta^T \end{bmatrix} = \begin{bmatrix} 0 & 0 & 0 & 0 & 0 & \ell_5 & 0 & 0 & 0 & 0 & 0 & \ell_6 \\ 0 & 0 & 0 & \ell_1 & h\ell_2 & 0 & 0 & 0 & 0 & \ell_3 & h\ell_4 & 0 \\ \ell_1 & -h\ell_2 & 0 & 0 & 0 & 0 & \ell_3 & -h\ell_4 & 0 & 0 & 0 & 0 \\ 0 & 0 & \ell_5 & 0 & 0 & 0 & 0 & 0 & \ell_6 & 0 & 0 & 0 \end{bmatrix}.$$

(4.14)

in which

$$\ell_1 = 3\zeta^2 - 2\zeta^4 \quad , \quad \ell_2 = \zeta^2 - \zeta^3$$
$$\ell_3 = 1 - 3\zeta^2 + 2\zeta^3 \quad , \quad \ell_4 = -\zeta + 2\zeta^2 - \zeta^3 \qquad (4.15)$$
$$\ell_5 = \zeta \quad , \quad \ell_6 = 1 - \zeta$$

Assembling a substructure consisting of n elements, we can write

$$\begin{bmatrix} \underset{\sim}{u} \\ \underset{\sim}{\theta} \end{bmatrix}_S = R_S L_S^T C \underset{\sim}{V}_S \qquad (4.16)$$

where

$$R_S = [R_1 \quad R_2 \quad \cdots \quad R_n] \qquad (4.17a)$$

and

$$L_S = \begin{bmatrix} L_1 & & & \\ & L_2 & & \\ & & \ddots & \\ & & & L_n \end{bmatrix} \qquad (4.17b)$$

in which R_j is the transformation matrix from the coordinate system $x_0y_0z_0$ to the local coordinate system $x_{Ej}y_{Ej}z_{Ej}$ of the element j and L_j is the interpolation matrix for element j, as shown by Eq. (4.14).

Moreover, the vector $\underset{\sim}{V}_s$ denotes substructure nodal displacements and rotations in substructure coordinates and C is the substructure connectivity matrix defined by the expression

$$\underset{\sim}{V}_d = C\underset{\sim}{V}_s \tag{4.17c}$$

where

$$\underset{\sim}{V}_d = [\underset{\sim}{V}_1^T \quad \underset{\sim}{V}_2^T \quad \cdots \quad \underset{\sim}{V}_n^T]^T \tag{4.17d}$$

is the vector of the disjoint elements nodal displacements and rotations. Note that the purpose of the connectivity matrix is to cause the elements to act together as a substructure.

Next, we assemble N substructures to form the motion vector for an arm as follows:

$$\begin{bmatrix} \underset{\sim}{u} \\ \underset{\sim}{\theta} \end{bmatrix}_a = R_a L_a^T C_a T \underset{\sim}{V}_a \tag{4.18a}$$

where

$$R_a = [R_{s1} \quad R_{s2} \quad \cdots \quad R_{sN}] \tag{4.18b}$$

and

$$\underset{\sim}{V}_a = [\underset{\sim}{V}_{s1}^T \quad \underset{\sim}{V}_{s2}^T \quad \cdots \quad \underset{\sim}{V}_{sN}^T]^T \tag{4.18c}$$

Moreover, C_a and L_a^T are block diagonal matrices of substructure connectivity and interpolation matrices and T is the substructure to arm connectivity matrix, a rectangular matrix. Next, let

$$\underset{\sim}{V}_a = A\underset{\sim}{q} \tag{4.19}$$

where $\underset{\sim}{q}$ is a vector of generalized coordinates and A is a matrix to be determined. To determine A in terms of substructure admissible vectors, we consider the disjoint substructure nodal coordinate vector for one arm, which can be expressed as follows:

$$\underset{\sim}{V}_{da} = T\underset{\sim}{V}_{a} \tag{4.20}$$

Premultiplying by T^T and solving for $\underset{\sim}{V}_a$, we obtain

$$\underset{\sim}{V}_{a} = (T^TT)^{-1}T^T\underset{\sim}{V}_{da} \tag{4.21}$$

Now consider the block-diagonal matrix of admissible vectors Q for the disjoint substructures, where Q is such that

$$\underset{\sim}{V}_{da} = Q\underset{\sim}{q} \tag{4.22}$$

Inserting Eq. (4.22) into Eq. (4.21), we have

$$\underset{\sim}{V}_{a} = (T^TT)^{-1}T^TQ\underset{\sim}{q} \tag{4.23}$$

so that, from Eqs. (4.23) and (4.19), we conclude that

$$A = (T^TT)^{-1}T^TQ \tag{4.24}$$

For the finite element case, we can let Q = T so that A becomes an identity matrix.

From Eqs. (4.7), (4.18a) and (4.19) the matrix of admissible functions for an arm can be expressed as

$$\phi = R_aL_a^TC_aTA \tag{4.25}$$

Considering Eq. (4.21), the order of the matrix T can be so large that the inverse of T^TT may prove troublesome. Fortunately, the matrix T is a connectivity and coordinate transformation matrix so that T^TT is diagonal and positive definite. Hence, the solution exists for any number of substructure connections or admissible vectors. Note that in general it is not actually necessary to form the matrix T, and in fact the matrix product TA in Eq. (4.25) is the desired quantity and can be formed quite simply with no large-order matrix multiplications. This makes the computational aspects of the method very attractive.

To determine $\bar{\Phi}$, Φ must be integrated over the mass of the arm according to Eqs. (4.11). The result is

$$\bar{\Phi} = R_a \bar{L}_a^T C_a TA \tag{4.26}$$

where

$$\bar{L}_a^T = \int_m L_a^T dm = h \int_0^1 m(\zeta) L_a^T d\zeta \tag{4.27}$$

From Eqs. (4.11) and (4.25) it can be shown that

$$\tilde{\Phi}_u = \left[[I_{11}\ I_{21} \cdots I_{n1}]C_1 \cdots [I_{1N}\ I_{2N} \cdots I_{nN}]C_N\ TA \right] \tag{4.28}$$

where

$$I_{i\ell} = \int_m [\tilde{r}_E + \tilde{\sigma}]^T R_i L_{ui}^T\, dm \tag{4.29}$$

where the subscript ℓ denotes the substructure and the subscript i the element. Note that $\tilde{r}_E$ and $\tilde{\sigma}$ are represented in the coordinate system $x_0y_0z_0$.

From Fig. 4.4, we see that for the i^{th} element

$$\underset{\sim}{r} + \underset{\sim}{\rho} = \underset{\sim}{r} + \underset{\sim}{\rho}_{j-1} + R_i x \hat{\underset{\sim}{u}}_1 \tag{4.30}$$

where

$$\hat{\underset{\sim}{u}}_1 = [1 \quad 0 \quad 0]^T \tag{4.31}$$

so that

$$[\tilde{r} + \tilde{\rho}] = [\tilde{r} + \tilde{\rho}_{j-1}] + x\widetilde{[R_i \hat{\underset{\sim}{u}}_1]} \tag{4.32}$$

and Eq. (4.29) becomes

$$I_{i\ell} = [\tilde{r} + \tilde{\rho}_{j-1}]^T R_i \bar{L}_{ui}^T + D L_{ui}^T \tag{4.33}$$

where

$$L_{ui}^T = \int_0^h x L_{ui}^T \, m(x) dx \tag{4.34}$$

and

$$D = \widetilde{[R_i \hat{\underset{\sim}{u}}_1]}^T R_i \tag{4.35}$$

As soon as Φ is determined, we can compute the mass and stiffness matrices for arm i. From Eqs. (4.11) and (4.25), the mass matrix for arm i can be expressed as

$$M_i = A_i^T T_i^T C_{ai}^T \left(\int_{m_i} L_{ai} L_{ai}^T \, dm_i \right) C_{ai} T_i A_i \tag{4.36}$$

The integration is the conventional finite element integration. In fact, denoting the finite element mass matrix for substructure j as M_{Fj}, we have

$$M_i = A_i^T T_i^T \left[\begin{array}{cc} M_{Fj} & \\ & \end{array}\right]_i T_i A_i \qquad (4.37)$$

where the quantity in the brackets is the block-diagonal matrix of the N substructures' finite element mass matrices of arm i. Similarly, the stiffness matrix for arm i can be shown to be

$$K_i = A_i^T T_i^T \left[\begin{array}{cc} K_{fj} & \\ & \end{array}\right]_i T_i A_i \qquad (4.38)$$

In practice, matrices M_i and K_i can be pieced together one substructure at a time, avoiding large-order matrix multiplications and storage difficulties. In fact, the substructure connectivity matrix C and the appendage connectivity matrix T are only symbolic and need not be computed in full form. The matrix A defined by Eq. (4.24) represents the matrix of admissible vectors for the appendage as a whole, which is a least-squares approximation of the matrix of disjoint admissible vectors Q. However, this approximation preserves the admissibility of the vectors and provides exact substructure connectivity.

4.4 NUMERICAL RESULTS

The least-squares approach to substructure synthesis was used to compute the eigensolution of the satellite configuration of Fig. 4.5, which represents an INTELSAT satellite. The small triangles denote

nodal positions and the dashed lines represent rigid bodies. The dimensions are shown on Figs. 4.7 and 4.8. Figure 4.6 is an exploded view of the satellite showing the individual substructures making up each arm. An arm of the structure is identified with a number and each substructure of that arm is identified with a lower case letter. Each substructure's nodal connections are characterized by a symbol to be matched with that of connected substructures of the same arm. Lumped inertias are identified with a small circle at the node and the letter L. For instance, the dish antennas are denoted by L_2, L_3, L_4 and L_5. The solar panels 1b and 2b are modeled as lattice frameworks of beams connected to the main spars 1a and 2a, at five nodes each.

Table 4.1 shows the material properties for the elements of the substructures. Each substructure contains uniform homogeneous, isotropic, tubular elements. Substructures 1a, 2a, 3a, 3b, 3c, 3d, and 3e, have material properties (1) and substructures 1b, 2b, 4a, 5a have material properties (2). The inertia properties of the rigid structures can be found in Table 4.2.

The satellite eigenvalue problem corresponding to 288 degrees of freedom was first solved for the finite element case, that is, letting Q = T in Eq. (4.24).

Several flexible modes and their eigenvalues are shown in Figs. 4.9 through 4.14. The dashed lines represent the undeformed structure. The viewing orientation is the same as on Fig. 4.1 showing z_0, y_0, x_0 rotations viewed from the top at 16°, 30°, -60°, respectively. The diamond symbols on arm 3 dish antennas are reference marks to demonstrate in-plane antenna orientation.

The first flexible mode, Fig. 4.9, shows motion about the z_0 axis, with the arm 3 rotation in the negative z_0 direction balanced by the rest of the structures rotation in the positive z_0 direction. The second and fourth flexible modes, Figs. 4.10 and 4.12, are similar to mode one, but with rotations about the x_0 and y_0 axes, respectively. Figures 4.11 and 4.12 show modes with out-of-plane symmetric and antisymmetric solar panel motion. Mode 11, Fig. 4.13, shows in-plane symmetric solar panel motion. Mode 16, Figs. 4.14a and 4.14b, gives a good demonstration of the coupling between substructures. Figure 4.14b is a top view of mode 16, showing torsional motion of the hub and arm 3 antenna dishes.

Admissible vectors were then applied to the same finite element configuration to reduce the order of the system. Discretized cantilever beam modes were used as admissible vectors for substructures 1a and 2a and polynomials were used for the remaining substructures. The resulting eigenvalues and required C.P.U. time for eigensolution of the lower modes for varying numbers of admissible vectors can be found on Table 4.3, for comparison with the finite element method. The modal plots for the lower modes of the 164 degrees of freedom case were almost identical to the finite element case.

Since substructure connectivity is satisfied exactly, the FEM provides a lower bound for the substructure synthesis solution. Referring to Table 4.3, increasing the degrees of freedom increases the number of accurate eigenvalues but with a corresponding price of increased computer time. The placement of the admissible vectors is as

important as their quantity and type. For instance, a particular mode involves participation of certain substructures in certain directions. A self-adaptive computer scheme would be useful to determine the optimal placement of admissible vectors to yield convergence to the desired modes with a minimum of degrees of freedom.

The least-squares approach to substructure synthesis allows for simple, robust and computationally efficient assembly of the global mass and stiffness matrices. The admissible vectors are altered in the process, although they remain admissible. Hence, if it is desireable to apply a particular set of admissible vectors exactly to a substructure, the method is not applicable. Fortunately, this is rarely necessary.

TABLE 4.1 - Element Properties

	Stiffness			Inertia	
	Bending EI ($N \cdot m^2$)	Torsion GJ ($N \cdot m^2$)	Axial EA (N)	Mass m/h(kg/m)	Moment Ixx/m(m^2)
1	1.2×10^5	8.856×10^4	1.061×10^8	4.047	2.262×10^{-3}
2	1.095×10^4	8.081×10^3	4.108×10^7	1.567	5.33×10^{-4}

TABLE 4.2 - Lumped Mass Properties

	M_{sub} (kg)	I_{xx} ($kg \cdot m^2$)	I_{yy} ($kg \cdot m^2$)	I_{zz} ($kg \cdot m^2$)
Hub	3000	10,250	7250	5000
L_1	5	.0577	.0577	.104
L_2	80	213	213	426
L_3	60	99.3	99.3	198
L_4	25	10.7	10.7	21.3
L_5	15	2.5	2.5	5.0

TABLE 4.3 - Eigenvalues$(rad/sec)^2$

D.O.F	288(FEM)	107	139	164
C.P.U. (Sec)	120	8	12	18
Mode Number				
7	.961917	.969968	.969910	.965418
8	1.635424	1.635868	1.635770	1.635637
9	2.756513	2.835586	2.761894	2.758077
10	2.850234	2.887633	2.853221	2.851125
11	2.950203	3.380016	3.380008	3.128286
12	8.231409	8.273952	8.273910	8.231678
13	8.403138	8.413098	8.410894	8.410011
14	11.843087	11.884216	11.857294	11.848375
15	15.507217	15.863589	15.581922	15.540388
16	17.560972	20.892035	20.887355	18.991691
17	27.855638	28.118613	28.037233	27.867882
18	38.819576	48.582855	40.548563	38.953338
19	41.235337	48.888657	43.034113	41.377077
20	47.367909	51.722272	48.518211	47.370011
21	97.360301	112.531835	112.383214	97.365096
22	111.667137	121.516131	114.408989	111.938805
23	119.618554	125.659352	121.838180	119.812174
24	134.525889	136.219864	136.213995	135.610984
25	136.234593	141.043348	138.483730	137.425559
26	137.927422	163.919721	163.910643	159.662671

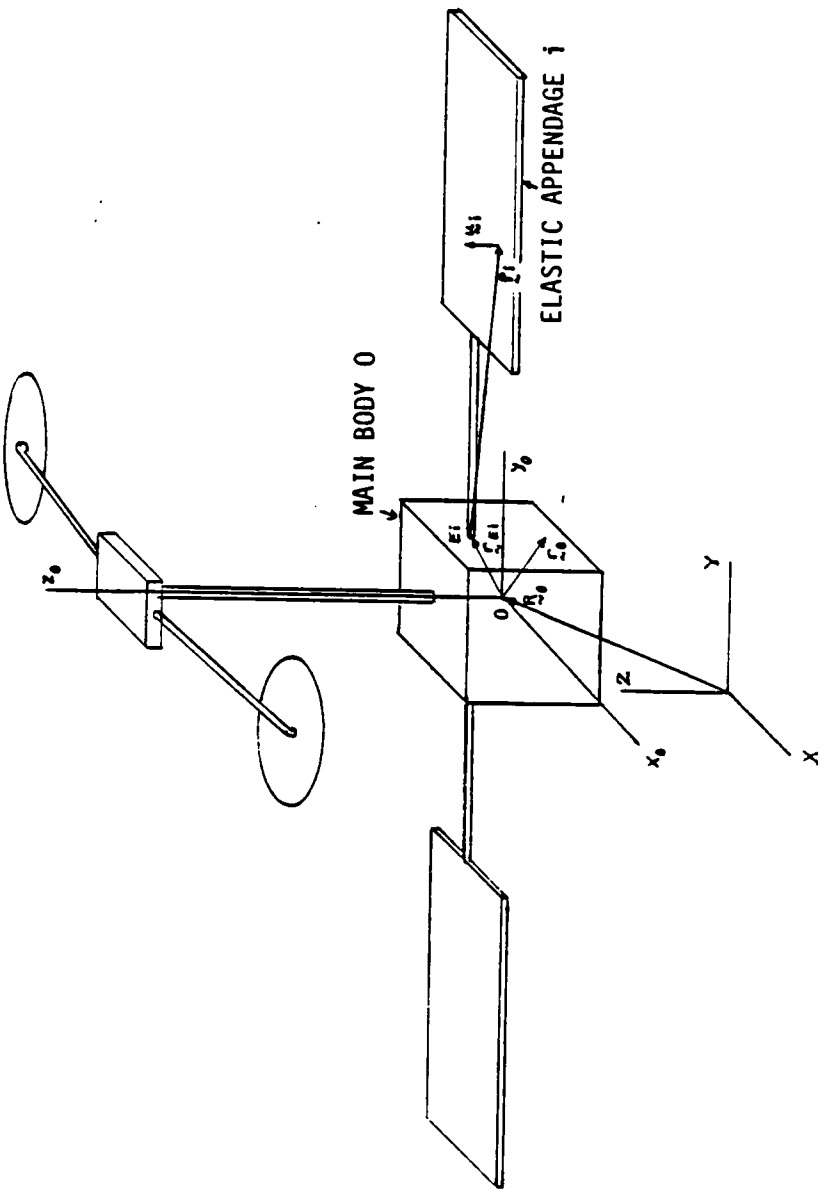

Figure 4.1 Multi-appendage flexible satellite.

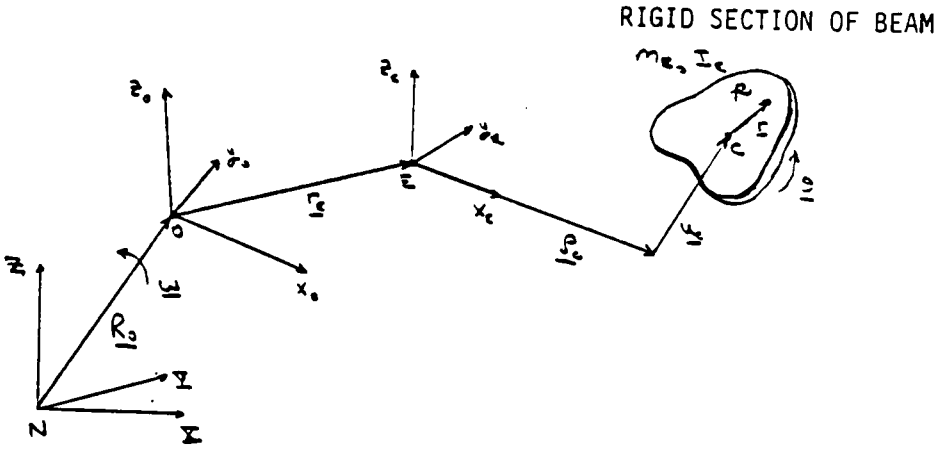

Figure 4.2 Kinematics of rigid cross-section of beam.

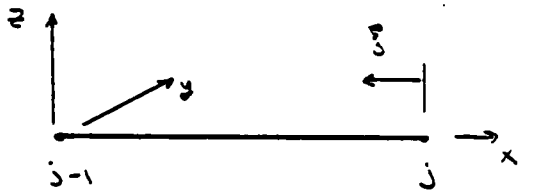

Figure 4.3 Idealized finite element model for beam.

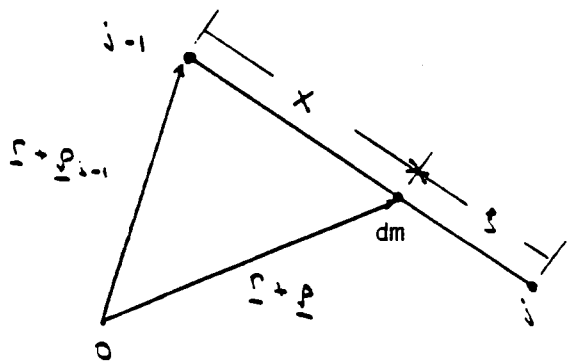

Figure 4.4 Kinematics of beam element.

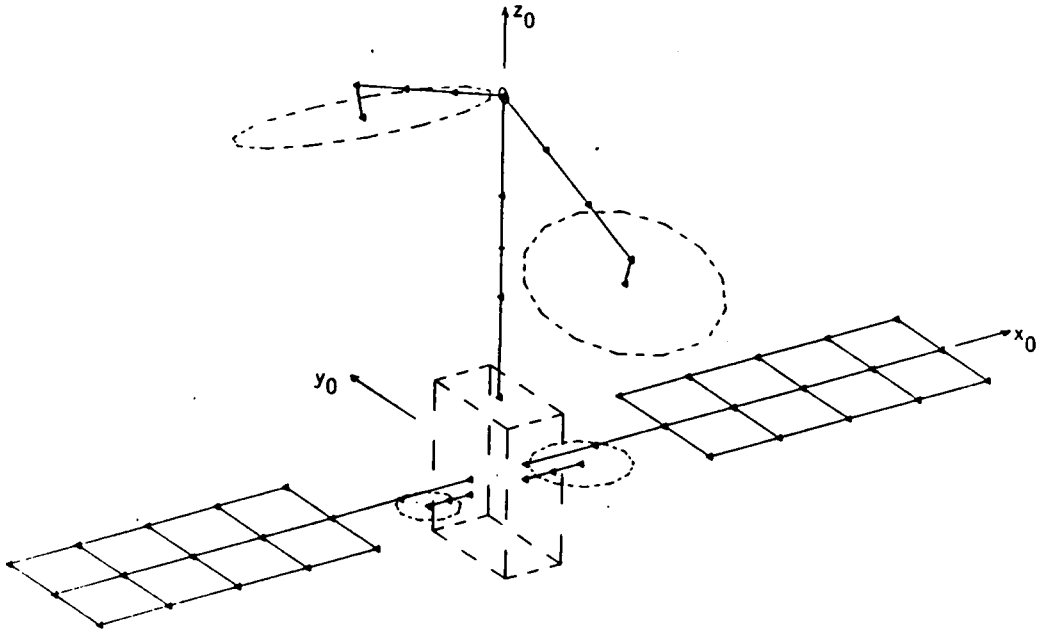

Figure 4.5 Satellite configuration showing nodal locations.

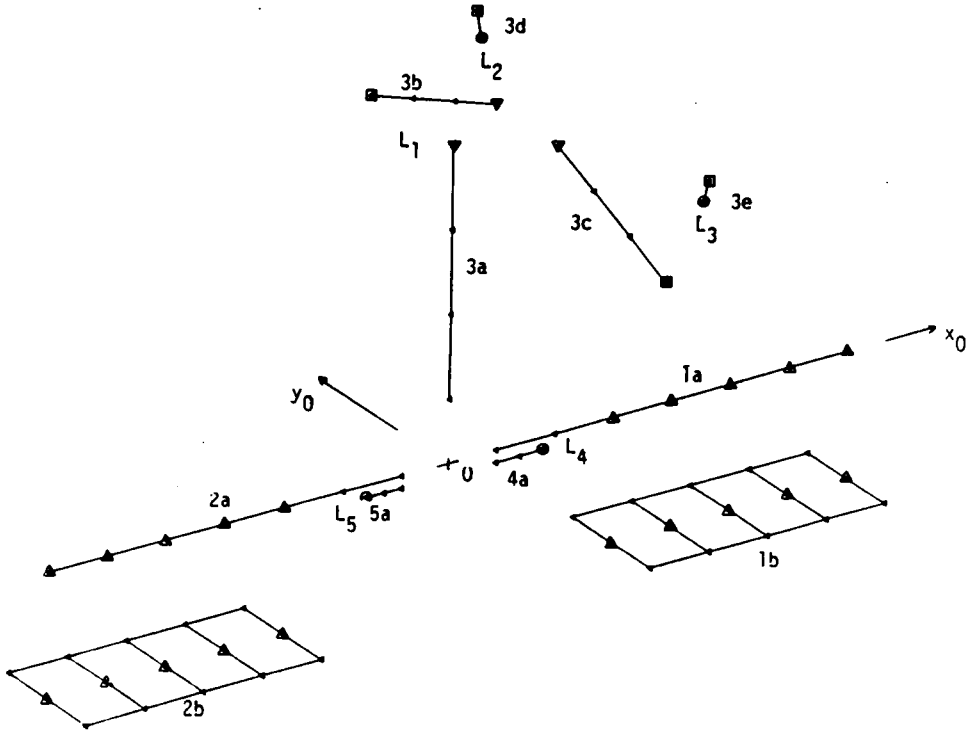

Figure 4.6 Exploded view of satellite showing substructures.

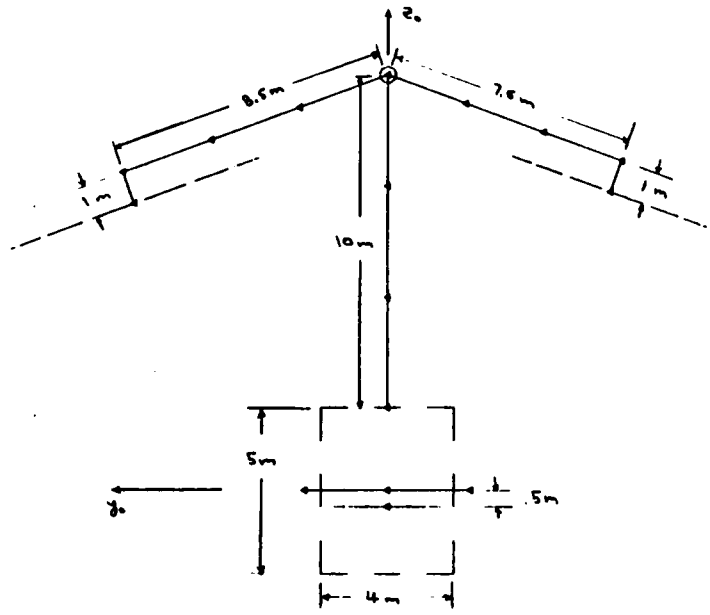

Figure 4.7 Satellite dimensions in y_0, z_0 plane.

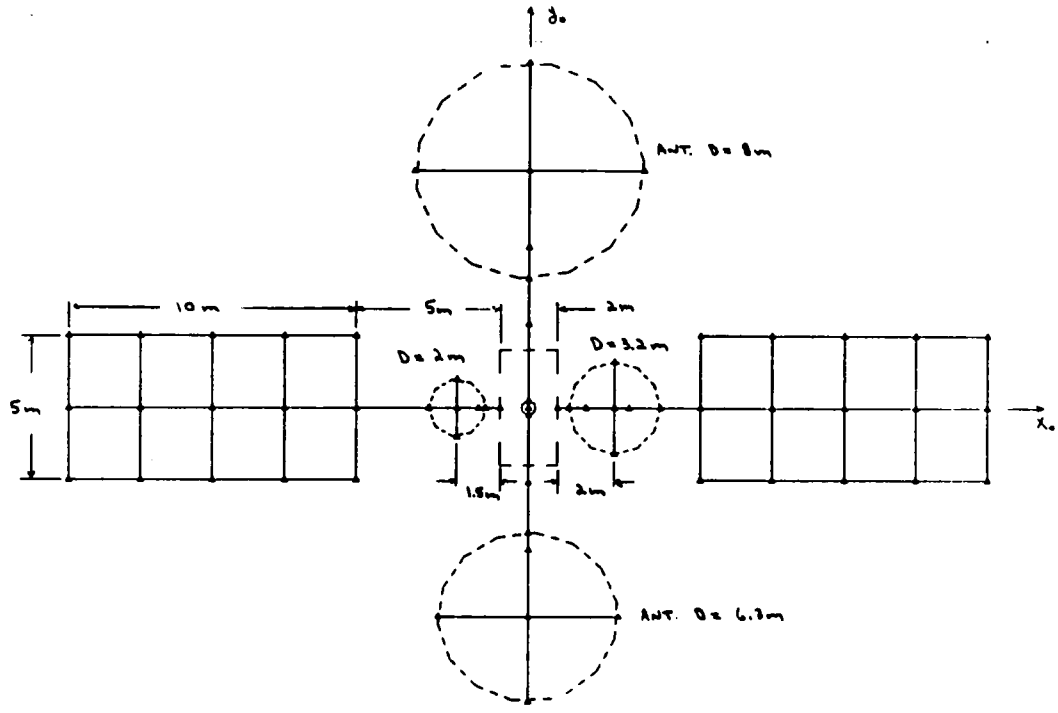

Figure 4.8 Satellite dimensions in x_0, y_0 plane.

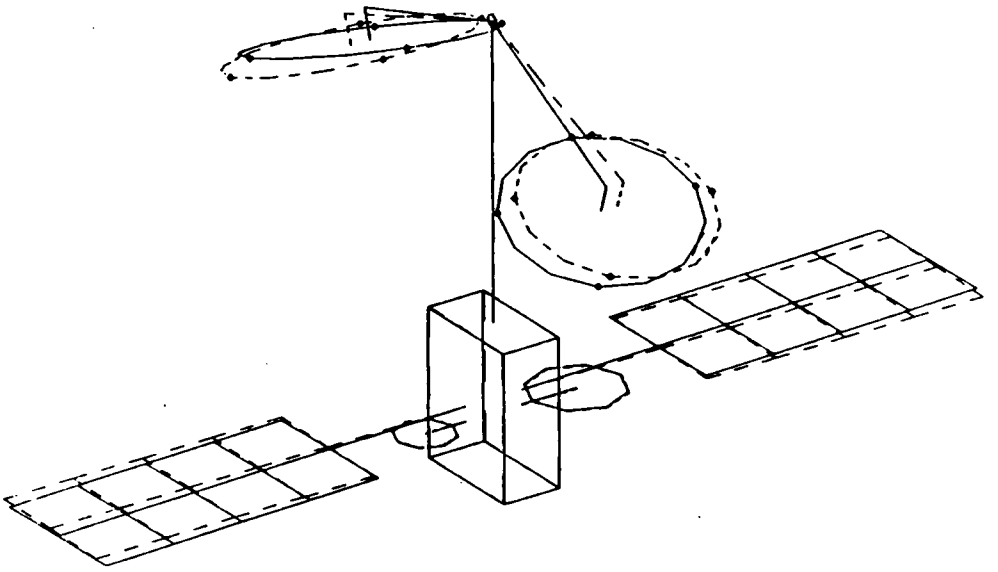

Figure 4.9 Satellite mode 7.

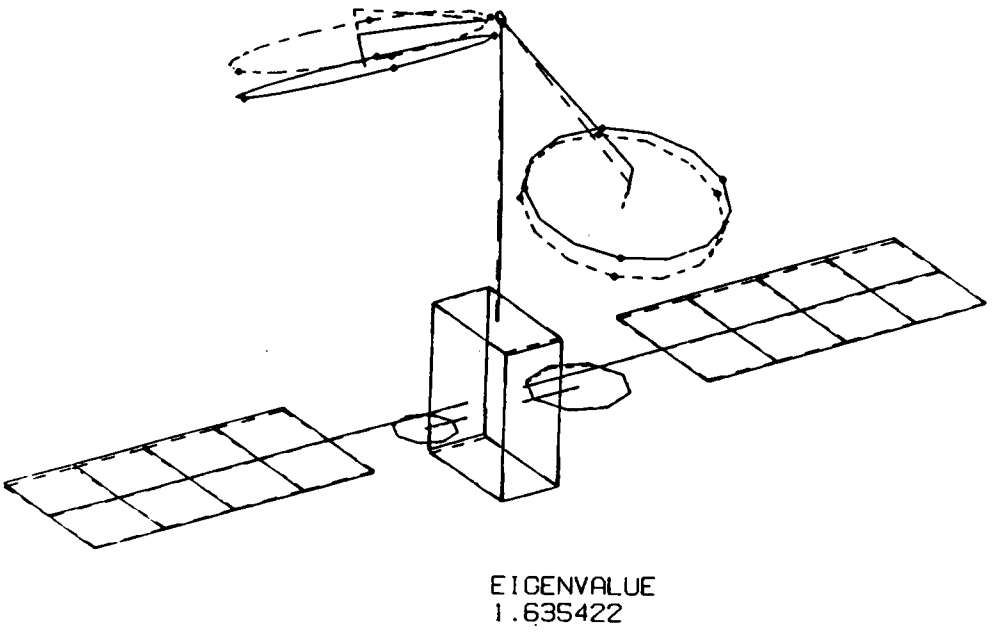

Figure 4.10 Satellite mode 8.

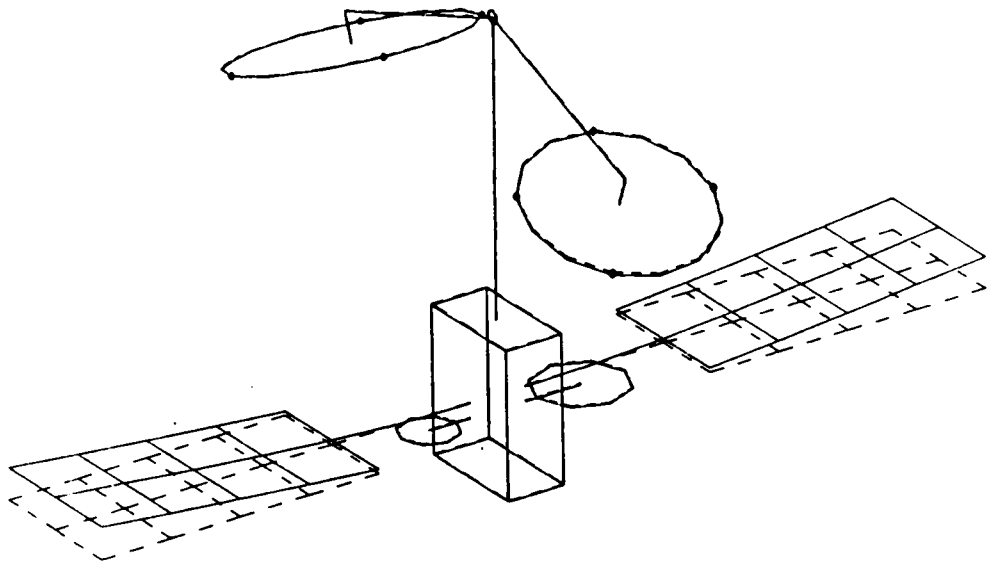

Figure 4.11 Satellite mode 9.

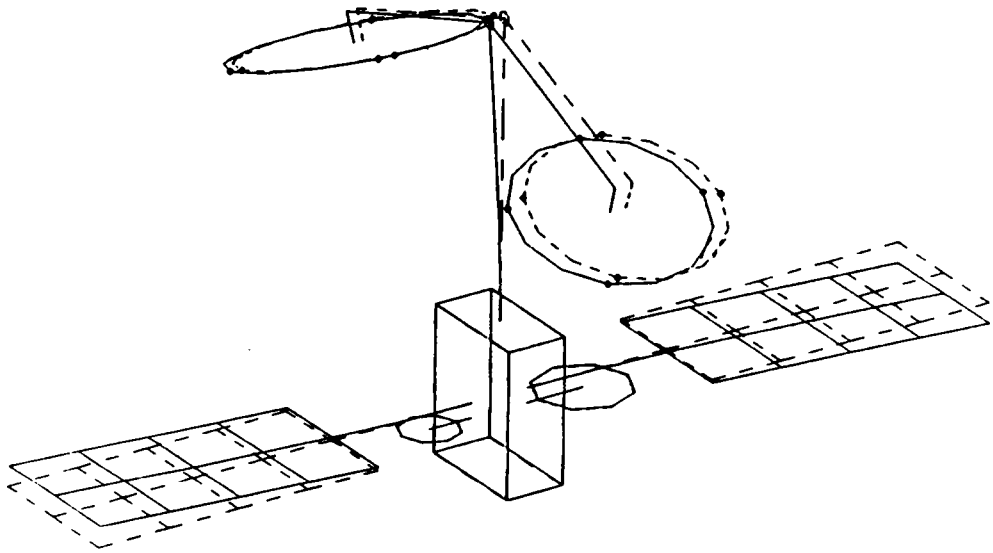

Figure 4.12 Satellite mode 10.

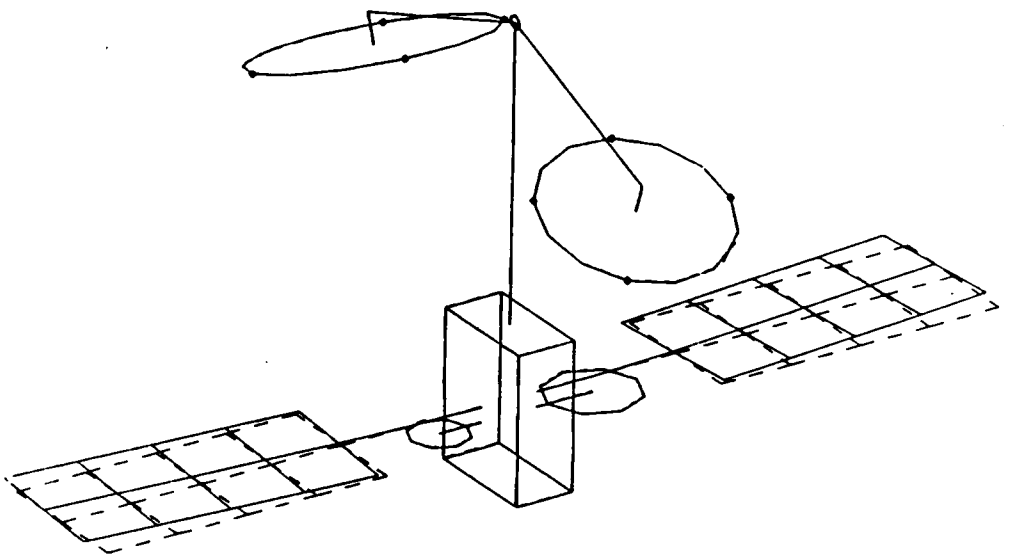

Figure 4.13 Satellite mode 11.

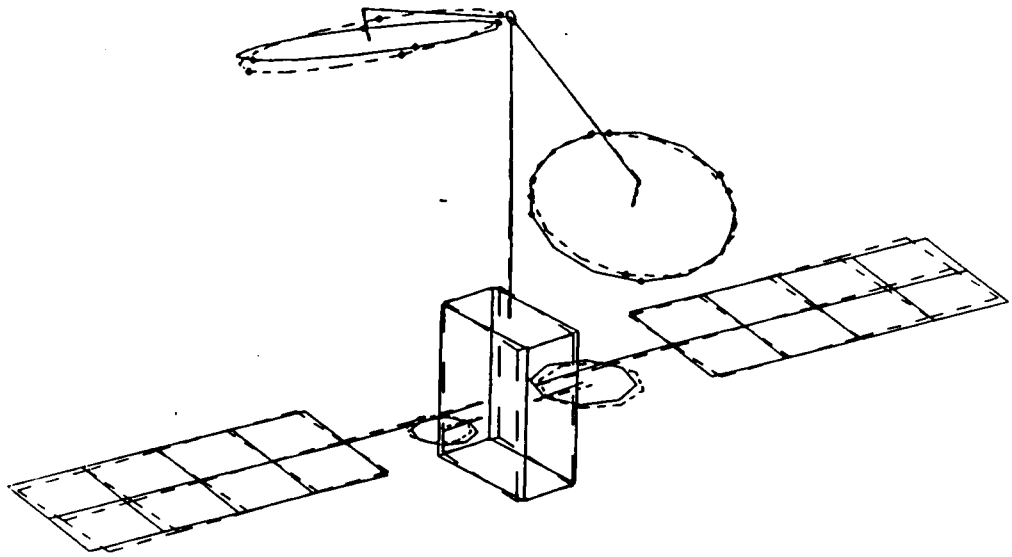

a) Standard View

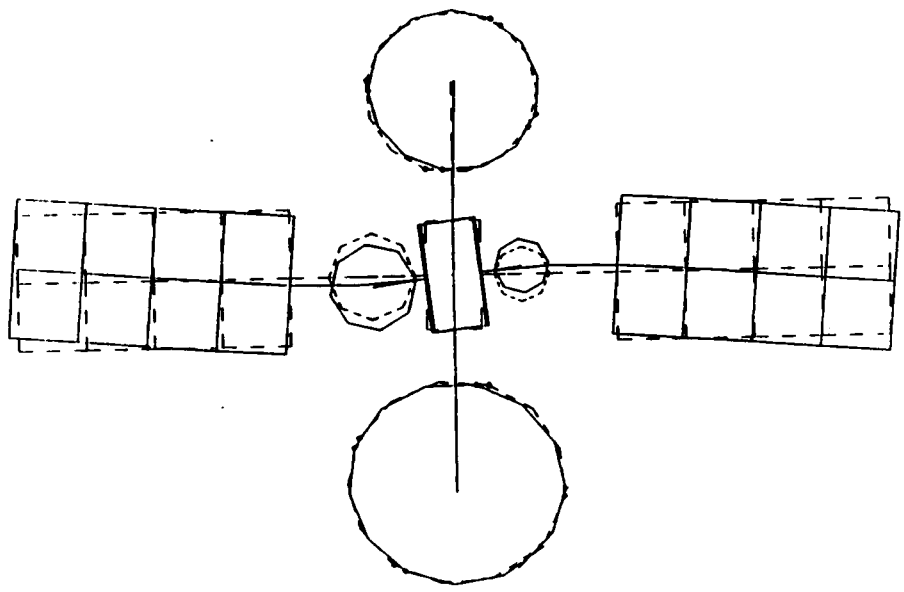

b) Top view

Figure 4.14 Satellite mode 16.

CHAPTER V

MANEUVERS: RIGID-BODY ROTATIONS

5.1 INTRODUCTION

In chapter 3, the nonlinear equations of motion were transformed via a perturbation technique to two sets of equations, a set governing the rigid-body maneuver and a set governing the first-order deviations from the rigid-body maneuver. In this chapter, an open-loop control strategy for minimum-time, single-axis rotational maneuvers of a rigid-body is discussed. The maneuver need not be about the center of mass and the axis of rotation is not necessarily a principal axis. The analysis considers actuator dynamics. The control strategy is first developed for continuous time and then adapted to discrete time.

Finally, the moment required for the maneuver is discussed for the case of a flexible structure. The most efficient way of applying the moment is the one in which only the desired rigid-body motion is excited by the actuators. A force distribution yielding a moment exhibiting these characteristics is developed. For the case of spatially discrete actuators, the actuator placement for the most efficient, rigid-body control performance is also discussed.

5.2 ROTATION ABOUT A PRINCIPAL AXIS

Consider a rotation of the structure about a principal axis. The governing equation for such a maneuver can be expressed as

$$M_0(t) = I_0\ddot{\theta}(t) \tag{5.1}$$

where $\ddot{\theta}(t)$ is the desired angular acceleration, $M_0(t)$ is the moment

about the rotational axis. The response of the actuators to the command moment is assumed to be of first-order. Hence, the equation of motion of the actuator takes the form

$$\dot{M}_0(t) = aM_0(t) + bM_c(t) \tag{5.2}$$

where $M_0(t)$ is the applied moment, $-M_{max} \leq M_c(t) \leq M_{max}$ is the command moment at time t and M_{max} is the maximum available command moment. Dividing Eq. (5.2) by I_0 and inserting Eq. (5.1) into Eq. (5.2) yields

$$\dddot{\theta}(t) = a\ddot{\theta}(t) + b'u(t) \tag{5.3a}$$

where

$$b' = \frac{bM_{max}}{I_0} \tag{5.3b}$$

and $u = M_c / M_{max}$ is the control command so that $-1.0 < u < 1.0$. The state equations can then be expressed as

$$\dot{\underset{\sim}{x}}(t) = A\underset{\sim}{x}(t) + \underset{\sim}{b}u(t) \tag{5.4a}$$

where

$$\underset{\sim}{x}^T = [\theta \ \dot{\theta} \ \ddot{\theta}] \tag{5.4b}$$

$$A = \begin{bmatrix} 0 & 1 & 0 \\ 0 & 0 & 1 \\ 0 & 0 & a \end{bmatrix} \tag{5.4c}$$

$$\underset{\sim}{b}^T = [0 \ 0 \ b'] \tag{5.4d}$$

Thus, the control problem can be classified as a stationary, linear regulator, minimum-time problem and the solution is bang-bang control. The eigenvalues of matrix A are (a,0,0), which are real and nonpositive if $a \leq 0$, so that a unique optimal control exists and the control component will switch a maximum of two times. Also, since the controllability matrix

$$C = [\underset{\sim}{b}\ A\underset{\sim}{b}\ A^2\underset{\sim}{b}] = \begin{bmatrix} 0 & 0 & b' \\ 0 & b' & ab' \\ b' & ab' & a^2b' \end{bmatrix} \tag{5.5}$$

is non singular for $a < 0$ and $b < 0$, the system is controllable and no singular intervals exist in the optimal control policy (Ref. 10). The lack of singular intervals means that u can be determined at all times during the maneuver and will be equal to +1 or -1. The solution of Eq. (5.4a) can be expressed as

$$\underset{\sim}{x}(t) = \phi(t)\underset{\sim}{x}(0) + \underset{\sim}{\Gamma}(t)u(t) \tag{5.6}$$

where

$$\phi(t) = e^{At} = \begin{bmatrix} 1 & t & \frac{e^{at}}{a^2} - \frac{t}{a} - \frac{1}{a^2} \\ 0 & 1 & \frac{e^{at}}{a} - \frac{1}{a} \\ 0 & 0 & e^{at} \end{bmatrix} \tag{5.6a}$$

is the transition matrix and

$$\underset{\sim}{\Gamma}^T(t) = b' \begin{bmatrix} \frac{t^2}{2} - \frac{e^{at}}{a^2} + \frac{t}{a} - \frac{1}{a^2} & t - \frac{e^{at}}{a} + \frac{1}{a} & 1 - e^{at} \end{bmatrix} \quad (5.6b)$$

Hence, with the initial and final states x_0 and x_f known, and assuming that initially u = +1, the nine equations

$$\begin{aligned} \underset{\sim}{x}_1 &= e^{At_1} \underset{\sim}{x}_0 + \underset{\sim}{\Gamma}(t_1) \\ \underset{\sim}{x}_2 &= e^{A(t_2 - t_1)} \underset{\sim}{x}_1 - \underset{\sim}{\Gamma}(t_2 - t_1) \\ \underset{\sim}{x}_f &= e^{A(t_f - t_2)} \underset{\sim}{x}_2 + \underset{\sim}{\Gamma}(t_f - t_2) \end{aligned} \quad (5.7a\text{-}c)$$

can be solved for the two switching times t_1 and t_2, the final time t_f, and the states at the switching times $\underset{\sim}{x}_1$ and $\underset{\sim}{x}_2$. Equations (5.7) can be reduced by variable substitution to three nonlinear equations and solved numerically for t_1, t_2 and t_f. With the switching times known, Eqs. (5.7) can be used to find the state trajectory during the maneuver.

In the previous analysis it was assumed that the command moments could be switched at any time. However, the commands must actually be applied in discrete time so that the switching times must be multiples of the sampling period. The discrete maneuver strategy can follow closely the optimal continuous strategy if the sampling time is small compared to the total maneuver time. Optimal discrete switching times can be found by perturbing the continuous switching times while minimizing the difference between the discrete-time trajectory and the

continuous-time trajectory. Note that the closed-loop vibration control discussed in Chapter 7 can further reduce this difference during the actual maneuver.

5.3 GENERAL ROTATIONAL MANEUVERS

In Section 5.2 the rotational maneuver was assumed to be about a principal axis. The analysis is now extended by relaxing this assumption. Equations (3.11) govern the motion of a rigid-body during a maneuver and can be expressed as

$$mC_0\ddot{\underset{\sim}{R}}_0 + \tilde{\underset{\sim}{S}}_0\dot{\underset{\sim}{\omega}} + \tilde{\underset{\sim}{\omega}}_0^T\tilde{\underset{\sim}{S}}_0\underset{\sim}{\omega}_0 = \underset{\sim}{F}_0 \tag{5.8a}$$

$$\tilde{\underset{\sim}{S}}_0^T C_0\ddot{\underset{\sim}{R}}_0 + I_0\dot{\underset{\sim}{\omega}}_0 + \tilde{\underset{\sim}{\omega}}_0^T I_0\underset{\sim}{\omega}_0 = \underset{\sim}{M}_0 \tag{5.8b}$$

where the gravitational terms have been neglected and Eq. (3.11a) has been premultiplied by C_0. The gravitational effects are treated in Chapter 7. A rotation about the 1 axis that begins and ends at rest can be characterized by the expressions

$$\omega_{01} = \dot{\theta}(t) \tag{5.9a}$$

$$\omega_{02} = \omega_{03} = \dot{R}_{01} = \dot{R}_{02} = \dot{R}_{03} = 0 \tag{5.9b}$$

where ω_{0i} and $\dot{R}_{0i}$ $(i = 1,2,3)$ are the components of $\underset{\sim}{\omega}_0$ and $\dot{\underset{\sim}{R}}_0$, respectively, and $\theta(t)$ is the desired time history of the rotational angle. Introducing Eqs. (5.9) into Eqs. (5.8), we obtain

$$F_{01} = 0 \tag{5.10a}$$

$$F_{02} = S_{21}\ddot{\theta} - S_{31}\dot{\theta}^2 \tag{5.10b}$$

$$F_{03} = S_{31}\ddot{\theta} + S_{21}\dot{\theta}^2 \tag{5.10c}$$

$$M_{01} = I_{11}\ddot{\theta} \tag{5.10d}$$

$$M_{02} = I_{21}\ddot{\theta} - I_{31}\dot{\theta}^2 \tag{5.10e}$$

$$M_{03} = I_{31}\ddot{\theta} + I_{21}\dot{\theta}^2 \tag{5.10f}$$

where F_{01}, F_{02}, F_{03}, and M_{01}, M_{02}, M_{03} are the required forces and moments in the 1, 2 and 3 directions, respectively, producing the desired time history given by Eqs. (5.9). Eq. (5.10d) is identical to Eq. (5.1), so that the previous analysis applies for this situation in determining $M_{01}(t)$ and $\theta(t)$. Since this is an open-loop strategy, $M_{02}(t)$ and $M_{03}(t)$ can be determined from Eqs. (5.10e) and (5.10f) as soon as $\theta(t)$ is known. Equation (5.2) can be solved for $M_c(t)$, so that the command moments needed to produce $M_{02}(t)$ and $M_{03}(t)$ can also be determined. The same argument applies for determining the necessary force commands to achieve the desired forces of Eqs. (5.10a-c). Some error can be expected to occur because the command moments can only be updated at multiples of the sampling period, while θ varies continuously in time. For many useful cases, such as for SCOLE, the rotational axis is close to a principal axis so that the off-diagonal terms of the inertia matrix appearing in Eqs. (5.10e,f) are relatively small. For these cases the error can be insignificant. Equations (5.8) are nonlinear so that the solution given by Eqs. (5.10) may not be stable.

However, the closed-loop vibrational control of Chapter 7 can stabilize the spacecraft as well as reduce the error caused by discrete-time sampling.

5.4 MANEUVER FORCE IMPLEMENTATION FOR A FLEXIBLE STRUCTURE

The most desirable control technique for a maneuver excites only the desired rigid-body motion, not the elastic modes. The obvious method is to apply a distributed force that is proportional to the rigid-body mode corresponding to the direction of the desired moment. Because the modes are orthogonal, the other modes are not excited by this force, although they may be excited by centrifugal forces during the maneuver. Of course, a distributed force can only be implemented approximately with discrete actuators, which tends to excite the other modes somewhat.

For simplicity, consider a rotation about a principal axis. The equation governing such a maneuver was expressed previously by Eq. (5.1). For reasons mentioned above, we wish to apply the moment by means of distributed actuators, so that $M_0(t)$ is the resultant moment produced by forces $F(p,t)$ distributed throughout the structure or

$$M_0(t) = \int_D r(p)F(p,t)dD \tag{5.11}$$

where $r(p)$ is the distance from the axis of rotation to a typical point p. Introducing the definition of I_0 and Eq. (5.11) into Eq. (5.1), the equation governing the maneuver can be expressed as

$$\int_D r(p)F(p,t)\,dD = \int_D \ddot{\theta}(t)m(p)r^2(p)\,dD \tag{5.12}$$

where m(p) is the mass density of the structure at point p. Considering Eq. (5.12), and consistent with our desire for the force to be proportional to the rotational mode, the force density can be expressed as

$$F(p,t) = \ddot{\theta}(t)m(p)r(p) \tag{5.13}$$

Because the force is proportional to the rotational mode, it is orthogonal to all the other modes, so that it will excite only the desired rotational maneuver. Note that the force is also proportional to the mass, so that the mass acts as the control gain. This suggests that when this force is applied with discrete actuators, the actuators should be located at the points of maximum mass for maximum efficiency in rigid-body control. Of course, analogously, when spatially discrete moment actuators are available, they should be located at the points of maximum mass moment of inertia. The application of the desired forces and moments with discrete actuators will be discussed in Chapter 7.

When the rotational axis is not a principal axis, Eqs. (5.10d-f) express the required moments. The moment vector can be expressed as

$$\underset{\sim}{M}(t) = \int_D \underset{\sim}{r}(p) \times \underset{\sim}{F}(p,t)\,dD \tag{5.14a}$$

where

$$\underset{\sim}{r}^T = [x \quad y \quad z] \tag{5.14b}$$

$$\underset{\sim}{F}^T(p,t) = [F_1(p,t) \quad F_2(p,t) \quad F_3(p,t)] \tag{5.14c}$$

are the position vector and force vector of a point on the body corresponding to mass density m(p). Introducing the definition of the inertia matrix into Eqs. (5.10 d-f) and comparing the resulting equations with Eq. (5.14), the distributed actuating forces producing the desired moments can be expressed as

$$F_1(p,t) = x(p)m(p)\dot{\theta}^2(t) \tag{5.15a}$$

$$F_2(p,t) = -z(p)m(p)\ddot{\theta}(t) \tag{5.15b}$$

$$F_3(p,t) = y(p)m(p)\ddot{\theta}(t) \tag{5.15c}$$

As in the preceding analysis, the actuating forces are proportional to rotational rigid-body modes and will not excite the other modes.

For a translational maneuver, the analysis is analogous to the one for rotational maneuvers. The force should be proportional to the corresponding translational mode so that the desired force can be expressed as

$$F(p,t) = a_0(t)m(p) \tag{5.16}$$

where $a_0(t)$ is the desired translational acceleration. Note that a rotation about an arbitrary point results in a translation of the center of mass of the spacecraft.

CHAPTER VI

VIBRATION SIMULATION: DISCRETIZATION IN TIME

6.1 INTRODUCTION

The vibration problem is described by Eqs. (3.15), which are linear equations with known time-varying coefficients. The time-varying coefficients are functions of the maneuver time history, which was discussed in Chapter 5. In this chapter the numerical simulation of the first-order perturbations from the desired maneuver strategy is considered. The desired maneuver strategy was defined in the last chapter as the continuous-time maneuver history of the structure in its rigid state. Thus, the vibration problem includes rigid-body deviations from the desired trajectory as well as elastic deformations. The simulation is performed with numerical integration in discrete time.

A static analysis is performed on the vibrational problem to check the stability characteristics and to determine the static equilibrium configuration. This information can then be used as the initial state in the discrete-time simulation.

A truncated set of premaneuver eigenvectors are used as admissible vectors to reduce the number of first-order equations of motion used in both simulation and control. These admissible vectors do not decouple the equations of motion, but they do diagonalize the mass matrix. Hence, the formulation of the equations in state form can be carried out with little effort. The time-dependent coefficient matrices are simplified by making use of the fact that the maneuvers of interest are single-axis rotations.

6.2 STATIC ANALYSIS

For safety, the laboratory experiment must be designed so that the structure is stable at all times. This means that when the structure is rotated to its maximum maneuver angle, it will remain in this orientation or, at worst, oscillate about its initial position if no external torques are applied. For stability of the SCOLE model, the universal joint must be located at or above the true center of mass at all times. Of course, the true center of mass changes with elastic deformation. Hence, the universal joint's location must be chosen very carefully, especially for maneuver rotations not corresponding to the tether axis. A static analysis is very useful for checking the stability of the mathematical model and adjusting the universal joint's location in an iterative fashion to achieve stability at the desired orientation.

Gravity has a much stronger influence in the laboratory experiment, both because the force of gravity is greater, and because the opposing force is a point (cable) force rather than a body (centrifugal) force as with the orbiting structure. It has been previously assumed that the universal joint is in the vicinity of the rigid-body center of mass along the axes orthogonal to the cable. That is, point B is near the center of mass, or perhaps somewhere above it. We now wish to find the stable equilibrium orientation and elastic deflection of the structure for a given joint location. For the laboratory experiment, the static portions of Eqs. (3.17) can be expressed as

$$K_{ST}\underset{\sim}{x}_{ST} = \underset{\sim}{F}_{ST} \tag{6.1a}$$

where the static stiffness is

$$K_{ST} = \begin{bmatrix} K_C & 0 & 0 \\ 0 & \tilde{S}_B[\widetilde{C_{0g}}] & [\widetilde{C_{0g}}]\bar{\Phi} \\ 0 & \bar{\Phi}^T[\widetilde{C_{0g}}]^T & K_A \end{bmatrix} \tag{6.1b}$$

and the static force is

$$\underset{\sim}{F}_{ST} = \begin{bmatrix} -(m\Phi_B^T + \bar{\psi}^T)C_0\underset{\sim}{g} \\ \tilde{S}_B C_0 \underset{\sim}{g} \\ -\bar{\Phi}^T C_0 \underset{\sim}{g} \end{bmatrix} \tag{6.1c}$$

Equations (6.1) form a set of nonlinear algebraic equations which can be solved for $\underset{\sim}{x}_{ST}$, the static equilibrium orientation and elastic deflection of the structure. The elastic deflection is coupled with the angular orientation of the structure. The orientation about the longitudinal axis of the cable (direction of gravity) is arbitrary. This means that a rotation about this axis will not affect the static orientation or elastic deflections. Any orientation can be made to be the stable equilibrium position by properly locating the universal joint using Eqs. (6.1). Hence, a single-axis rotation not affected by gravity can be accomplished about any desired axis once the proper joint location has been determined.

6.3 EIGENVALUE PROBLEM: REDUCTION OF ORDER

The maneuvers of interest, as described in Chapter 5, are time-optimal rotations beginning and ending in a state of rest. The eigensolution of the structure before and after the maneuver will be the same if gravity is neglected or if the axis of rotation corresponds to the direction of gravity. During the maneuver, the gyroscopic and

stiffness matrices, and hence the eigenvalue problem, are functions of time. Solving the eigenvalue problem at each time step would be inefficient and of limited usefulness. However, a truncated set of the premaneuver eigenvectors can be used as a set of admissible vectors to reduce further the number of equations of motion. The equations in reduced form can then be solved using a discrete-time technique.

Equation (3.48) can be rewritten as

$$M\ddot{\underset{\sim}{x}}(t) + G(t)\dot{\underset{\sim}{x}}(t) + [K_0 + K_t(t)]\underset{\sim}{x}(t) = \underset{\sim}{F}^*(t) \tag{6.2}$$

where K_t consists of the time-varying and gravitational terms of the stiffness matrix and K_0 contains the remaining constant terms. The premaneuver equations of motion, neglecting gravity, can be expressed as

$$M\ddot{\underset{\sim}{x}}(t) + K_0\underset{\sim}{x}(t) = \underset{\sim}{F}^*(t) \tag{6.3}$$

Hence, the corresponding eigenvalue problem can be expressed as

$$K_0\underset{\sim}{X} = M\underset{\sim}{X}\lambda \tag{6.4}$$

where $\lambda = \omega^2$ is an eigenvalue, in which ω is a corresponding natural frequency and $\underset{\sim}{X}$ is the associated eigenvector.

Due to the nature of the discretization process, only the lower modes, say n modes, are accurate representations of the actual modes (Ref. 11). Of course, by increasing the number N of admissible functions in the original discretization process, we can increase the number n of accurate modes. The lower n modes can be arranged in the $N \times n$ matrix X of eigenvectors, which can be normalized as follows:

$$X^T M X = I \tag{6.5a}$$

where I is an $n \times n$ identity matrix and

$$X^T K_0 X = \Lambda \tag{6.5b}$$

where Λ is the $n \times n$ block-diagonal matrix of eigenvalues. Using the expansion theorem (Ref. 13), the displacement vector for the premaneuver problem can be approximated by a linear combination of the lower n modes as follows:

$$\underset{\sim}{x}(t) = X\underset{\sim}{u}(t) \tag{6.6}$$

where $\underset{\sim}{u}(t)$ is a vector of the first n natural coordinates, or modal coordinates of the structure. Inserting Eq. (6.6) into Eq. (6.3), premultiplying by X^T and introducing Eqs. (6.5), we obtain the decoupled modal equations

$$\ddot{u}_r(t) + \omega_r^2 u_r(t) = f_r(t) \quad r = 1,2,\ldots,n \tag{6.7}$$

where ω_r is the rth natural frequency. Moreover, the modal force $f_r(t)$ is the rth component of the modal force vector

$$\underset{\sim}{f}(t) = X^T \underset{\sim}{F}^*(t) \tag{6.8}$$

Note that modal equations similar to Eqs. (6.7) are obtained also in the case of distributed-parameter models, without discretization. The only difference is that for distributed systems $n \to \infty$. Fortunately, the vibrational energy in the higher modes dissipates more rapidly, so that the truncation implied in Eqs. (6.6), (6.7) and (6.8) is acceptable for our purposes.

During the maneuver, the eigensolution is time-dependent and Eq. (6.7) no longer applies. However, the above eigenvectors can be used as admissible vectors during the maneuver so that Eqs. (6.5), (6.6) and (6.8) are applicable. Introducing Eq. (6.6) into Eq. (6.2) and considering Eqs. (6.5) and (6.8) the first-order approximation to the equations of motion can be written in the form

$$\ddot{\underset{\sim}{u}}(t) + \bar{G}(t)\dot{\underset{\sim}{u}}(t) + [\Lambda + \bar{K}(t)]\underset{\sim}{u}(t) = \underset{\sim}{f}(t) \tag{6.9a}$$

where

$$\bar{G}(t) = X^T G(t) X, \quad \bar{K}(t) = X^T K_t(t) X \tag{6.9b,c}$$

are the reduced-order gyroscopic and stiffness matrices. The premaneuver eigenvectors have not decoupled the equations of motion. However, as the maneuver velocity decreases, the time-varying terms decrease in magnitude and the equations approach their uncoupled form. Note that Eq. (6.9a) is of order $n < N$, hence the equations of motion have been reduced in order. Also, the mass matrix has been reduced to the identity matrix, which is convenient for the next task of putting Eq. (6.9) in state space form.

6.4 SIMULATION

Equation (6.9a) can be expressed in state space form

$$\dot{\underset{\sim}{z}}(t) = A(t)\underset{\sim}{z}(t) + \underset{\sim}{Q}(t) \tag{6.10a}$$

where

$$\underset{\sim}{z}^T = [\underset{\sim}{u}^T \quad \dot{\underset{\sim}{u}}^T] \tag{6.10b}$$

$$A(t) = \left[\begin{array}{c|c} 0 & I \\ \hline -[\Lambda + \bar{K}(t)] & -\bar{G}(t) \end{array}\right] \tag{6.10c}$$

$$\underset{\sim}{Q}^T(t) = [\underset{\sim}{0}^T \quad \underset{\sim}{f}^T(t)] \tag{6.10d}$$

A discrete-time numerical technique could be applied directly to yield a solution of Eqs. (6.10a). A numerical integration would require the evaluation of $A(t)$, perhaps numerously, at each sampling time. However, for $A(t)$ to be evaluted, $\bar{K}(t)$ and $\bar{G}(t)$ must first be evaluated. This in

turn requires the evaluation of G(t) and K(t), defined in Chapter 3, and the multiplications suggested by Eqs. (6.9a-c). Note that the evaluation of terms such as J_0 in Eq. (3.16f) implies spatial integration at each time step. Hence, it is desirable to determine a method that lends itself to more efficient computations.

Given the definitions of the gyroscopic and stiffness matrices, Eq. (3.16e-g, 3.17d-f), these matrices can be expanded as follows:

$$G(t) = \omega_{01}G_1 + \omega_{02}G_2 + \omega_{03}G_3 \tag{6.11a}$$

$$\begin{aligned} K(t) = {} & K_0 + \dot{\omega}_{01}K_1 + \dot{\omega}_{02}K_2 + \dot{\omega}_{03}K_3 + \omega_{01}^2K_4 + \omega_{01}\omega_{02}K_5 \\ & + \omega_{01}\omega_{03}K_6 + \omega_{02}K_7 + \omega_{02}\omega_{03}^2K_8 + \omega_{03}^2K_9 \\ & + f_1(\alpha_1,\alpha_2,\alpha_3)K_{10} + F_{01}K_{11} + F_{02}K_{12} + F_{03}K_{13} \end{aligned} \tag{6.11b}$$

where G_1, G_2, G_3 and K_0 through K_{13} are time-invariant matrices and f_1 is a nonlinear function of the Euler angles. Note that K_0 was defined previously in Eq. (6.2). For simplicity, consider single-axis rotations beginning and ending in a state of rest, so that for a rotation about axis 1, $\omega_{02} = \omega_{03} = \dot{\omega}_{02} = \dot{\omega}_{03} = 0$ and $\underset{\sim}{F}_0 = 0$. Hence, Eqs. (6.11) can be simplified as follows:

$$G(t) = \dot{\theta}G_1 \tag{6.12a}$$

$$K(t) = K_0 + \ddot{\theta}K_1 + \dot{\theta}^2K_4 + f_2(\theta)K_g \tag{6.12b}$$

where $\dot{\theta} = \omega_{01}$, f_2 involves trigonometric functions of $\theta(t)$ and K_g contains the gravity terms of the stiffness matrix. The generalized force $\underset{\sim}{F}^*$ is also time varying and can be expressed as

$$\underset{\sim}{F}^*(t) = \ddot{\theta}\underset{\sim}{F}_1^* + \dot{\theta}^2\underset{\sim}{F}_2^* + h(\theta)\underset{\sim}{F}_g^* \tag{6.13}$$

where $\underset{\sim}{F}_1^*$, $\underset{\sim}{F}_2^*$ and $\underset{\sim}{F}_g^*$ are time-invariant vectors and h is a function of

the angle θ. The choice of axis 1 as the rotational axis does not limit the usefulness of these equations since the equations of motion can be transformed cyclicly so that any desired axis can correspond to the 1 axis.

Introducing Eqs. (6.12) into Eqs. (6.9b,c), the reduced-order gyroscopic and stiffness matrices can be expressed as

$$\bar{G}(t) = \dot{\theta}(t)\bar{G}_1 \tag{6.14a}$$

$$\bar{K}(t) = \ddot{\theta}(t)\bar{K}_1 + \dot{\theta}^2(t)\bar{K}_4 + f_2(\theta)\bar{K}_g \tag{6.14a}$$

where the constant coefficient matrices are defined as

$$\bar{G}_1 = X^T G_1 X, \quad \bar{K}_1 = X^T K_1 X, \quad \bar{K}_4 = X^T K_4 X, \quad \bar{K}_g = X^T K_g X \tag{6.14c-f}$$

Introducing Eq. (6.13) into Eq. (6.8), the reduced-order generalized force vector can be expressed as

$$\underset{\sim}{f}(t) = \ddot{\theta}(t)\underset{\sim}{f}_1 + \dot{\theta}^2(t)\underset{\sim}{f}_2 + h(\theta)\underset{\sim}{f}_g \tag{6.15a}$$

where

$$\underset{\sim}{f}_1 = X^T \underset{\sim}{F}_1^* \ , \quad \underset{\sim}{f}_2 = X^T \underset{\sim}{F}_2^* \ , \quad \underset{\sim}{f}_g = X^T \underset{\sim}{F}_g \tag{6.15b-d}$$

Examining the expressions for the stiffness matrices, Eqs. (3.16e-g, 3.17d-f), the most significant terms of $f_1 K_{10}$ of Eq. (6.11b) can be expressed as

$$f_1 K_{10} = \begin{bmatrix} 0 & 0 & 0 \\ 0 & \underset{\sim}{\tilde{S}}\underset{\sim}{H} & \underset{\sim}{\tilde{H}}\bar{\Phi} \\ 0 & \bar{\Phi}^T \underset{\sim}{\tilde{H}}^T & K_{Ag} \end{bmatrix} \tag{6.16a}$$

where

$$\underset{\sim}{H} = C_0 \underset{\sim}{g} \tag{6.16b}$$

and K_{Ag} is the portion of the bending stiffness matrix of the appendage due to gravitational effects. The rotational transformation matrix C_0 can be expanded as

$$C_0 = C_0'' C_0' \tag{6.17}$$

where C_0' is the matrix describing the initial orientation of the 0 frame with respect to the inertial frame and C_0'' describes the orientation of the 0 frame with respect to the initial orientation during the maneuver. Hence, Eq. (6.16b) can be expressed as

$$\underset{\sim}{H} = C_0'' \underset{\sim}{g}' \tag{6.18}$$

where

$$\underset{\sim}{g}' = C_0' \underset{\sim}{g} \tag{6.18a}$$

For the maneuvers of interest, C_0'' is a function of the maneuver history described by $\theta(t)$, or

$$C_0'' = \begin{bmatrix} 1 & 0 & 0 \\ 0 & \cos\theta & \sin\theta \\ 0 & -\sin\theta & \cos\theta \end{bmatrix} \tag{6.19}$$

Thus, Eq. (6.18) can be expressed as

$$\underset{\sim}{H} = \underset{\sim}{H}_0 + \cos\theta \underset{\sim}{H}_c + \sin\theta \underset{\sim}{H}_s \tag{6.20a}$$

where

$$\underset{\sim}{H}_0^T = [g_1' \quad 0 \quad 0] \tag{6.20b}$$

$$\underset{\sim}{H}_c^T = [0 \quad g_2' \quad g_3'] \tag{6.20c}$$

$$\underset{\sim}{H}_s^T = [0 \quad g_3' \quad -g_2'] \tag{6.20d}$$

and

$$\underset{\sim}{g}'^T = [g_1' \quad g_2' \quad g_3'] \tag{6.20e}$$

The matrix K_{Ag} also depends on $\theta(t)$ and can be expressed as

$$K_{Ag} = K_{Ag0} + \cos\theta K_{Agc} + \sin\theta K_{Ags} \tag{6.21}$$

Introducing Eqs. (6.20) and (6.21) into Eqs. (6.16) and this result into Eq. (6.14f), the reduced-order gravitational terms of the stiffness matrix can be expressed as

$$\bar{K}_g = \bar{K}_{g0} + c\theta\bar{K}_{gc} + s\theta\bar{K}_{gs} \tag{6.22}$$

where $\bar{K}_{g0}$, $\bar{K}_{gc}$ and $\bar{K}_{gs}$ are matrices of time-invariant terms. Introducing Eq. (6.20) into Eq. (3.16b, 3.17b), the gravitational terms of the reduced-order force vector of Eq. (6.15a) can be expressed as

$$\underset{\sim}{f}_g = \underset{\sim}{f}_{g0} + \cos\theta\underset{\sim}{f}_{gc} + \sin\theta\underset{\sim}{f}_{gs} \tag{6.23}$$

where

$$\underset{\sim}{f}_{g0} = -X^T\bar{\Phi}^T\underset{\sim}{H}_0 \quad , \quad \underset{\sim}{f}_{gc} = -X^T\bar{\Phi}^T\underset{\sim}{H}_c \quad , \quad \underset{\sim}{f}_{gs} = -X^T\bar{\Phi}^T\underset{\sim}{H}_s \tag{6.23a-c}$$

Gravity exerts a significant influence on the laboratory model of SCOLE. Hence, including the gravitational effects in the premaneuver eigenvalue problem can be beneficial in some circumstances. In this case, θ is set equal to zero in Eq. (6.16a) and the resulting matrix is added to K_0 of Eq. (6.3) and subtracted from Eq. (6.16a). Note that the stiffness matrix of Eq. (6.16a) is nonsymmetric due to the term $\underset{\sim\sim}{SH}$. Thus, the premaneuver eigenvalue problem appears to be nonself-adjoint when gravity is included. However, for stability the universal joint must be above the true center of mass of the structure. Equation (6.1) can be solved for the static deformation of the structure from which the actual center of mass can be determined. This static correction to the matrix $\underset{\sim}{S}$ nullifies the quantity $\underset{\sim\sim}{SH}$ and the stiffness matrix becomes

symmetric. The premaneuver eigenvalue problem is then self-adjoint as it should be for a stable equilibrium position.

The spatial integrations and multiplications necessary to evaluate Eqs. (6.14c-f) and (6.15b-d) can be done off-line, before the start of the simulation. Evaluation of the matrix $A(t)$ of Eq. (6.10c) during the simulation merely requires the simple multiplications found in Eqs. (6.14a,b). The computer storage and multiplications implied by Eqs. (6.14a,b) at each time step can be further reduced by storing and multiplying only the nonzero elements of the matrices $\bar{G}_1$, $\bar{K}_1$, $\bar{K}_4$ and $\bar{K}_g$, since these matrices may be sparse. Hence, the computations required at each time step to perform the simulation have been greatly reduced.

CHAPTER VII

ACTIVE VIBRATION CONTROL

7.1 INTRODUCTION

The generalized forces discussed thus far, have been disturbance forces and maneuver control forces. The disturbance forces are caused by the acceleration and velocity of the body-fixed frame during the maneuver and the acceleration of gravity. This chapter deals with the computation and application of control forces suppressing the vibrations of the structure, that is, the undesirable elastic motions and deviations from the desired rigid-body maneuver trajectory. The implementation techniques discussed in Sec. 7.6 also apply to the maneuver control developed in Chapter 5.

The first section deals with the problem of shape and orientation control of the spacecraft. Steady-state disturbance forces require the mean control forces to be nonzero if the shape of the structure is to be maintained in a configuration other than that of uncontrolled equilibrium. Gravity is a distributed force and must be opposed by a distributed force if precise shape control is to be achieved. In a general rotational maneuver, the gravity force varies with time when measured relative to the O frame, so that the opposing shape control forces must also vary with time.

Optimal control techniques with linear feedback are discussed along with pole-placement methods. The merits of a minimum-time performance functional versus a minimum energy/effort performance functional are considered in terms of vibration suppression. Inclusion of the

actuator's dynamics along with the structure's dynamics for control force computation is found to be beneficial. In fact, all the control techniques presented are reformulated to include actuator dynamics.

In Chapter 6 the premaneuver eigenvectors were used as admissible vectors for the simulation problem. In this chapter, these same vectors are used as admissible vectors for vibration suppression. At each sampling time, the control forces are formulated as if the premaneuver eigenfunctions are the true eigenfunctions at that time. This is equivalent to a modeling error and does not cause a stability problem for robust control techniques, such as natural control, which do not require the exact eigenfunctions in control evaluation (Refs. 12-17). As has been shown in Chapter 3, the equations describing the motion of a spacecraft during a maneuver are nonself-adjoint. Thus, a control technique designed for self-adjoint systems is applied to a nonself-adjoint system of equations.

7.2 SHAPE CONTROL

One part of the SCOLE design challenge requires rotating the structure through a specified angle and then aiming the antenna within a certain tolerance, all in minimum time. Hence, for SCOLE, the control task of highest priority is aiming the antenna and maintaining its shape. The shape of the mast is not critical provided its deformation is within reasonable limits. Shape control implies opposing a steady-state, or slowly varying force to maintain approximately a certain mean configuration. On the other hand, vibration control suppresses small motions of the structure about the desired steady-state configuration.

Hence, shape control adds apparent gross stiffness to the structure, while vibraton control applies apparent damping. The shape control can orient and position the O frame as well as elastically shape the structure.

If the axis of rotation does not correspond to the gravitational axis, the static-elastic deflection, which would result if the O frame were held fixed at its present position, varies with time during the maneuver. Hence, for aiming the antenna, the static-elastic deflection due to gravity must be taken into consideration. One possibility is to attempt to suppress the static-elastic deflection with active controls, that is, keep the structure undeformed. This is total structural shape control and may be necessary if the antenna is to be oriented accurately and uniformly with respect to the shuttle. An alternative is to attempt to control the shape and orientation of the antenna only, allowing the mast to deform.

Shape control requires a control force equal and opposite to the mean disturbance forces. Gravity is a distributed force and must be opposed by a distributed force, or at least by a great number of discrete actuators. For a spacecraft in orbit, the gravitational force is mainly opposed by a centrifugal force, which is distributed, and only higher-order forces such as the gravity gradient, aerodynamic drag and solar wind must be combated with shape control forces. However, for the laboratory model, only the tether's tension, which is a point force, opposes gravity. Hence, shape control requires more control effort for the laboratory model than for the orbiting spacecraft. In fact, typical

vibration control techniques such as natural control include feedback on the displacement and so, may be capable of higher-order shape control required for the orbiting spacecraft.

Gravity provides a steady-state disturbance force which depends only on the mass distribution of the structure. The mass distribution is generally known with more accuracy than the stiffness distribution. Hence, shape control can be open-loop in some circumstances such as in the laboratory. However, for an orbiting spacecraft, the steady-state forces are less well defined, though smaller in magnitude, and require closed-loop shape control.

Due to the large amount of effort and great number of actuators needed, precise shape control may be impractical for the laboratory experiment. An alternative is to implement only vibration control, that is, allow the structure to deform to its static-elastic deformation but suppress the vibrations about this configuration. Vibration control of this type can be formulated by including the gravitational potential along with the elastic potential energy in the performance functional discussed in Sec. 7.4.

7.3 ACTUATOR DYNAMICS

The premaneuver modal equations of motion were discussed in the last chapter. The equation of motion for the rth mode can be expressed as

$$\ddot{u}_r(t) + \omega_r^2 u_r(t) = f_{dr}(t) + f_r(t) \tag{7.1}$$

where $f_{dr}(t)$ is the sum of the rth modal disturbance and maneuver control forces and $f_r(t)$ is the rth modal vibrational control force

defined as the rth component of the vector

$$\underset{\sim}{f}(t) = X^T \underset{\sim}{F}(t) \tag{7.2}$$

where $\underset{\sim}{F}(t)$ is a vector of control forces and moments. The response of the actuators to their commands is assumed to be of first-order as in Chapter 5 so that an actuator's equation of motion can be expressed as

$$\dot{F}(t) = aF(t) + bF_c(t) \tag{7.3}$$

where a and b are constants and $F_c(t)$ is the command force. Multiplying Eq. (7.3) by X^T and assuming that all the actuators obey the same equations of motion, the rth modal control force's equation of motion can be expressed as

$$\dot{f}_r(t) = af_r(t) + bf_{cr}(t) \tag{7.4a}$$

where f_{cr} is the rth component of the vector

$$\underset{\sim}{f}_c = X^T \underset{\sim}{F}_c \tag{7.4b}$$

In discrete time, if the feedback force f_r is computed at t_i, the earliest it can be applied is the next sampling time t_{i+1}. However, considering Eq. (7.4a) in discrete time, f_{cr} is the quantity that is updated at t_{i+1} and the desired force f_r cannot actually be applied until t_{i+2}. Hence, the actuator response doubles the time lag for control force application. This problem can be circumvented by including the actuator's response, Eq. (7.3), in the control formulation.

Since the force $f_{dr}(t)$, does not affect the vibration control formulation, it will be neglected in the following discussion. Taking the time derivative of Eq. (7.1) and neglecting $f_{dr}(t)$ results in the expression:

$$\ddot{u}_r + \omega_r^2 \dot{u}_r = \dot{f}_r \tag{7.5}$$

Introducing Eq. (7.4) and (7.1) into Eq. (7.5), the combined dynamic equation can be expressed as

$$\dddot{u}_r = -\omega_r^2 \dot{u}_r + a\ddot{u}_r + a\omega_r^2 u_r + bf_{cr} \tag{7.6}$$

The state equations for the rth mode can be expressed in the state form

$$\dot{z}_r = A_r z_r + b f_{cr} \tag{7.7a}$$

where

$$z_r^T = [u_r \quad \dot{u}_r \quad \ddot{u}_r] \tag{7.7b}$$

$$A_r = \begin{bmatrix} 0 & 1 & 0 \\ 0 & 0 & 1 \\ a\omega_r^2 & -\omega_r^2 & a \end{bmatrix} \tag{7.7c}$$

$$b^T = [0 \quad 0 \quad b] \tag{7.7d}$$

7.4 OPTIMAL CONTROL

The minimum-time optimal control policy is bang-bang and involves determining three-dimensional switching surfaces for each mode. At each sampling time the modal state is to be located with respect to the switching surfaces, and based on this, the command modal force is set to its positive or negative maximum value. The calculation of three-dimensional switching surfaces is not a simple matter and using them in the above mentioned fashion can be computationally time consuming (Ref. 10). If the measured modal states are noisy, the modal forces could be switched frequently. This implies frequent, abrupt structural accelerations which when applied with spatially discrete forces tend to destablize the uncontrolled modes. Hence, a minimum-time optimal performance functional for vibration control has distinct disadvantages.

Consider instead, the IMSC optimal performance functional which minimizes a weighted sum of the elastic energy and the control effort (Refs. 16, 20). This performance index has the form

$$J = \sum_{r=1}^{\infty} J_r \tag{7.8a}$$

where

$$J_r = \int_0^{\infty} (\underset{\sim}{z}_r^T Q_r \underset{\sim}{z}_r + R_r f_{cr}^2)dt \tag{7.8b}$$

are the modal performance functionals and

$$Q_r = \begin{bmatrix} q_r & 0 & 0 \\ 0 & 1 & 0 \\ 0 & 0 & 0 \end{bmatrix} \tag{7.8c}$$

in which q_r and R_r are weighting factors. For the elastic modes, q_r is taken as the rth eigenvalue ω_r^2, and for the rigid-body modes q_r is chosen on the basis of pole-placement considerations. As the effort's weight R_r is decreased, the rate of modal energy dissipation is increased, but, of course, more effort is required. Hence, R_r can be chosen on the basis of the available control command force for vibration suppression. The command forces required by this performance functional tend to be smooth functions compared to the discontinuous, bang-bang forces of minimum-time control. Smooth forcing time histories are preferable in that they do not tend to excite the uncontrolled modes to the extent of forces that contain discontinuities.

In order to minimize J of Eq. (7.8a), each J_r of Eq. (7.8b) can be minimized independently. The steady-state Riccati equation for the rth

mode is a set of algebraic equations of order three and can be expressed as

$$0 = -K_r A_r - A_r^T K_r - Q_r + \frac{1}{R_r} K_r \underset{\sim}{b}\underset{\sim}{b}^T K_r \tag{7.9}$$

where K_r is a symmetric matrix to be determined which takes the form

$$K_r = \begin{bmatrix} k_{r1} & & \text{symm.} \\ k_{r2} & k_{r4} & \\ k_{r3} & k_{r5} & k_{r6} \end{bmatrix} \tag{7.10}$$

The linear, state feedback control law is of the form

$$f_{cr} = -\frac{1}{R_r} \underset{\sim}{b}^T K_r \underset{\sim}{z}_r \tag{7.11}$$

Introducing Eq. (7.7b) into Eq. (7.11), the control law becomes

$$f_{cr} = -\frac{b}{R_r} (k_{r3} u_r + k_{r5} \dot{u}_r + k_{r6} \ddot{u}_r) \tag{7.12}$$

which minimizes the performance functional given by Eq. (7.8b) (Ref. 10). In the solution of Eq. (7.9) the required terms of K_r can be determined from the following expressions:

$$k_{r3} = \frac{R_r}{b^2} (a\omega_r + d_r) \tag{7.13a}$$

$$k_{r6}^4 C_4 + k_{r6}^3 C_3 + k_{r6}^2 C_2 + k_{r6} C_1 + C_0 = 0 \tag{7.13b}$$

$$k_{r5} = -a k_{r6} + \frac{b^2}{2R_r} k_{r6}^2 \tag{7.13c}$$

where

$$d_r = [a^2\omega_r^2 + q_r b^2/R_r]^{1/2}, \quad C_0 = \frac{1}{d_r} (a k_{r3} - \frac{1}{2}),$$

$$C_1 = -\frac{1}{d_r} (d_r + a\omega_r^2), \quad C_2 = \frac{b^2}{2 d_r R_r} (\omega_r^2 + a^2), \tag{7.13d-i}$$

$$C_3 = \frac{-b^4 a}{2d_r R_r^2}, \quad C_4 = \frac{b^6}{8d_r R_r^3}$$

are constant coefficients which can be evaluated for each mode. The solution of the fourth-order polynomial of Eq. (7.13b) for k_{r6} can be obtained numerically for each mode before the start of the control procedure. This solution can then be introduced into Eq. (7.13c) to obtain k_{r5} for each mode, thus completing the solution for the control gains. The control law given by Eq. (7.12) is IMSC modified to include actuator dynamics. IMSC is also called natural control because the closed-loop modes are identical to the open-loop or natural modes, so that natural coordinates remain natural after control (Ref. 20). Note that the performance functional and eigenvalue problem must be complimentary. Hence, if the eigenvalue problem includes the gravitational potential energy, this effect must also be included in the performance index J. Natural control is efficient because no effort is wasted in changing the shape of the modes (Ref. 18). In this regard, we recall that only eigenvalues affect stability and not eigenvectors.

Equation (7.12) can be expressed in the form

$$f_{cr} = -g_{r1}u_r - g_{r2}\dot{u}_r - g_{r3}\ddot{u}_r \tag{7.14}$$

where the control gains are defined as follows:

$$g_{r1} = \frac{bk_{r3}}{R_r}, \quad g_{r2} = \frac{bk_{r5}}{R_r}, \quad g_{r3} = \frac{bk_{r6}}{R_r} \tag{7.14b-d}$$

Introducing Eqs. (7.14) into Eqs. (7.7) and solving the characteristic determinant, the closed-loop poles are the roots of the polynomial

$$s^3 + (g_{r3} - a)s^2 + (g_{r2} + \omega_r^2)s + (g_{r1} - a\omega_r^2) = 0 \tag{7.15}$$

Equation (7.15) can be used to determine the required values of the control gains g_{ri} (i = 1,2,3) so as to produce the desired pole placement for the rigid-body modes.

7.5 POLE ALLOCATION

In optimal control, a performance functional is defined, somewhat arbitrarily, and minimized. In pole allocation methods of modal control, the poles are chosen, again somewhat arbitrarily, for each mode and the actuator forces are computed to produce these desired results. The most general form of the poles for the rth mode defined by Eqs. (7.7) whose characteristic equation is represented by Eq. (7.15) can be expressed as

$$s_{r1} = \alpha_r + i\beta_r, \quad s_{r2} = \alpha_r - i\beta_r, \quad s_{r3} = \gamma_r \qquad (7.16a\text{-}c)$$

where α_r and γ_r are decay-rate time constants for the rth mode and β_r is the closed-loop modal frequency. The characteristic equation associated with the poles given by Eqs. (7.16) is of the form

$$s^3 + (-\gamma_r - 2\alpha_r)s^2 + (2\gamma_r\alpha_r + \alpha_r^2 + \beta_r^2)s + (-\gamma_r\alpha_r^2 - \gamma_r\beta_r^2) = 0 \qquad (7.17)$$

Equating Eqs. (7.17) and (7.15) and solving for the control gains, we obtain

$$g_{r1} = a\omega_r^2 - \gamma_r(\alpha_r^2 + \beta_r^2) \qquad (7.18a)$$

$$g_{r2} = 2\gamma_r\alpha_r + \alpha_r^2 + \beta_r^2 - \omega_r^2 \qquad (7.18b)$$

$$g_{r3} = a - 2\alpha_r - \gamma_r \qquad (7.18c)$$

Hence, the poles given by Eqs. (7.16) can be chosen for each mode and implemented with the command modal force given by Eq. (7.14) and the gains of Eqs. (7.18).

7.6 IMPLEMENTATION OF MODAL CONTROL

Modal Actuation

Implementation of any IMSC technique requires an inversion of Eq. (7.4a), so that the applied command force $\underset{\sim}{F}_c$ can be found from knowledge of the modal command force $\underset{\sim}{f}_c$. Present technology does not permit distributed actuation, so that we must be content with suboptimal discrete actuation. For the case of discrete actuators, the simplest implementation technique is a projection method (Ref. 16). Premultiplying Eq. (6.5a) by the pseudo-inverse of X^T denoted by X^{-T}, we obtain

$$X^{-T} = MX \tag{7.19}$$

Premultiplying Eq. (7.4b) by X^{-T} and considering Eq. (7.19) we obtain

$$\underset{\sim}{F}_c = MX\underset{\sim}{f}_c \tag{7.20}$$

which is the discrete counterpart of a distributed generalized force and must be applied with actuators at every finite element node. This may require an impractically large number of actuators, so that only an approximate "distributed" force can be applied. The simplest approximation is a projection symbolized mathematically by a quasi-identity matrix operator I_p, where all the elements are zero except the diagonal elements corresponding to the available actuators, which are unity. As such, the projected force vector $\underset{\sim}{F}_{cp}$ is related to the "distributed" force vector $\underset{\sim}{F}_c$ as follows:

$$\underset{\sim}{F}_{cp} = I_p\underset{\sim}{F}_c \tag{7.21}$$

This technique, while being suboptimal, is desirable because it avoids the computation of a numerical inverse and requires no additional

computations if an actuator fails.

Another method of calculating the applied command force $\underset{\sim}{F}_C$ requires a numerical inversion (Ref. 14). Given m actuators and their locations, $\underset{\sim}{F}_C$ can be partitioned into the form

$$\underset{\sim}{F}_C^T = [\underset{\sim}{F}_{CC}^T \quad \underset{\sim}{0}^T] \tag{7.22}$$

where $\underset{\sim}{F}_{CC}$ is an $m \times 1$ vector of control forces corresponding to the available actuators. The columns of X^T can be rearranged accordingly, so that Eq. (7.4b) can be expressed as

$$\underset{\sim}{f}_C = [B_C \quad B_r] \begin{bmatrix} \underset{\sim}{F}_{CC} \\ \underset{\sim}{0} \end{bmatrix} \tag{7.23}$$

where B_C is a $c \times m$ matrix, c is the number of controlled modes and B_r corresponds to the uncontrolled or residual modes. Hence, an equation of the form

$$\underset{\sim}{f}_C = B_C \underset{\sim}{F}_{CC} \tag{7.24}$$

relates the actuator forces to the modal control forces. If $m = c$, then B_C can be inverted, so that premultiplying Eq. (7.24) by this B_C^{-1}, we obtain the expression

$$\underset{\sim}{F}_{CC} = B_C^{-1} \underset{\sim}{f}_C \tag{7.25}$$

which is the desired relation.

Inverse control requires a numerical inversion, unlike projected control, but has the advantage of producing the desired c components of the modal force vector exactly, rather than only an approximation as in the case of projected control. Thus, inverse control is a true natural control in that the closed-loop eigenfunctions of the controlled modes

are identical to the open-loop eigenfunctions. Note that the inversion must be recalculated in the event of an actuator failure. If $m < c$, B_c^{-1} represents a pseudo-inverse and the modal forces are applied in a least-squares sense rather than exactly. The forces computed from both the inverse and projected methods tend to excite the uncontrolled modes giving rise to so-called control spillover (Ref. 14, 16).

Modal Estimation

Modal state estimation is another common problem inherent in the implementation of modal control techniques. This problem is somewhat analogous to that of modal force implementation. For estimation the equation that must be inverted is Eq. (6.6). The projection technique requires premultiplying this equation by the matrix product $X^T M$ and introducing Eq. (6.5a) which yields

$$\underset{\sim}{u}(t) = X^T M \underset{\sim}{x}(t) \tag{7.26}$$

which is the second half of the expansion theorem (Ref. 13). Equation (7.26) and its time derivatives form what are known as modal filters (Ref. 19). Application of modal filters presupposes "distributed" sensors, or sensors at every node for a finite element model. Since this is not usually the case, a projection technique could be attempted, similar to that used above, where $\underset{\sim}{x}$ is nullified except at the sensor locations where it retains its measured values. However, this is not recommended unless many sensors are available, since it is equivalent to approximating the structure's naturally smooth displacement function with spatial Dirac delta functions, which is physically unrealistic. On

the other hand, force projection is acceptable since force application with discrete actuators is indeed mathematically equivalent to spatial Dirac delta functions. For modal state estimation, an acceptable approach is to interpolate the discrete sensor's measurements with admissible functions to obtain approximate but smooth displacement, velocity and acceleration functions. These functions are then introduced into the modal filter equations to yield the approximate modal states.

The most straightforward method of modal estimation involves a numerical inversion of a matrix. In a manner analogous to the inversion technique for force implementation, the displacement vector and modal matrix of Eq. (6.5a) can be partitioned as follows:

$$\begin{bmatrix} \underset{\sim}{x}_s \\ --- \\ \underset{\sim}{x}_{ns} \end{bmatrix} = \begin{bmatrix} B_s \\ --- \\ B_{ns} \end{bmatrix} \underset{\sim}{u} \tag{7.27}$$

where $\underset{\sim}{x}_s$ is an $s \times 1$ vector of measured displacements with $\underset{\sim}{x}_{ns}$ as the remainder and B_s is an $s \times c$ matrix which originated from the modal matrix X with B_{ns} as the remaining portion. Hence, the equation

$$\underset{\sim}{x}_s = B_s \underset{\sim}{u} \tag{7.28}$$

relates the modal displacements with the measured displacements. Premultiplying Eq. (7.28) by B_s^{-1} results in the expression

$$\underset{\sim}{u} = B_s^{-1} \underset{\sim}{x}_s \tag{7.29}$$

where B_s^{-1} is a pseudo-inverse if $s \neq c$.

The observation spillover is computed from Eq. (7.27), after Eq. (7.29) has been introduced, as

$$\underset{\sim}{x}_{ns} = B_{ns}B_s^{-1}\underset{\sim}{x}_s \tag{7.30}$$

Thus, the inverse technique of modal estimation also implies assignment of values to the unmeasured states, and can be thought of as affecting a type of interpolation.

7.7 OUTPUT FEEDBACK CONTROL

Modal control techniques have become quite common in the field of control of structures because of their ability to take advantage of the physical and mathematical properties of the natural modes of vibration. The main drawbacks common to all modal control methods are the problems encountered in modal force implementation and modal state estimation with discrete actuators and sensors. Direct output feedback methods, where the command control force is related directly to the measured state through control gains, avoids modal estimation entirely. In addition, if this feedback force is the physical (rather than modal) force, then the modal force implementation is also avoided. Hence, the most useful control technique would be derived while taking advantage of the concepts of natural modes but be applicable with output feedback. The relationship between linear, output feedback control and linear, modal feedback control will now be explored.

Consider the equation expressing a linear control law with output feedback and constant gains, or

$$\underset{\sim}{F}_c(t) = -A[\underset{\sim}{x}(t)g_1 + \dot{\underset{\sim}{x}}(t)g_2 + \ddot{\underset{\sim}{x}}(t)g_3] \tag{7.31}$$

where g_1, g_2 and g_3 are control gains, $\underset{\sim}{F}_c$ is a vector of physical command forces to be applied, $\underset{\sim}{x}$, $\dot{\underset{\sim}{x}}$ and $\ddot{\underset{\sim}{x}}$ are vectors expressing the

measured state and A is a weighting matrix of constant coefficients. Introducing Eq. (6.5a) and its time derivatives into Eq. (7.31), we obtain

$$\underset{\sim}{F}_c(t) = -AX[\underset{\sim}{u}(t)g_1 + \dot{\underset{\sim}{u}}(t)g_2 + \ddot{\underset{\sim}{u}}(t)g_3] \tag{7.32}$$

from which it appears that, considering Eq. (7.14) the associated modal control force can be expressed as

$$\underset{\sim}{f}_c(t) = -\underset{\sim}{u}(t)g_1 - \dot{\underset{\sim}{u}}(t)g_2 - \ddot{\underset{\sim}{u}}(t)g_3 \tag{7.33}$$

where the modal control gains are constant for all modes. Hence, Eq. (7.32) takes the form

$$\underset{\sim}{F}_c = AX\underset{\sim}{f}_c \tag{7.34}$$

Considering Eq. (7.20), which is true regardless of the control technique because it is only an extension of the expansion theorem, it is obvious that the weighting matrix A should be equal to the mass matrix. Hence, if A is replaced by M in Eq. (7.31), the output feedback control law takes the form

$$F_c(t) = -M[\underset{\sim}{x}(t)g_1 + \dot{\underset{\sim}{x}}(t)g_2 + \ddot{\underset{\sim}{x}}g_3] \tag{7.35}$$

and the effective control thus produced is equivalent to the modal control of Eq. (7.33). However, the control gains have yet to be determined. Note that in Chapter 5 the mass matrix was also found to act as the weight, or gain, for the maneuver control force Eqs. (5.13, 5.14).

A method of determining a particular set of these control gains which has both a good physical and mathematical basis is known as uniform damping control (Ref. 24). This method is a pole allocation technique and, hence, must be implemented with distributed actuators if

the poles are to be placed exactly as desired. However, in structural vibration controls, precise pole placement is rarely necessary. Indeed, uniform damping control can readily be applied with discrete actuators in an approximate, but robust manner.

Consider Eqs. (7.16) which represent the desired closed-loop poles for pole allocation. Changing the natural frequencies of the modes with control effort could be considered a waste of effort for the case of vibration suppression. Therefore, β_r of Eqs. (7.16) is taken as being equal to the natural frequency of the rth mode ω_r. The expansion theorem states that the motion of the structure can be represented as a linear combination of all the modes. Hence, it is reasonable to force all the modes to decay in time at the same rate, which implies that $\alpha_r = \alpha$ and $\gamma_r = \gamma$ in Eqs. (7.16). Introducing these values into Eqs. (7.18), the gains for the rth mode can be expressed as

$$g_{r1} = (a - \gamma)\omega_r^2 - \gamma\alpha^2, \quad g_{r2} = 2\gamma\alpha + \alpha^2, \quad g_{r3} = a - 2\alpha - \gamma \tag{7.36a-c}$$

which are identical for all the modes. If γ is set equal to the decay rate of the actuator response a, which also is an open-loop pole, then the modal gains for all the modes become

$$g_1 = -a\alpha^2, \quad g_2 = 2a\alpha + \alpha^2, \quad g_3 = -2\alpha \tag{7.37a-c}$$

When these gains are introduced into Eq. (7.35), the result is a linear output feedback control law providing a uniform decay rate for all the modes without altering the natural frequencies. Thus, modal estimation and implementation is bypassed entirely, although the formulation takes advantage of the concepts of modal control. In fact, uniform damping

control can also be derived as a first-order approximation of natural control if

$$R = \frac{1}{2a^2\alpha^2} \qquad (7.38)$$

and $\alpha << \omega_r$ for all modes.

As with other distributed control techniques, uniform damping control can only be implemented approximately with discrete actuators. However, this control method has the advantage of being applicable in a decentralized and collocated sense, and one that is known to be robust (Refs. 1, 24). If an actuator and sensor pair is located at node i, acting in direction 1, the control command force at that location takes the form

$$F_{ci\ell} = -m_{i\ell}(x_{i\ell}g_1 + \dot{x}_{i\ell}g_2 + \ddot{x}_{i\ell}g_3) \qquad (7.39)$$

where $m_{i\ell}$ is an entry of the mass matrix, and $x_{i\ell}$, $\dot{x}_{i\ell}$ and $\ddot{x}_{i\ell}$ are correspondents of the displacement, velocity and acceleration vectors, respectively, all of which correspond to node i and direction 1. This is known as decentralized control because the force at a point is related only to measurements taken at that point and, of course, is only possible when the actuators and sensors are collocated. If collocation is not possible, the measured state must be spatially interpolated to approximate the state at the actuator locations. Another advantage of uniform damping control is that all the modes are controlled, even with discrete actuation, not just a subset as with typical modal control techniques. A disadvantage of this control technique is that it is no longer a first-order approximation of natural control and, thus, not

optimal if the desired decay rate α is large compared to ω_r (which is frequently the case).

The mass matrix has been found to be the weighting matrix both for the open-loop maneuver force Eq. (5.13) and for a particular closed-loop vibration control force Eq. (7.35). There is a certain physical sense in this result. Obviously, the uniform acceleration of a spacecraft demands more force at more massive sections. For the maneuver, this acceleration rate is the desired rotational acceleration and for the vibration control, it is the required vibrational decay rate α.

CHAPTER VIII

NUMERICAL RESULTS

8.1 MATHEMATICAL MODEL

The SCOLE configuration of Fig. 8.1 is modeled by means of the finite element method. This model is used to demonstrate the maneuver strategy of Chapter 5, the simulation of Chapter 6 and the control techniques of Chapter 7.

The mast supporting the antenna is a steel tube 10 feet in length. The antenna consists of 12 aluminum tubes, each 2 feet long, welded together to form a grid in a hexagonal shape. The tether is an 11 feet long steel cable. The material properties can be found in Table 8.1. There is a lumped mass of 0.01719 slugs at the point of the attachment of the antenna to the mast. Also, the hub of the antenna is considered to be a lumped mass of 0.004201 slugs. Figure 8.1 shows the nodal locations of the finite element model. Hermite cubics were used as interpolation functions for bending and linear functions for axial and torsional deformations.

The "shuttle" is a steel plate of uniform thickness with a mass of 13.85 slugs and mass moment of inertia matrix as follows:

$$I_{SO} = \begin{bmatrix} 10.914 & 0 & 0 \\ 0 & 39.754 & 0 \\ 0 & 0 & 50.668 \end{bmatrix} \text{ slugs-ft}^2 \qquad (8.1)$$

The O frame is embedded in the shuttle with the origin at its center of mass as shown in Fig. 8.1. The center of mass is located 2.6708 feet

from the rear of the shuttle in the x direction. Table 8.2 lists the values of the lumped masses attached to the plate and their respective locations. Table 8.3 identifies the location of the mast's attachment to the shuttle as well as the universal joint's location, both with respect to the 0 frame. Note that the mast is attached below the rigid-body center of mass and the joint is located above the true center of mass. This joint location provides a horizontal static equilibrium orientation for the shuttle which is the actual orientation for SCOLE. The total mass of the structure is 23.884 slugs and the mass moment of inertia matrix about the universal joint (point B) is

$$I_B = \begin{bmatrix} 65.9409 & & \text{Symm} \\ -.006082 & 89.0227 & \\ 7.4305 & 2.1118 & 87.5150 \end{bmatrix} \text{ slugs-ft}^2$$

8.2 PREMANEUVER EIGENSOLUTION

An eigensolution was performed on the laboratory model of Fig. 8.1 with the structure in its static equilibrium state. The static deflection is plotted in Fig. 8.2. The natural frequencies are listed in the first column of Table 8.4 and the first fifteen modes are plotted in Figs. 8.3 through 8.17. The quantity FACT given in the plots is the scale factor used to amplify the deformations for plotting purposes. The universal joint is denoted by a star and the underformed structure by dashed lines. The view is from above and slightly behind the shuttle.

The appendage is rigid in the first five modes. The first mode is a yaw rigid-body mode (rotation about the z_0 axis). The second and

third modes are combinations of pitch and roll, the former being mostly pitch (about the y_0 axis). Modes 4 and 5 are pendulum modes consisting of rigid-body translations of the structure in the x_0 and y_0 directions. Modes 6 and 7 are the first bending modes of the appendage and exhibit deformations mainly in the x_0z_0 and y_0z_0 planes, respectively. Mode 8 is characterized by both bending and torsion of the mast. Modes 9 and 10 exhibit higher degrees of bending of the mast and perceptible deformations of the antenna while mode 11 demonstrates an even more notable deformation of the antenna. Modes 12 and 13 are bending modes of the cable with the structure appearing to be unaffected. Modes 14 and 15 also exhibit notable deformations of the antenna. Mode 15 includes axial motion of the cable which obviously affects the deflections of the mast and antenna.

The plots of modes 16 and 17 are not presented, but they are bending modes of the cable, like modes 12 and 13, with no perceptible effects on the structure. Hence, higher-order bending vibration of the cable has little effect on the spacecraft because the universal joint does not permit moment transmission from the cable to the spacecraft. As the mass of the cable is decreased, the frequencies of higher-order bending modes of the cable approach infinity. The second column of Table 8.4 contains the frequencies of the structure with the mass of the cable neglected. As expected, this aproximation affects the remaining frequencies only slightly. The mass of the cable will be neglected in the sequel. Note that this approximation yields a time invariant mass matrix for the laboratory model.

Gravity has a great influence on the laboratory model. The natural frequencies of the spacecraft in a space environment, with no tether or gravitational effects, are listed in column three of Table 8.4. Note that there are now six zero frequencies corresponding to the rigid-body modes. All of the frequencies are lower than the corresponding frequencies with gravity included because gravity has a stiffening effect. In fact, to further demonstrate the effect of gravity, the natural frequencies of the appendage cantilevered at the base are listed in Table 8.5. The first and second columns of Table 8.5 correspond to the cantilevered end of the mast lying above and below the mast, respectively. The direction of gravity with respect to the appendage has the greatest effect on the first two frequencies. The first two bending frequencies of the appendage are plotted versus the roll angle in Fig. 8.18 for the spacecraft in the laboratory. Zero degrees corresponds to the static equilibrium position of the structure. Hence, gravity strongly influences the stiffness of the appendage.

The last column of Table 8.4 demonstrates the error resulting from considering the antenna as rigid. Comparing this column with the column before last, we conclude that only the first two elastic modes of the appendage are relatively unaffected by this approximation.

8.3 STABILITY

For safety, a large degree of stability is important for the laboratory experiment. On the other hand, greater stability results in increased control effort to combat gravity during a maneuver. Hence, a stability analysis is essential.

The stable region during a roll maneuver is defined as the range of the roll angle while the static stiffness matrix remains semipositive definite. A semipositive stiffness matrix is equivalent to nonnegative eigenvalues since the mass matrix is positive definite. The location of the ball joint with respect to the center of mass is the critical parameter for stability. Of course, as the structure changes position with respect to the direction of gravity, the spacecraft deforms and the center of mass moves.

Let z_B denote the distance in the z_0 direction from the shuttle's center of mass 0 to the universal joint B. Note that the rigid-body center of mass is listed in Table 8.3. The first three eigenvalues are plotted versus the roll angle in Figs. 8.19a through 8.19c, each figure corresponding to a different value of z_B. Note that in all three cases, one and only one mode is always marginally stable. The first two modes are unstable for z_{B1} as evidenced by Fig. 8.19a. A slight increase in z_B from z_{B1} to z_{B2} yields stability in the region $-35^o < \theta < 20^o$. A further increase in z_B to z_{B3} yields an even wider stability range. Note that the plots are not symmetric because the flexible appendage is not symmetric. Physically, when the first mode becomes unstable, the structure begins to slew about the z_0 axis if no control force is applied. When the next mode becomes unstable the structure continues to roll with no external force application, so that it will begin to turn upside down.

Considering the plot for $z_B = z_{B1}$, if stabilizing control is applied, the structure can be rotated from $\theta = -40^o$ to $\theta = 30^o$ with

little effort to combat gravity. In fact, three dimensional stability curves, considering both pitch and roll, can be useful in determining an even more advantageous maneuver trajectory. The present laboratory model is stable at $\theta = 0$, so that $z_B = z_{B2}$ is used for the mathematical model. With the completion of the structure, the model will be updated and the stability reevaluated.

8.4 MANEUVER STRATEGY

The maneuver strategy of Chapter 5 was applied to the rigid-body model of the spacecraft. The actuator response was assumed to be of first-order as in Eq. (5.2) with a=-10 and b=1.

Figures 8.20a through 8.20c show the history of a minimum-time roll maneuver from 0° to 20° with M_{max} = 5 ft-lb. Both continuous and discrete time switching histories are plotted in these figures, with the + symbol denoting discrete switching and the Δ symbol denoting continuous switching time histories. There is a perceptible difference only at the switching states. The effect of the actuator response is to smooth the curves at the switching states. If actuator response is instantaneous, the acceleration is discontinuous.

Figures 8.21a and 8.21b illustrate the command forces and moments required at the universal joint to accomplish the 20° rotation. The forces are nonzero since the joint is not the rigid-body center of mass and the moments in the y_0 and z_0 directions are necessary because the roll axis is not a principal axis.

The histories of three other rotational maneuvers are also presented. The discrete-time switching history of a 0° to 30° minimum-

time rotation with M_{max} = 20 lb-ft is illustrated by Fig. 8.22a. Note that the acceleration overshoots the target state because of the discrete-time switching. Figures 8.22b and 8.22c illustrate the continuous-time switching histories of 0° to 180° rotations with M_{max} = 20 lb-ft and M_{max} = 60 lb-ft, respectively.

8.5 ACTUATOR RESPONSE

The effect of actuator response on the rigid-body maneuver history has been demonstrated in Sec. 8.4. In this section, the benefits of the inclusion of the actuators' equations of motion with the structure's equations of motion for control formulation are illustrated.

The space model, for which the natural frequencies are given by the third column of Table 8.4, is initially struck with an impulsive force of magnitude 5 lb in the y_0 direction. The structure is initially in a state of rest. The ensuing motion is modeled with 15 modes and the first 10 modes are controlled with natural control applied with distributed actuators and sensors. Both the classical form of natural control and natural control adapted for actuator dynamics is used to suppress the vibrations.

Figures 8.23a and 8.23b are plots of the total energy of the system versus the control performance for various values of the actuator response decay rate -a. The values of R in the performance functional, given by Eq. (7.8a), are 0.5 and 0.1 for Figs. 8.23a and 8.23b respectively, while q = 1 in both cases, for all modes. The symbol + signifies a solution with classical natural control, where actuator response is not accounted for. In all cases, the performance is improved

with inclusion of actuator dynamics in the control formulation. Of course, as $-a \to \infty$ this difference approaches zero. Note that, comparing Figs. 8.23a and 8.23b, this difference also depends on the value of R. As R decreases, the modal decay rate increases according to Eq. (7.38). Hence, the benefits derived from including the actuator response in the vibration control formulation depend on the ratio of the desired modal decay rate to the actuators' decay rate. Of course, as this ratio is decreased, the effect of the actuators' response becomes less important. As can be observed from a comparison of Figs. 8.22a-c, a similar conclusion can be made about the effect of actuator response on the maneuver control. In this case, the ratio of interest is that of the mean angular maneuver velocity to the actuator decay rate.

8.6 ZERO-GRAVITY ROTATIONAL MANEUVERS

In Sec. 8.3, it was shown that gravity has a great influence on the eigensolution of the structure. In this section, the dynamic effects of the maneuver on the first-order vibration problem are investigated. First, the eigensolution is shown to be time varying and nonself-adjoint during rotational maneuvers. Then, the vibration problems caused by the maneuver are demonstrated. Finally, the control techniques of Chapter 7 are used to suppress the vibration during the maneuver.

In Sec. 8.4, the strategies for three rotational maneuvers for the untethered spacecraft about the rigid-body mass center were presented: a 30° roll with M_{max} = 20 ft-lb, and two 180° rolls, one with M_{max} = 20 ft-lb and the other with M_{max} = 60 ft-lb. Tables 8.6 through 8.8 list the eigenvalues of the spacecraft during each of these maneuvers. The

vibration problem is nonself-adjoint during the maneuver, so that the real parts of the eigenvalues are nonzero during the rotations. Physically, this means that the initial configuration is not the equilibrium position during the rotation and, in fact, the equilibrium position is time varying.

The majority of the nonsymmetric parts of the stiffness matrix, expressed by Eq. (3.16g), are functions of the angular acceleration. A positive real part of an eigenvalue corresponds to growth of that mode's participation in the vibration of the structure. Referring to Table 8.6 through 8.8, we observe the participation of the flexible modes increases during the first half of the maneuver, when the angular acceleration is positive, and decreases during the last half. Note that the flexible modes most affected are the first two, modes 7 and 8.

The natural frequencies are also affected by the maneuvers. Most notably, the natural frequencies corresponding to four of the rigid-body modes are nonzero during the rotations. The natural frequencies of the flexible-body modes are also altered during the maneuver. Considering Eqs. (3.16f) and (3.17e), the stiffness matrix formed by terms involving only centrifugal accelerations and derived from the kinetic energy is negative semi-definite. On the other hand, the stiffness matrix of the appendage K_A includes centrifugal terms derived from the potential energy which are positive semi-definite (Ref. 3). Hence, the overall effect of the centrifugal terms on the natural frequencies is indefinite. The effects of the gyroscopic coefficients on the natural frequencies of an unsymmetric structure are also sign indefinite. Of

course, the fluctuations of the eigenvalues during the maneuver increase with the target angle and the acceleration rate, as can be concluded from a comparison of Table 8.6 through 8.8.

The remainder of this section is concerned with the simulation and control of the 30° and 180° roll maneuvers in space. The first fifteen modes are modeled for the simulations. First a simulation is presented without vibration controls, showing the excitation of the structure by centrifugal and tangential forces. Then, vibration control is added, demonstrating the control techniques of Chapter 7.

Figure 8.24a is a time-lapse plot of the spacecraft during the 30° roll maneuver. The rotation is produced by actuators located at the shuttle, so that centrifugal and tangential forces cause structural vibration. The view is from directly behind the structure, showing the y_0z_0 plane with the x_0 axis directed into the paper. At each plotting sampling time, two plots appear, one in dashed lines representing the structure as if it were rigid and the other representing the deformed structure. As the structure is accelerated, the appendage lags behind its desired position and then it bounces forward to precede the desired configuration during deceleration. When the maneuver ends, the appendage continues to vibrate about the desired target state. Note that the rigid-body error is small but discernible through the deflection of the y_0 axis.

Figure 8.24b is also a time-lapse plot of the 30° roll. However, this maneuver was produced by actuators distributed throughout the structure. This form of actuation obviously causes a great deal less

structural vibration. The distributed maneuver forces cancel the tangential disturbance forces and only centrifugal forces remain to cause structural vibration. Hence, an increase in the number of actuators used to produce the rotational moments reduces the vibration caused by the maneuver. In fact, the use of just ten actuators, six on the shuttle and four thrusters, two located at the end of the mast and two located at the hub of the antenna, decreases the amount of energy imparted to the structure during the maneuver significantly. Figure 8.25 shows a plot of the energy of the structure versus time for three cases, namely, distributed actuation, projected actuation with the above ten actuators and six actuators located on the shuttle. Note that both the steady-state energy level and the instantaneous energy are decreased by the addition of actuators.

The locations of the four thrusters used in the projection technique above were determined from a plot of the force distribution over the appendage for the case of distributed actuators. Figure 8.26 is such a plot where what appears to be the deformation of the appendage is actually the force distribution. The forces in the x_0 and y_0 directions at the hub of the antenna and the end of the mast contribute the most to the force distribution. Note that these locations have the highest mass concentrations, which is no accident.

The maneuver is of a relatively short duration, so that the tangential forces are of greater magnitude than the centrifugal forces, because the angular velocities remain relatively small. The mode mainly

excited during maneuver is mode 8, which is the mode with the greatest tangential force.

The control techniques of Chapter 7 were applied to control the vibration of the spacecraft during the 30° roll. In all the presented cases, R = 0.01 and q = 1.0 for all the controlled modes. The time constant of the actuators' equations of motion was assumed to be a = -10, as in the maneuver strategy. Figure 8.27 is a time-lapse plot of the spacecraft during the maneuver with uniform damping control suppressing the vibrations of the first 9 modes using the array of ten actuators discussed above. Comparing Figs. 8.27 and 8.24a, we conclude that uniform damping control provides excellent performance during the maneuver.

The spacecraft was maneuvered through the 30° angle with both distributed actuators and the 10 actuators used previously in this section. These 10 actuators were used for both maneuver control and vibration suppression first using natural control approximated with projected actuating and distributed sensing. Next, 10 sensors were collocated with the actuators and the maneuver was repeated using natural control approximated by projected sensing and actuating. Finally, uniform damping control was used with the same 10 collocated actuators and sensors.

Figures 8.28a and 8.28b show the total energy in the system and the total command effort versus time, respectively, for all four of the above mentioned control strategies. Note that, at the completion of the maneuver, energy is lower in all four strategies, and the performance

during the maneuver is always better compared to the case of no vibration suppression shown by Fig. 8.25. Distributed sensors and actuators yield the best performance by far. Note that uniform damping control performs almost as well as projected actuating and distributed sensing. This is to be expected, since the former is an approximation of the latter. While uniform damping control requires more effort, it also reduces vibration more effectively during the maneuver. However, uniform damping control being decentralized, requires only a finite number of sensors, equal to the number of actuators.

The case of projected actuating and sensing is clearly inferior to uniform damping control, even though both techniques were applied with the same collocated sensors and actuators. The difference lies in the feedback method. Uniform damping control is decentralized so that each sensor supplies information only for the collocated actuator, requiring no interpolation. On the other hand, the projected actuating and sensing strategy is centralized so that the modal states are estimated through interpolation of signals from all the sensors. The actuators are commanded from the estimated modal states. Hence, in order to reduce modal estimation error with projected sensing, more sensors are needed, as discussed in Chapter 7. Better modal filtering techniques can help to reduce the modal estimation error, but in general, more sensors than actuators are required.

The main control objective of the SCOLE project is aiming the antenna within a certain tolerance in minimum time. Hence, a study of the antenna rotations versus time is of interest. Figures 8.29a-c and

illustrate the instantaneous antenna rotations with respect to the 0 frame about the x_0, y_0 and z_0 axes, respectively. The plots include the responses produced during the maneuver with all four of the above control implementation techniques. The relative quality of performance is as mentioned above.

The effect of controlling only a finite set of modes is reflected in Fig. 8.29b in the form of residual motion of the uncontrolled modes. In reality, this residual motion will be eventually dissipated through passive damping. Uniform damping control dissipates energy in all of the modes, not just a finite set. From Fig. 8.29b, however, we observe that it is not very effective in controlling certain modes due to actuator placement. Nevertheless, with time, it does remove all of the energy from the system, unlike the other implementation techniques.

Figure 8.30 contains plots of the portion of the command moments applied on the shuttle in the x_0 direction for both natural control with distributed actuators and sensors and uniform damping control. Uniform damping control, using fewer actuators, requires more effort for both maneuver and vibration control. The moment required by uniform damping control is less smooth and is nonzero well after the maneuver because it is attempting to suppress the total vibration of the structure, not just a finite set of modes. The fact that uniform damping controls all of the modes helps to explain its requiring more actuator effort compared to its counterparts, as shown in Fig. 8.28b.

In reality, because of saturation, actuators can only produce a finite amount of force or moment. The effect of limited command forces

was investigated for the 30° roll maneuver and uniform damping control. The shuttle command forces and moments were limited to 2 lb and 20 ft-lb, respectively. The four thrusters on the appendage were each limited to 0.15 lb. These values correspond to saturation of the thruster on the antenna hub in the y_0 direction. Figure 8.31 contains plots of this command force versus time for limited and unlimited actuation. The corresponding plots of modal vibrational energy versus time in Fig. 8.32a show the adverse effect of command force truncation. The price for force truncation is increased vibrational energy as well as an associated increase in overall effort, as illustrated by Fig. 8.32b, although the control scheme is still effective.

The maneuver and control techniques are now demonstrated for a more extreme situation, a 180° roll maneuver with M_{max} = 60 ft-lb. From Fig. 8.22c, we conclude that this is a relatively severe maneuver in that a 180° roll, starting and ending at rest, takes place in less than 4 seconds. Also, the maximum angular velocity of the maneuver corresponds to 27% of the first flexible natural frequency. Moreover, Table 8.8 shows that this maneuver alters the system eigenvalues significantly. Attempting this maneuver with actuators located only on the shuttle and without vibration controls resulted in deformations of the appendage exceeding greatly the small elastic motions assumption. Figure 8.33a is a time-lapse plot of the structure during the maneuver in which the moments have been produced by distributed forces. The deformation is caused by the centrifugal disturbance force which is much greater than for the 30° maneuver.

The maneuver modal control forces, the tangential modal forces and the centrifugal modal forces were each summed for all modes and plotted as functions of time in Fig. 8.33b. The control force cancels the tangential force, according to Eq. (5.15b,c), and opposes the rigid-body portion of the centrifugal forces according to Eq. (5.15a). The remainder of the centrifugal force then excites the vibrations of the structure.

Natural control and uniform damping control were employed to suppress the vibration of the structure during the maneuver using R=.01 and q=1.0. First, natural control was applied with distributed actuators and sensors to establish a "best case". Uniform damping control was then applied with the same 10 actuators and sensors used previously. Finally, uniform damping control was used with two additional thrusters (and collocated sensors), one in the z_0 direction at the hub of the antenna and the other at the extreme tip of the antenna in the y_0 direction.

The time-lapse plots of the structure during the maneuver showed no discernible deformations for all three control techniques. Figures 8.34a and 8.34b show the total modal energy and actual command effort versus time, respectively, for three control implementation techniques. Figure 8.34c illustrates the antenna rotation about the x_0 direction for all three cases. The addition of just two actuators resulted in much better performance and a reduction in effort of approximately 50%. Hence, the maneuver and vibration control approach

is successful even in extreme situations and the necessary number of actuators depends on the performance requirements.

8.7 ROTATIONAL MANEUVERS IN THE LABORATORY EXPERIMENT

All the results presented in this section are for the 0° to 20° rotational maneuver about the x_0 axis (roll) with M_{max} = 5 ft-lb. With the present configuration of the SCOLE model, the only equilibrium position is the 0° position, so that a departure from this angle requires moments to counteract gravity, even when the structure is at rest. First, the laboratory model is rotated as if it were rigid, with the maneuver strategy accounting for the effects of gravity. Next, the gravitational correction is removed from the maneuver moments and forces and the rotation is repeated. Vibration control is then added to the control strategy and the need for shape control is demonstrated. Finally, the structure is maneuvered using both vibration and shape control, which together produce the desired performance. The first twelve modes are simulated and the initial state is the static equilibrium configuration.

Figure 8.35a is a time-lapse plot of the laboratory model during the maneuver in which the body is assumed to be rigid. The maneuver strategy of Fig. 8.21 was modified to include moments to offset the gravitational torques. No vibrational controls were used and the maneuver was carried out with actuators located at the shuttle. Because the appendage deforms during the maneuver, the rigid assumption for moment calculations results in an overcompensation for the gravity torques and errors on the order of the maneuver angle itself. Hence,

the deformation of the appendage affects the moments necessary to counterbalance the gravitational torques strongly.

Figure 8.35b is a time-lapse plot of the laboratory model during the same maneuver in which the strategy of Fig. 8.21 was followed with no correction for gravity. Again, no vibration control was used and the moments were produced with actuators located on the shuttle. Little rigid-body error has resulted, but the deformation of the apendage due to gravity is large. Figure 8.36a illustrates the energy in the system versus time. As in the preceding section, for other roll maneuvers, the mode mainly excited is the second flexible mode, mode 7 in the second column of Table 8.4.

Next, natural control implemented with distributed actuators and sensors was applied to the spacecraft along with the maneuver strategy given by Fig. 8.21. The constants in the performance functional were chosen as R=0.01 and q=1.0 for all 9 controlled modes. Figure 8.35c is the corresponding time-lapse plot. The appendage still lags its desired position for this case, though the error has been reduced. A comparison of Fig. 8.36a and Fig. 8.36b shows that both the energy fluctuations during the maneuver and the steady-state energy level have been reduced with the addition of natural control. The steady-state error is caused by the gravitational force.

Natural control is chiefly a vibration suppresser not a shape control. A decrease in R increases all the gains, not just the displacement control gain, which would be the case in snape control. Hence, the addition of shape control is necessary to counterbalance the

gravitational force. The distribution of the gravitational force depends on the mass distribution of the structure, which is known reasonably well. Thus, the shape control force can be open-loop for the laboratory experiment. Note that, as demonstrated, natural control does provide a small amount of shape control by virtue of displacement control. Hence, it can offset partially small steady-state errors.

The torques required to counteract gravity in the case in which the structure is regarded as rigid is also included in the shape control force. The gravitational force is distributed over the entire structure. Hence, if precise shape control is desired, the control force must also be distributed or at least be produced by a large number of discrete actuators dispersed throughout the structure.

A distributed shape control force was applied along with the maneuver controls but with no vibration control. Figure 8.37a is the coresponding plot of energy versus time. The energy fluctuates but the mean energy level rises only slightly with time. Without vibration control, the system is actually unstable which explains the rising mean energy level. Hence, vibration control is needed to stabilize the system as well as to suppress the vibrations. The command moments at the universal joint are plotted on Fig. 8.37b. Note that the magnitude of the shape control moment dwarfs the maneuver moment. A steady-state moment of about -26 ft-lb is required to maintain the steady-state configuration.

Next, natural control implemented with distributed actuators and sensors was applied to the structure along with the shape and maneuver

controls. The corresponding time-lapse plot is shown in Fig. 8.35d. The performance is excellent as can be seen from the plot of the system energy versus time of Fig. 8.38a. The antenna rotations are virtually nullified soon after the end of the maneuver. The most active of the antenna vibrational rotations is that about the x_0 axis, which is shown in Fig. 8.38b.

As demonstrated in Sec. 8.6, projected control implemented with relatively few actuators produces excellent vibration control. However, applying open-loop shape control with the projection technique and a finite number of actuators results in a steady-state error. Increasing the gains can reduce this error but results in some deformation. An alternative is to use natural control to help reduce the steady-state error with the shape control supporting the majority of the steady-state load. Note that when the vibration of the structure has subsided, the only feedback force for natural control is due to the displacement control, so that the process reduces to shape control. Hence, when precise aiming of the antenna is required, R can be decreased so that the displacement gain (along with the other gains) is increased. In this manner, the steady state error can be reduced to within the desired tolerance and the antenna locked on target.

Natural control, the shape control and the maneuver controls were all implemented with 23 actuators using the projected technique. A projected-sensing modal estimation was also used where the sensors were collocated with the actuators. Referring to Fig. 8.1, the actuator and sensor locations were as follows: thrusters and torquers in the x_0, y_0

and z_0 directions at the universal joint, torquers in the x_0 direction at node 4 and y_0 direction at node 6, thrusters in the x_0, y_0 and z_0 directions at nodes 8, 11 and 14, and thrusters in the x_0 direction at node 12 and y_0 direction at node 13.

The maneuver strategy ends at t=4.77 s. Starting at t=5.00 s, R was incrementally decreased by 10% at each sampling time from R=0.01 to R=0.0005. The coresponding plots of the system's energy versus time are shown in Fig. 8.39a and the corresponding plot of the antenna's vibrational rotation in the x_0 direction is shown in Fig. 8.61c. By increasing the gains at t=5.00 s, the steady-state error is reduced by more than one half within two seconds. A considerable amount of effort is required to provide shape control, as is illustrated by Fig. 8.61b which is a plot of the modal effort versus time. A hashed straight line has been added to the plot to accentuate the increase in slope at t=5.00 s corresponding to the increase in gains.

Table 8.1 Element Material Properties

	Stiffness			Inertia	
	Bending	Torsion	Axial	Mass	Moment
	$EI(lb\text{-}ft^2)$	$GJ(lb\text{-}ft^2)$	$EA(lb)$	$\frac{m}{h}(\frac{slugs}{ft})$	$\frac{I_{xx}}{m}(ft^2)$
Cable	2.0	8.0	$3.3120(10^6)$	.01160	$1.211(10^{-4})$
Mast	1,648	1,263	$3.9714(10^6)$	.01391	$8.302(10^{-4})$
Antenna	557	411.65	$1.3397(10^6)$	.00475	$8.327(10^{-4})$

Table 8.2 Lumped Masses Attached to the Shuttle

	Mass	Distance From Point 0		
	(slugs)	x(ft)	y(ft)	z(ft)
Stack 1	4.3478	-0.8177	-1.5312	1.4895
Stack 2	4.3478	-0.8021	1.5625	1.4895
CMG	1.064	3.0938	-0.0625	0.6615

Table 8.3 Mast and Universal Joint Locations

	Distance From Point 0		
	x(ft)	y(ft)	z(ft)
R.B. Mass Center	-.15385586	.011609637	.48217069
Mast Attachment	-.15385586	.011609637	-.375
True Mass Center	-.15456184	.010386841	.48172838
Universal Joint	-.15456184	.010386841	.49366246

Table 8.4 Natural Frequencies (Hz)

	Equilibrium Position		Zero Gravity (Space)	
Mode	Actual	Massless Cable	Actual	Rigid Antenna
1	0.0	0.0	0.0	0.0
2	0.02661800	0.02661800	0.0	0.0
3	0.03335345	0.03335345	0.0	0.0
4	0.27527161	0.27550803	0.0	0.0
5	0.27528201	0.27551848	0.0	0.0
6	1.02135153	1.02136222	0.95626111	0.95781737
7	1.09274338	1.09275532	1.02205468	1.02304393
8	2.86993771	2.86993909	2.85798288	2.91078995
9	4.14099978	4.14100682	4.12238565	4.77249201
10	7.21202381	7.21203514	7.13573328	7.53400307
11	11.8888566	11.8892693	11.8067296	14.3285908
12	11.9975825	----------	----------	----------
13	11.9979985	----------	----------	----------
14	14.5271386	14.5271319	14.4703039	18.0655372
15	17.8807340	17.8965361	0.0	0.0
16	23.9951935	----------	----------	
17	23.9951971	----------	----------	
18	29.4618566	29.4618689	29.3765971	
19	31.9790379	31.9790406	31.8650183	
20	35.6083428	35.6083908	35.5681068	

Table 8.5 Cantilever Natural Frequencies (Hz)

	Roll Angle (Deg)	
Mode	0	180
1	0.90329379	0.74059481
2	0.92231250	0.74130235
3	2.85838001	2.84157907
4	4.11631152	4.06401370
5	7.18829155	7.03295932
6	11.8569533	11.6900310
7	14.5078152	14.3982264
8	29.4282394	29.2763643
9	31.9410827	31.7363829

Table 8.6 Eigenvalues during 30° maneuver, M_{max}=20 lb-ft

EIGENVALUES-REAL (RAD/SEC)

TIME	MODE 1	MODE 2	MODE 3	MODE 4	MODE 5	MODE 6
0.00	0.000D+00	0.000D+00	0.000D+00	0.000D+00	0.000D+00	0.000D+00
0.26	-3.116D-06	1.471D-04	5.996D-05	-3.116D-06	5.996D-05	1.689D-06
0.52	-8.403D-06	3.953D-04	1.618D-04	-8.403D-06	1.618D-04	4.558D-06
0.78	2.628D-04	6.383D-04	-1.364D-05	-1.364D-05	2.628D-04	7.410D-06
1.04	-3.633D-04	8.745D-04	-1.883D-05	-1.883D-05	3.633D-04	1.025D-05
1.30	4.636D-04	1.103D-03	-2.398D-05	-2.398D-05	4.636D-04	1.309D-05
1.56	-3.684D-04	-8.921D-04	1.917D-05	1.917D-05	-3.684D-04	-1.038D-05
1.82	-3.472D-04	-8.533D-04	1.806D-05	1.806D-05	-3.472D-04	-9.784D-06
2.08	1.308D-05	-6.247D-04	-2.516D-04	1.308D-05	-2.516D-04	-7.089D-06
2.34	7.868D-06	-3.785D-04	-1.514D-04	-1.514D-04	7.868D-06	-4.264D-06
2.60	2.641D-06	-1.275D-04	-1.432D-06	-5.082D-05	2.641D-06	-5.082D-05
2.77	1.075D-22	-1.022D-22	7.569D-23	1.075D-22	7.569D-23	1.721D-22

TIME	MODE 7	MODE 8	MODE 9	MODE 10	MODE 11	MODE 12
0.00	0.000D+00	0.000D+00	0.000D+00	0.000D+00	0.000D+00	0.000D+00
0.26	1.689D-06	7.533D-07	7.533D-07	3.564D-07	3.564D-07	7.565D-08
0.52	4.558D-06	2.033D-06	2.033D-06	9.616D-07	9.616D-07	2.041D-07
0.78	7.410D-06	3.304D-06	3.304D-06	1.563D-06	1.563D-06	3.318D-07
1.04	1.025D-05	4.568D-06	4.568D-06	2.161D-06	2.161D-06	4.588D-07
1.30	1.309D-05	5.832D-06	5.832D-06	2.759D-06	2.759D-06	5.857D-07
1.56	-1.038D-05	-4.634D-06	-4.634D-06	-2.192D-06	-2.192D-06	-4.654D-07
1.82	-9.784D-06	-4.366D-06	-4.366D-06	-2.066D-06	-2.066D-06	-4.385D-07
2.08	-7.089D-06	-3.162D-06	-3.162D-06	-1.496D-06	-1.496D-06	-3.176D-07
2.34	-4.264D-06	-1.902D-06	-1.902D-06	-8.999D-07	-8.999D-07	-1.910D-07
2.60	-1.432D-06	-6.385D-07	-6.385D-07	-3.021D-07	-3.021D-07	-6.413D-08
2.77	1.721D-22	2.842D-14	2.842D-14	2.473D-22	2.473D-22	1.906D-21

NATURAL FREQUENCIES (HZ)

TIME	MODE 1	MODE 2	MODE 3	MODE 4	MODE 5	MODE 6
0.00	0.000D+00	0.000D+00	0.000D+00	0.000D+00	0.000D+00	0.000D+00
0.26	0.000D+00	0.000D+00	5.155D-02	5.462D-02	6.473D-02	6.772D-02
0.52	0.000D+00	0.000D+00	4.151D-02	4.936D-02	7.475D-02	8.211D-02
0.78	0.000D+00	0.000D+00	2.914D-02	4.208D-02	8.313D-02	9.480D-02
1.04	0.000D+00	0.000D+00	1.660D-02	3.481D-02	9.158D-02	1.074D-01
1.30	0.000D+00	0.000D+00	4.051D-03	2.771D-02	1.002D-01	1.199D-01
1.56	0.000D+00	0.000D+00	6.287D-04	2.350D-02	9.320D-02	1.120D-01
1.82	0.000D+00	0.000D+00	1.764D-02	3.525D-02	9.020D-02	1.055D-01
2.08	0.000D+00	0.000D+00	3.051D-02	4.288D-02	8.219D-02	9.339D-02
2.34	0.000D+00	0.000D+00	4.308D-02	5.038D-02	7.400D-02	8.087D-02
2.60	0.000D+00	0.000D+00	5.564D-02	5.804D-02	6.597D-02	6.832D-02
2.77	0.000D+00	0.000D+00	2.245D-06	2.245D-06	2.245D-06	2.245D-06

TIME	MODE 7	MODE 8	MODE 9	MODE 10	MODE 11	MODE 12
0.00	9.563D-01	1.022D+00	2.858D+00	4.122D+00	7.136D+00	1.181D+01
0.26	9.562D-01	1.023D+00	2.858D+00	4.122D+00	7.136D+00	1.181D+01
0.52	9.561D-01	1.023D+00	2.858D+00	4.123D+00	7.136D+00	1.181D+01
0.78	9.558D-01	1.023D+00	2.858D+00	4.123D+00	7.136D+00	1.181D+01
1.04	9.555D-01	1.024D+00	2.858D+00	4.124D+00	7.136D+00	1.181D+01
1.30	9.552D-01	1.025D+00	2.858D+00	4.125D+00	7.136D+00	1.181D+01
1.56	9.554D-01	1.024D+00	2.858D+00	4.125D+00	7.136D+00	1.181D+01
1.82	9.557D-01	1.023D+00	2.858D+00	4.124D+00	7.136D+00	1.181D+01
2.08	9.560D-01	1.022D+00	2.858D+00	4.123D+00	7.136D+00	1.181D+01
2.34	9.562D-01	1.022D+00	2.858D+00	4.123D+00	7.136D+00	1.181D+01
2.60	9.563D-01	1.022D+00	2.858D+00	4.122D+00	7.136D+00	1.181D+01
2.77	9.563D-01	1.022D+00	2.858D+00	4.122D+00	7.136D+00	1.181D+01

Table 8.7 Eigenvalues during 180° maneuver, M_{max}=20 lb-ft

EIGENVALUES-REAL (RAD/SEC)

TIME	MODE 1	MODE 2	MODE 3	MODE 4	MODE 5	MODE 6
0.00	0.000D+00	0.000D+00	0.000D+00	0.000D+00	0.000D+00	0.000D+00
0.60	1.930D-04	4.708D-04	-1.002D-05	-1.002D-05	1.930D-04	5.439D-06
1.20	4.250D-04	1.016D-03	-2.200D-05	-2.200D-05	4.250D-04	1.199D-05
1.80	6.558D-04	1.519D-03	-3.375D-05	-3.375D-05	6.558D-04	1.855D-05
2.40	8.851D-04	-4.517D-05	1.971D-03	-4.517D-05	8.851D-04	2.514D-05
3.00	-5.617D-05	2.372D-03	-5.617D-05	1.112D-03	1.112D-03	3.175D-05
3.60	5.626D-05	-2.258D-03	5.626D-05	-1.077D-03	-1.077D-03	-3.037D-05
4.20	-9.004D-04	-1.999D-03	4.691D-05	4.691D-05	-9.004D-04	-2.539D-05
4.80	-6.707D-04	-1.566D-03	3.491D-05	3.491D-05	-6.707D-04	-1.890D-05
5.40	-4.398D-04	-1.068D-03	2.287D-05	2.287D-05	-4.398D-04	-1.239D-05
6.00	-2.081D-04	-5.185D-04	1.082D-05	1.082D-05	-2.081D-04	-5.863D-06
6.58	1.022D-22	7.031D-23	-4.557D-16	1.022D-22	-4.557D-16	1.960D-22

TIME	MODE 7	MODE 8	MODE 9	MODE 10	MODE 11	MODE 12
0.00	0.000D+00	0.000D+00	0.000D+00	0.000D+00	0.000D+00	0.000D+00
0.60	5.439D-06	2.425D-06	2.425D-06	1.147D-06	1.147D-06	2.436D-07
1.20	1.199D-05	5.346D-06	5.346D-06	2.529D-06	2.529D-06	5.369D-07
1.80	1.855D-05	8.261D-06	8.261D-06	3.907D-06	3.907D-06	8.296D-07
2.40	2.514D-05	1.118D-05	1.118D-05	5.285D-06	5.285D-06	1.122D-06
3.00	3.175D-05	1.409D-05	1.409D-05	6.660D-06	6.660D-06	1.415D-06
3.60	-3.037D-05	-1.362D-05	-1.362D-05	-6.444D-06	-6.444D-06	-1.369D-06
4.20	-2.539D-05	-1.136D-05	-1.136D-05	-5.374D-06	-5.374D-06	-1.142D-06
4.80	-1.890D-05	-8.447D-06	-8.447D-06	-3.996D-06	-3.996D-06	-8.486D-07
5.40	-1.239D-05	-5.531D-06	-5.531D-06	-2.617D-06	-2.617D-06	-5.556D-07
6.00	-5.863D-06	-2.615D-06	-2.615D-06	-1.237D-06	-1.237D-06	-2.627D-07
6.58	1.960D-22	2.382D-22	2.382D-22	3.300D-22	3.300D-22	2.920D-22

NATURAL FREQUENCIES (HZ)

TIME	MODE 1	MODE 2	MODE 3	MODE 4	MODE 5	MODE 6
0.00	0.000D+00	0.000D+00	0.000D+00	0.000D+00	0.000D+00	0.000D+00
0.60	0.000D+00	0.000D+00	3.775D-02	4.715D-02	7.735D-02	8.605D-02
1.20	0.000D+00	0.000D+00	8.878D-03	3.042D-02	9.686D-02	1.151D-01
1.80	0.000D+00	0.000D+00	1.442D-02	2.009D-02	1.174D-01	1.440D-01
2.40	0.000D+00	0.000D+00	0.000D+00	4.905D-02	1.390D-01	1.730D-01
3.00	0.000D+00	0.000D+00	1.398D-02	7.802D-02	1.617D-01	2.020D-01
3.60	0.000D+00	0.000D+00	1.700D-02	8.103D-02	1.619D-01	2.022D-01
4.20	0.000D+00	0.000D+00	1.013D-03	5.089D-02	1.404D-01	1.748D-01
4.80	0.000D+00	0.000D+00	1.353D-02	2.193D-02	1.187D-01	1.459D-01
5.40	0.000D+00	0.000D+00	7.039D-03	2.939D-02	9.813D-02	1.169D-01
6.00	0.000D+00	0.000D+00	3.600D-02	4.614D-02	7.862D-02	8.796D-02
6.58	0.000D+00	0.000D+00	2.757D-07	2.757D-07	2.757D-07	2.757D-07

TIME	MODE 7	MODE 8	MODE 9	MODE 10	MODE 11	MODE 12
0.00	9.563D-01	1.022D+00	2.858D+00	4.122D+00	7.136D+00	1.181D+01
0.60	9.560D-01	1.023D+00	2.858D+00	4.123D+00	7.136D+00	1.181D+01
1.20	9.553D-01	1.024D+00	2.858D+00	4.124D+00	7.136D+00	1.181D+01
1.80	9.542D-01	1.027D+00	2.858D+00	4.127D+00	7.137D+00	1.181D+01
2.40	9.527D-01	1.030D+00	2.859D+00	4.132D+00	7.138D+00	1.181D+01
3.00	9.510D-01	1.034D+00	2.859D+00	4.137D+00	7.139D+00	1.181D+01
3.60	9.510D-01	1.033D+00	2.859D+00	4.137D+00	7.140D+00	1.181D+01
4.20	9.527D-01	1.029D+00	2.859D+00	4.132D+00	7.138D+00	1.181D+01
4.80	9.542D-01	1.026D+00	2.858D+00	4.128D+00	7.137D+00	1.181D+01
5.40	9.554D-01	1.023D+00	2.858D+00	4.125D+00	7.136D+00	1.181D+01
6.00	9.561D-01	1.022D+00	2.858D+00	4.123D+00	7.136D+00	1.181D+01
6.58	9.563D-01	1.022D+00	2.858D+00	4.122D+00	7.136D+00	1.181D+01

Table 8.8 Eigenvalues during 180° maneuver, $\dot{M}_{max}$=60 lb-ft

EIGENVALUES-REAL (RAD/SEC)

TIME	MODE 1	MODE 2	MODE 3	MODE 4	MODE 5	MODE 6
0.00	0.000D+00	0.000D+00	0.000D+00	0.000D+00	0.000D+00	0.000D+00
0.35	8.541D-04	2.026D-03	-4.433D-05	-4.433D-05	8.541D-04	2.407D-05
0.70	2.082D-03	4.681D-03	-1.074D-04	-1.074D-04	2.082D-03	5.883D-05
1.05	3.283D-03	6.840D-03	-1.677D-04	-1.677D-04	3.283D-03	9.328D-05
1.40	4.464D-03	-2.246D-04	8.559D-03	-2.246D-04	4.464D-03	1.278D-04
1.75	-2.771D-04	9.953D-03	-2.771D-04	5.618D-03	5.618D-03	1.624D-04
2.10	2.429D-04	-8.306D-03	2.429D-04	-4.749D-03	-4.749D-03	-1.357D-04
2.45	2.395D-04	-9.019D-03	2.395D-04	-4.669D-03	-4.669D-03	-1.329D-04
2.80	1.814D-04	-7.507D-03	1.814D-04	-3.517D-03	-3.517D-03	-9.966D-05
3.15	-2.320D-03	-5.438D-03	1.202D-04	1.202D-04	-2.320D-03	-6.552D-05
3.50	5.758D-05	-2.788D-03	-1.109D-03	5.758D-05	-1.109D-03	-3.126D-05
3.85	3.883D-09	-1.859D-07	-2.105D-09	-7.471D-08	3.883D-09	-7.471D-08

TIME	MODE 7	MODE 8	MODE 9	MODE 10	MODE 11	MODE 12
0.00	0.000D+00	0.000D+00	0.000D+00	0.000D+00	0.000D+00	0.000D+00
0.35	2.407D-05	1.073D-05	1.073D-05	5.078D-06	5.078D-06	1.078D-06
0.70	5.883D-05	2.622D-05	2.622D-05	1.240D-05	1.240D-05	2.634D-06
1.05	9.328D-05	4.154D-05	4.154D-05	1.964D-05	1.964D-05	4.173D-06
1.40	1.278D-04	5.684D-05	5.684D-05	2.686D-05	2.686D-05	5.710D-06
1.75	1.624D-04	7.212D-05	7.212D-05	3.405D-05	3.405D-05	7.246D-06
2.10	-1.357D-04	-6.095D-05	-6.095D-05	-2.879D-05	-2.879D-05	-6.130D-06
2.45	-1.329D-04	-5.950D-05	-5.950D-05	-2.812D-05	-2.812D-05	-5.981D-06
2.80	-9.966D-05	-4.454D-05	-4.454D-05	-2.106D-05	-2.106D-05	-4.476D-06
3.15	-6.552D-05	-2.925D-05	-2.925D-05	-1.383D-05	-1.383D-05	-2.938D-06
3.50	-3.126D-05	-1.394D-05	-1.394D-05	-6.596D-06	-6.596D-06	-1.400D-06
3.85	-2.105D-09	-9.386D-10	-9.386D-10	-4.441D-10	-4.441D-10	-9.426D-11

NATURAL FREQUENCIES (HZ)

TIME	MODE 1	MODE 2	MODE 3	MODE 4	MODE 5	MODE 6
0.00	0.000D+00	0.000D+00	0.000D+00	0.000D+00	0.000D+00	0.000D+00
0.35	0.000D+00	0.000D+00	6.908D-02	8.326D-02	1.291D-01	1.424D-01
0.70	0.000D+00	0.000D+00	2.040D-02	5.543D-02	1.643D-01	1.942D-01
1.05	0.000D+00	0.000D+00	2.717D-02	3.023D-02	2.001D-01	2.449D-01
1.40	0.000D+00	0.000D+00	0.000D+00	8.092D-02	2.378D-01	2.956D-01
1.75	0.000D+00	0.000D+00	2.389D-02	1.316D-01	2.776D-01	3.463D-01
2.10	0.000D+00	0.000D+00	3.789D-02	1.491D-01	2.758D-01	3.435D-01
2.45	0.000D+00	0.000D+00	4.805D-03	9.109D-02	2.451D-01	3.052D-01
2.80	0.000D+00	0.000D+00	2.197D-02	4.019D-02	2.073D-01	2.549D-01
3.15	0.000D+00	0.000D+00	1.050D-02	4.987D-02	1.712D-01	2.042D-01
3.50	0.000D+00	0.000D+00	6.119D-02	7.920D-02	1.369D-01	1.535D-01
3.85	0.000D+00	0.000D+00	2.969D-02	2.970D-02	2.975D-02	2.977D-02

TIME	MODE 7	MODE 8	MODE 9	MODE 10	MODE 11	MODE 12
0.00	9.563D-01	1.022D+00	2.858D+00	4.122D+00	7.136D+00	1.181D+01
0.35	9.557D-01	1.024D+00	2.858D+00	4.123D+00	7.136D+00	1.181D+01
0.70	9.539D-01	1.028D+00	2.858D+00	4.128D+00	7.137D+00	1.181D+01
1.05	9.511D-01	1.034D+00	2.859D+00	4.136D+00	7.139D+00	1.181D+01
1.40	9.479D-01	1.043D+00	2.860D+00	4.149D+00	7.142D+00	1.182D+01
1.75	9.445D-01	1.052D+00	2.861D+00	4.165D+00	7.147D+00	1.182D+01
2.10	9.439D-01	1.052D+00	2.861D+00	4.168D+00	7.147D+00	1.182D+01
2.45	9.472D-01	1.042D+00	2.860D+00	4.152D+00	7.143D+00	1.182D+01
2.80	9.507D-01	1.033D+00	2.859D+00	4.139D+00	7.140D+00	1.181D+01
3.15	9.538D-01	1.026D+00	2.858D+00	4.130D+00	7.138D+00	1.181D+01
3.50	9.559D-01	1.022D+00	2.858D+00	4.124D+00	7.136D+00	1.181D+01
3.85	9.563D-01	1.022D+00	2.858D+00	4.122D+00	7.136D+00	1.181D+01

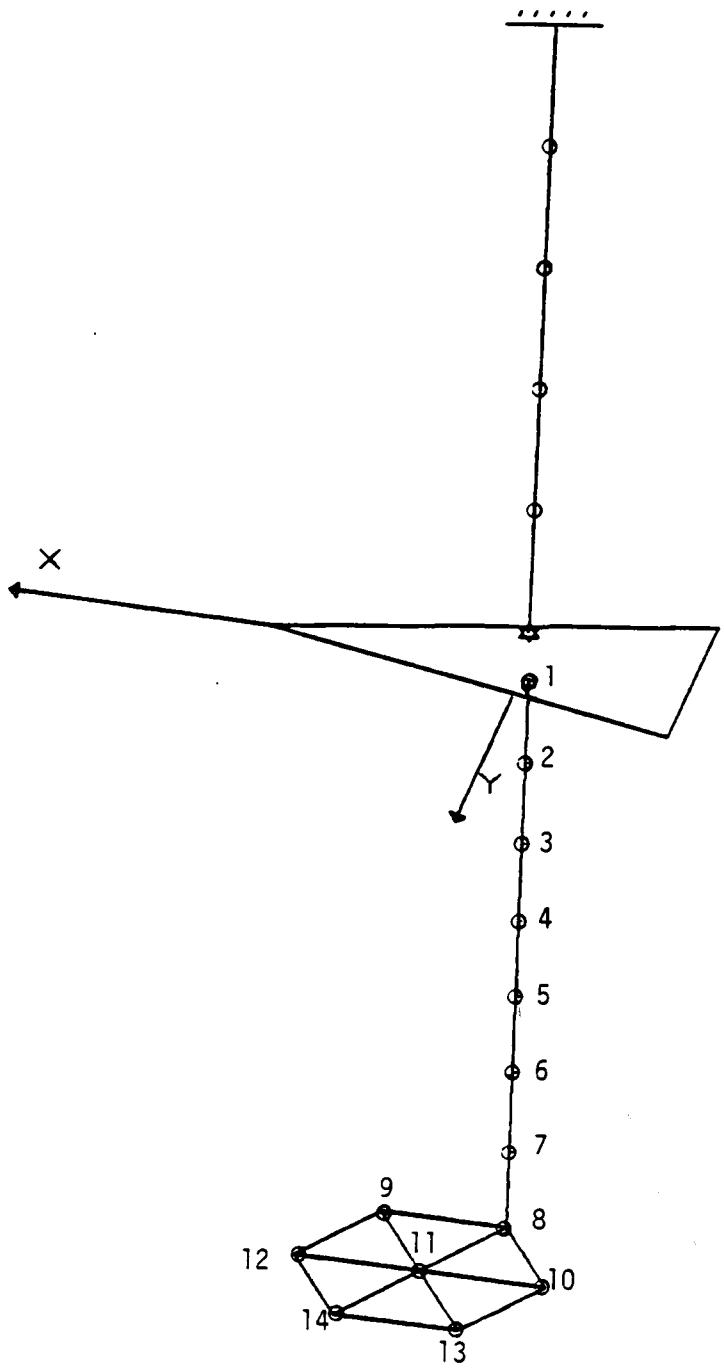

Figure 8.1 SCOLE configuration showing nodal locations.

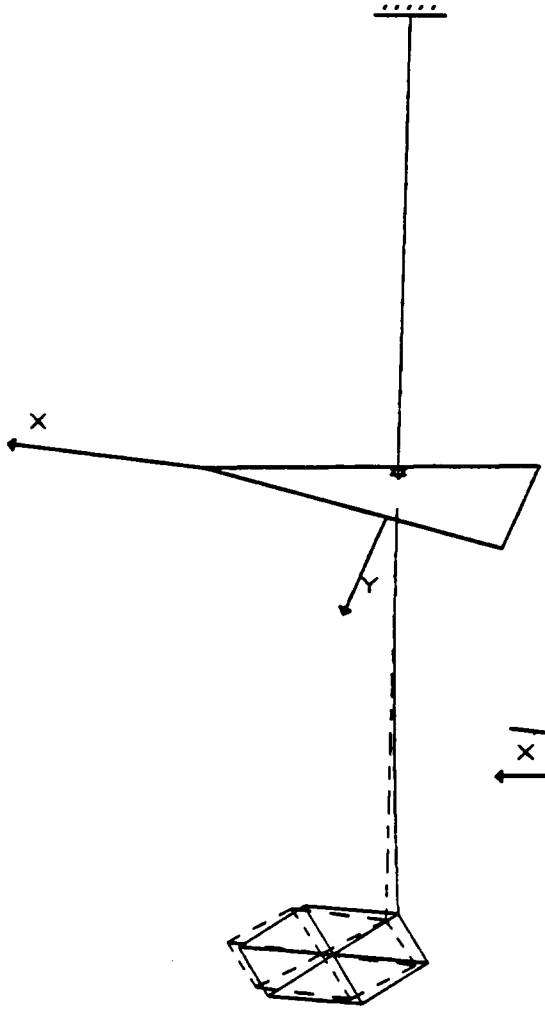

Figure 8.2 Static deflection, FACT = 2.5

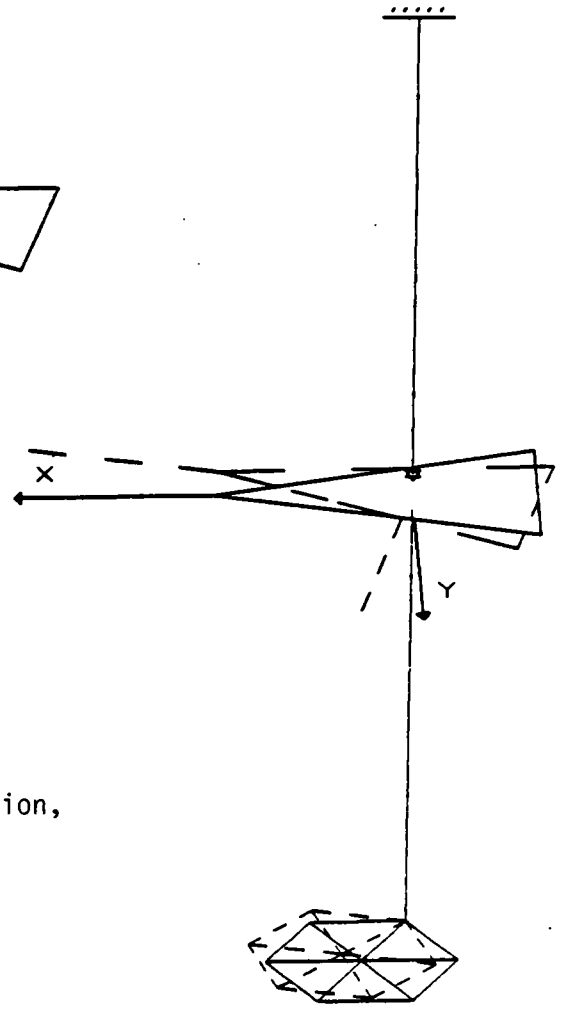

Figure 8.3 Mode 1, FACT = 0.25, 0.000001 Hz

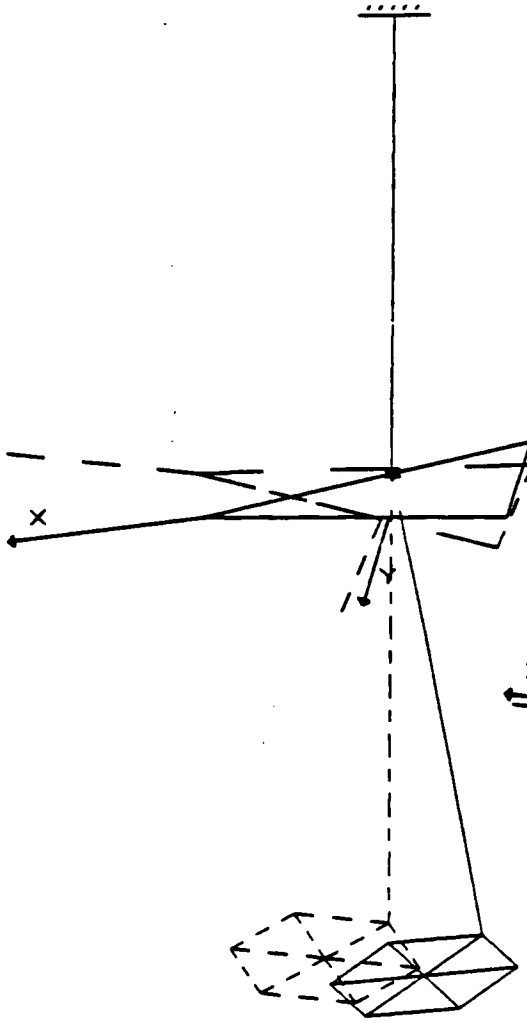

Figure 8.4 Mode 2, FACT = 0.25,
0.026618 Hz

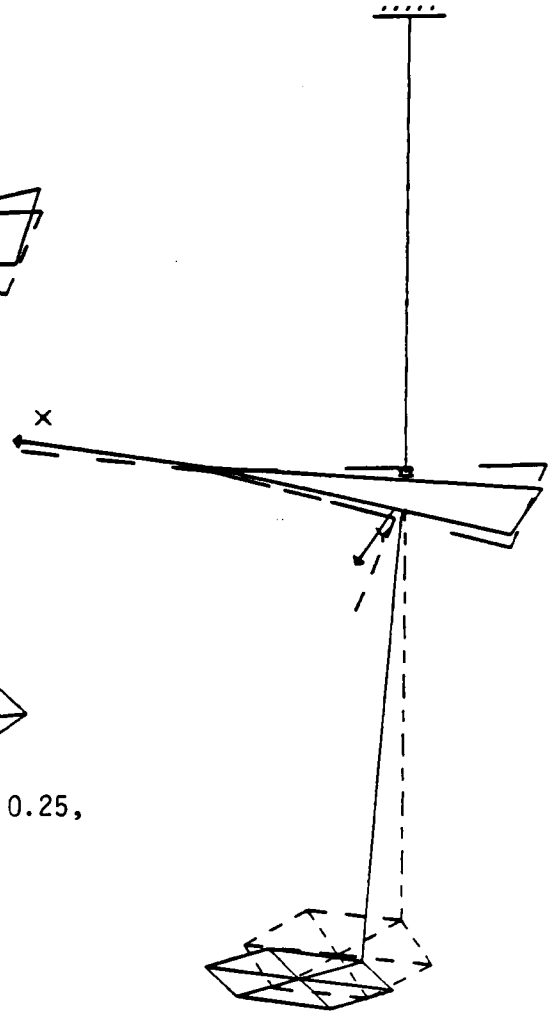

Figure 8.5 Mode 3, FACT = 0.25,
0.033353 Hz

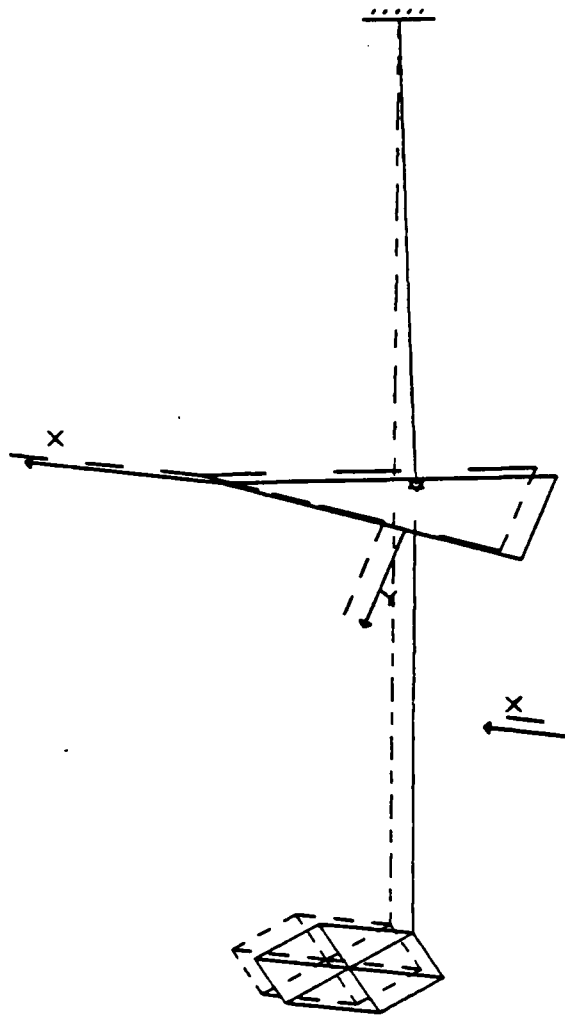

Figure 8.6 Mode 4, FACT = 0.50, 0.275272 Hz

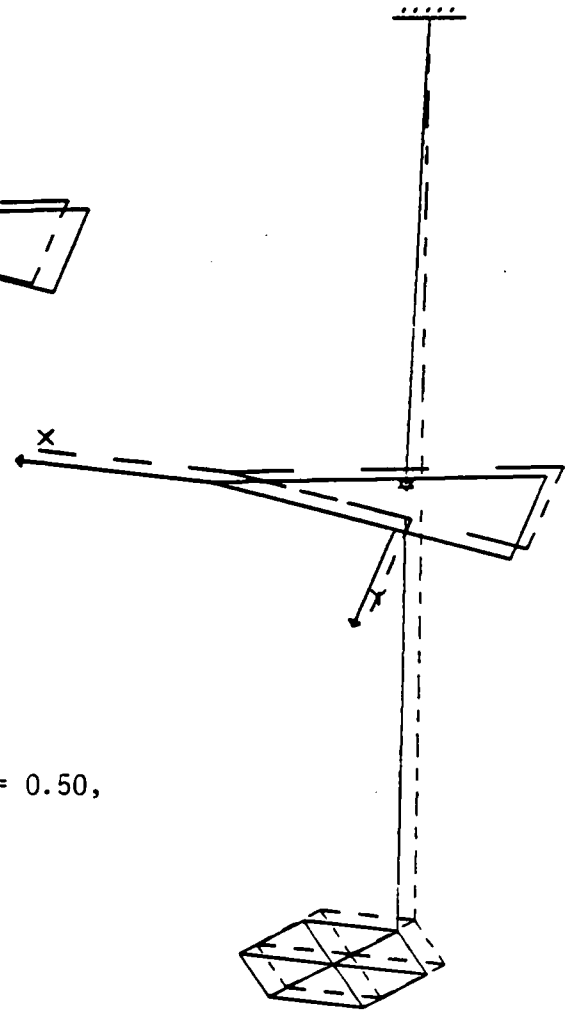

Figure 8.7 Mode 5, FACT = 0.50, 0.275282 Hz

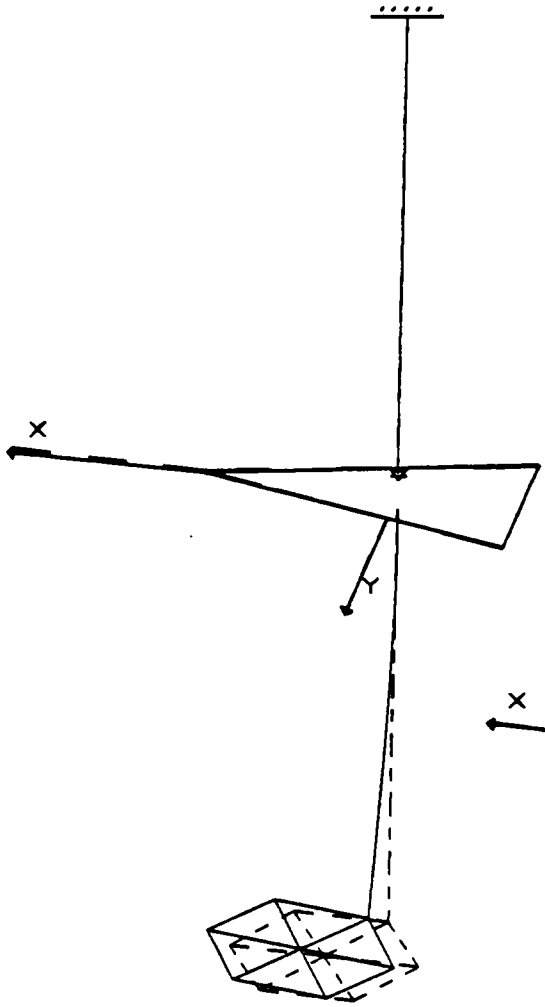

Figure 8.8 Mode 6, FACT = 0.75, 1.021351 Hz

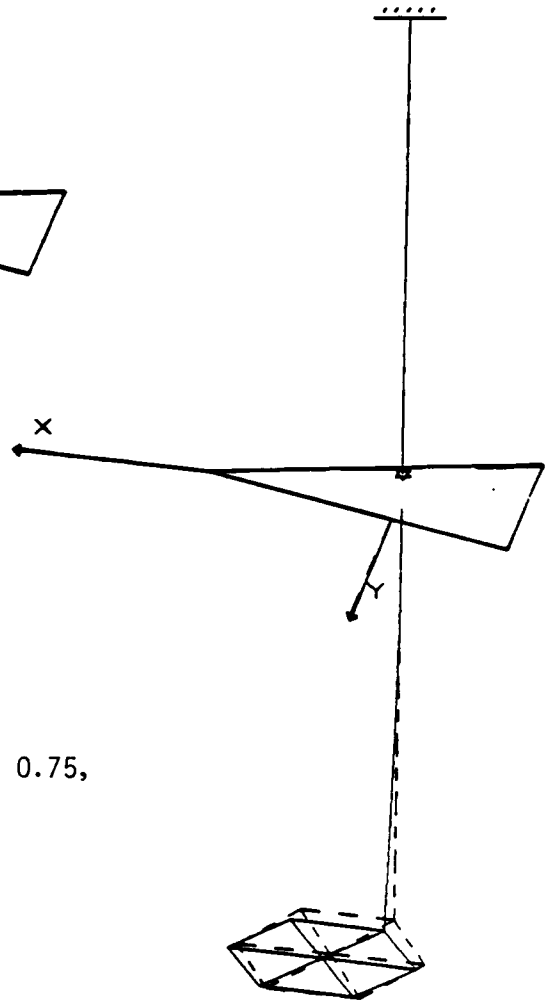

Figure 8.9 Mode 7, FACT = 0.75, 1.092742 Hz

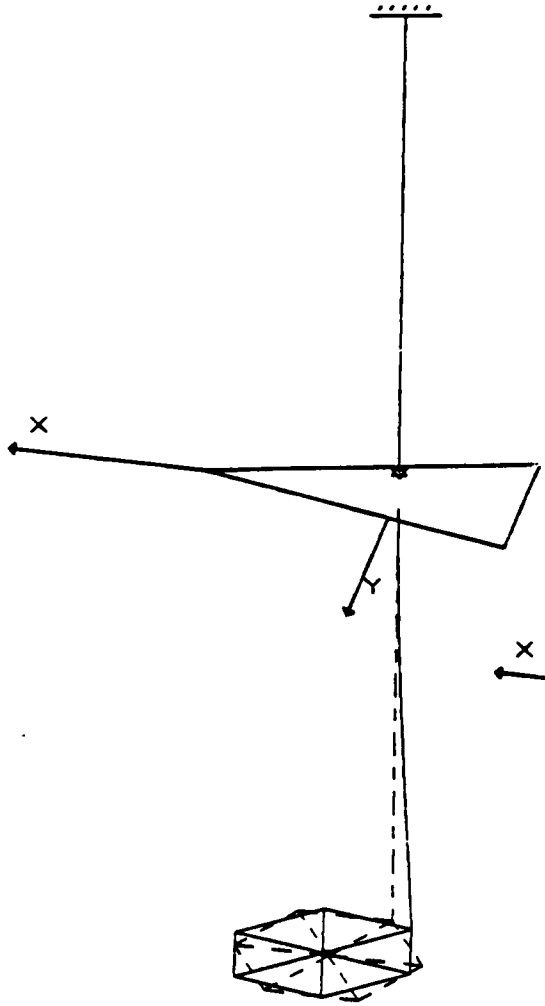

Figure 8.10 Mode 8, FACT = 0.75, 2.869936 Hz

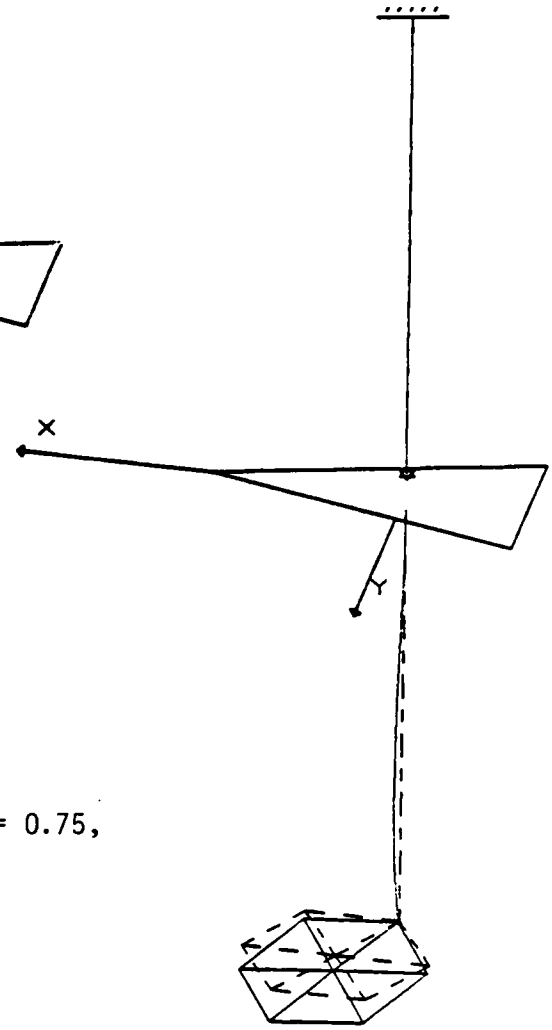

Fiugre 8.11 Mode 9, FACT = 0.75, 4.140995 Hz

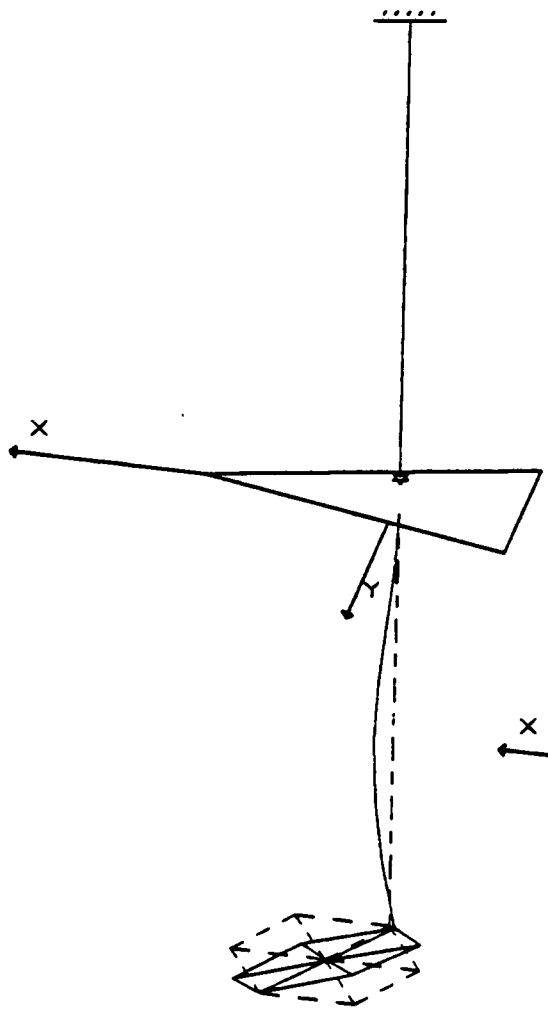

Figure 8.12 Mode 10, FACT = 0.75, 7.212018 Hz

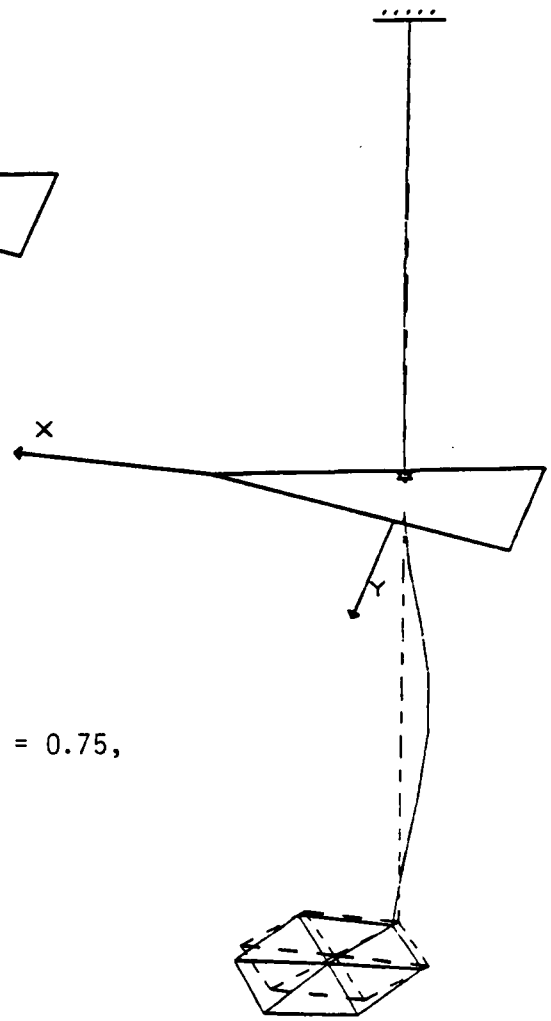

Figure 8.13 Mode 11, FACT = 0.75, 11.888850 Hz

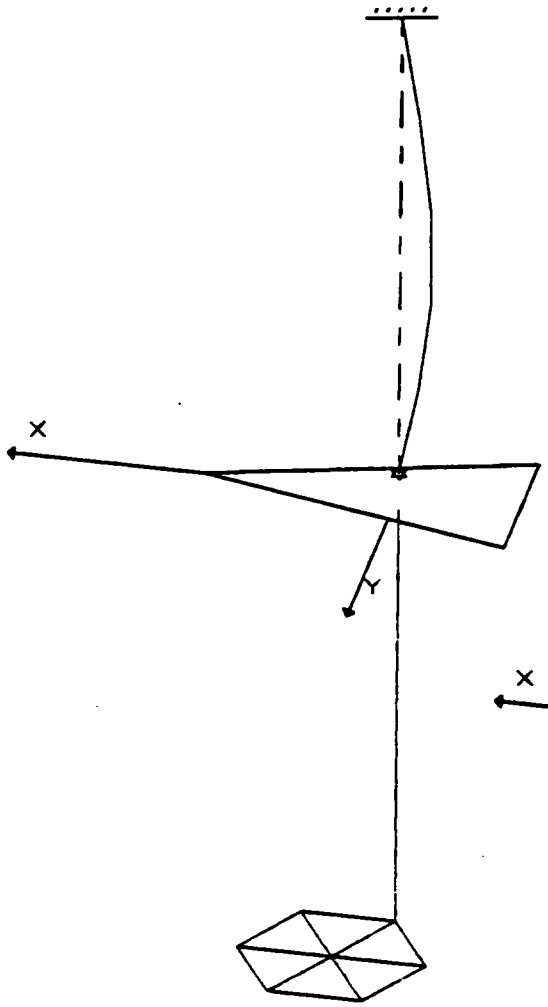

Figure 8.14 Mode 12, FACT = 0.75,
11.997580 Hz

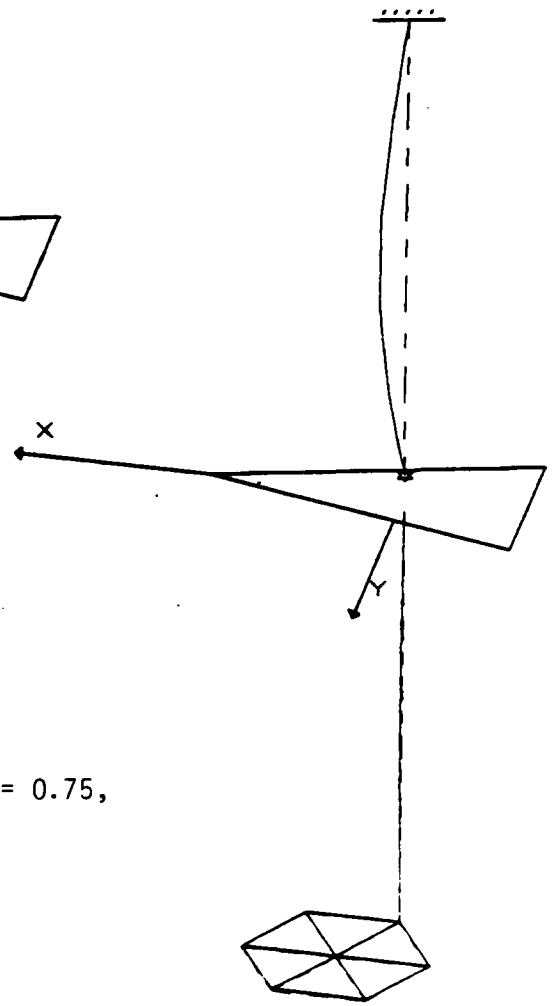

Figure 8.15 Mode 13, FACT = 0.75,
11.997990 Hz

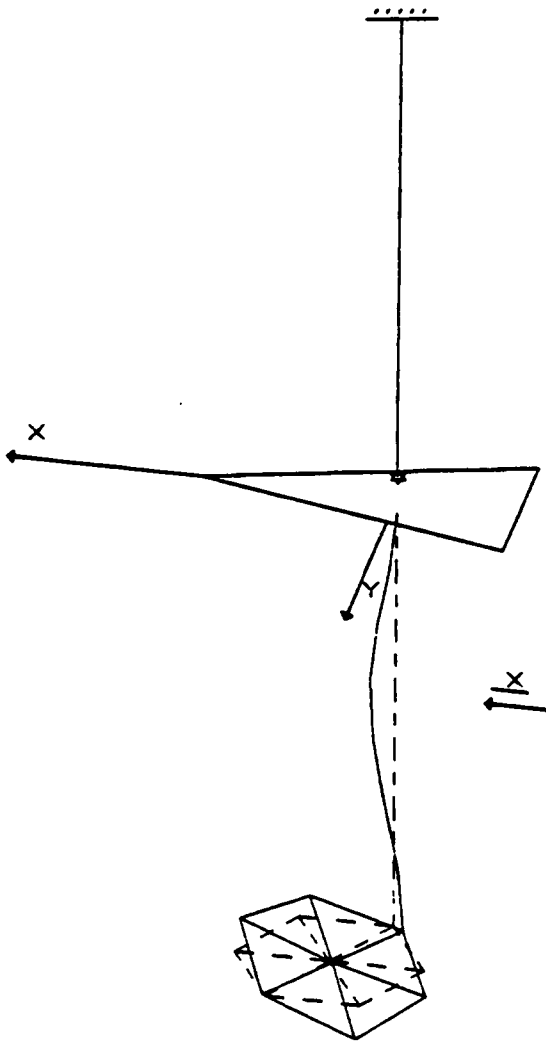

Figure 8.16 Mode 14, FACT = 0.75,
14.527130 Hz

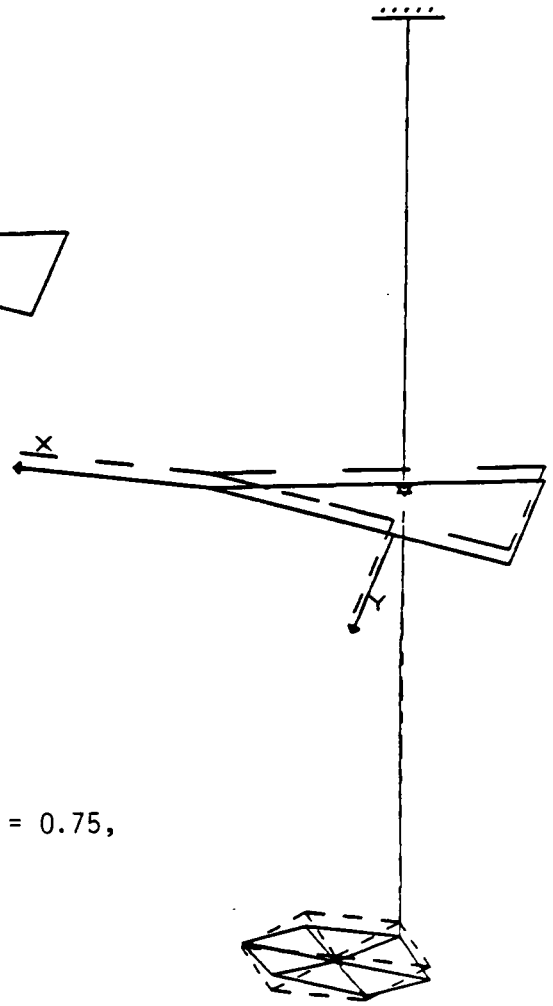

Figure 8.17 Mode 15, FACT = 0.75,
17.880720 Hz

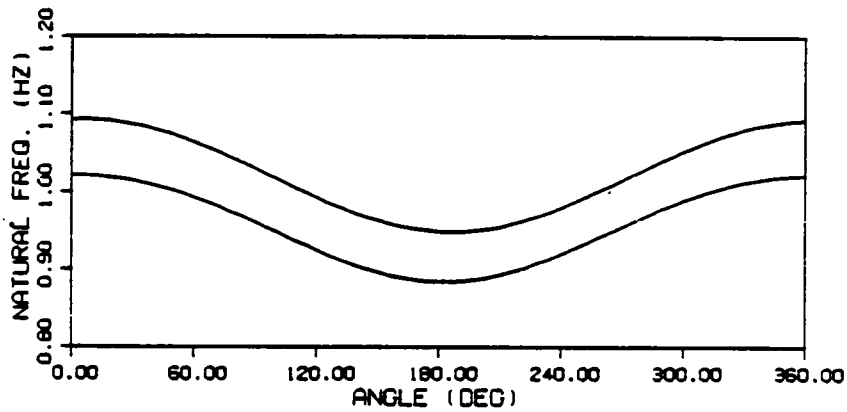

Figure 8.18 First two bending frequencies vs. roll angle.

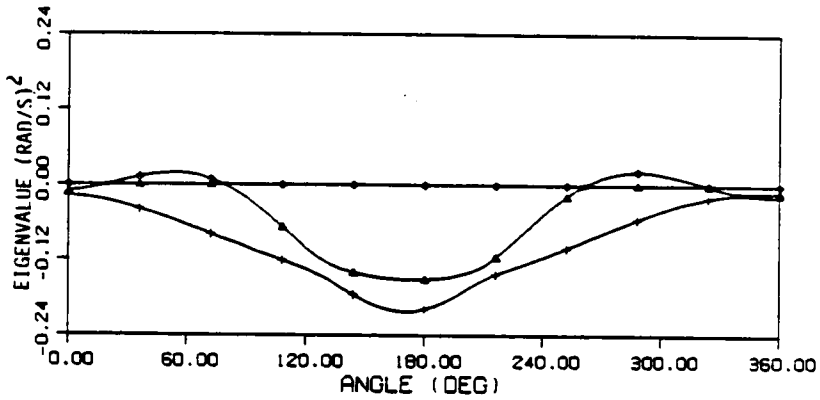

a) Z_{B1} = 0.490662 ft

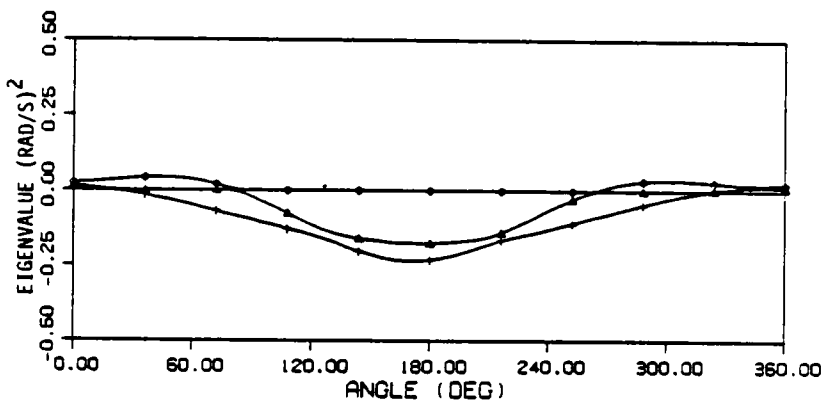

b) Z_{B2} = 0.493662 ft

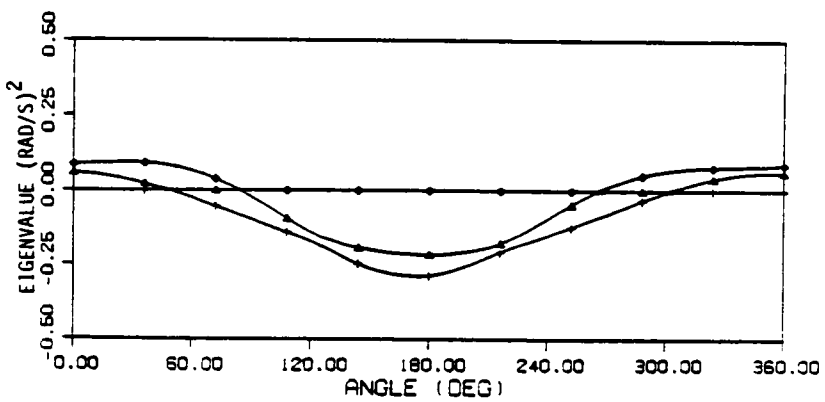

c) Z_{B3} = 0.498662 ft

Figure 8.19 First three eigenvalues vs. roll angle.

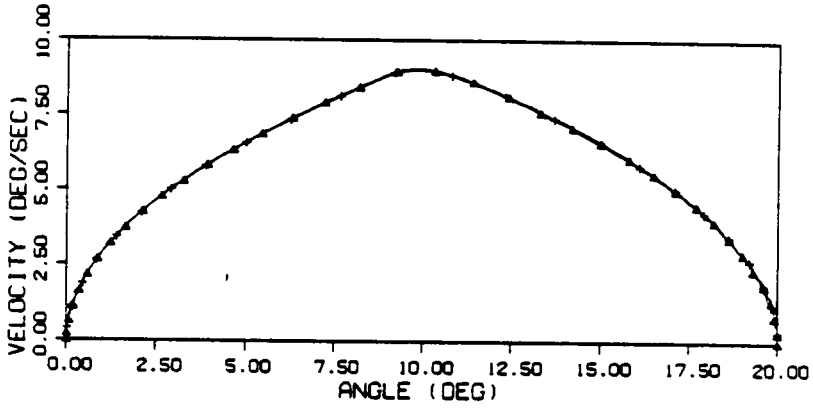

a) Angular velocity vs. angle

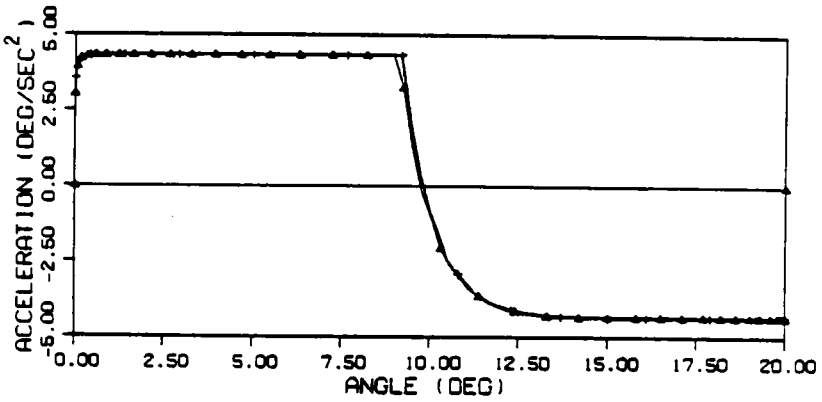

b) Angular acceleration vs. angle

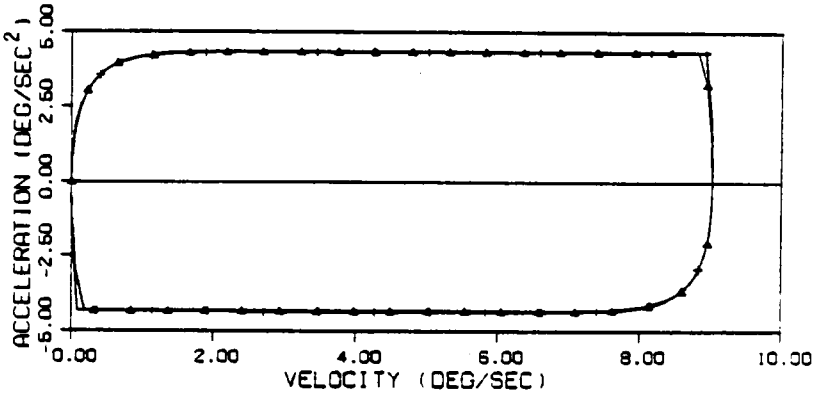

c) Angular acceleration vs. velocity

Figure 8.20 Maneuver strategy for 20° roll with M_{max} = 5 ft-lb.

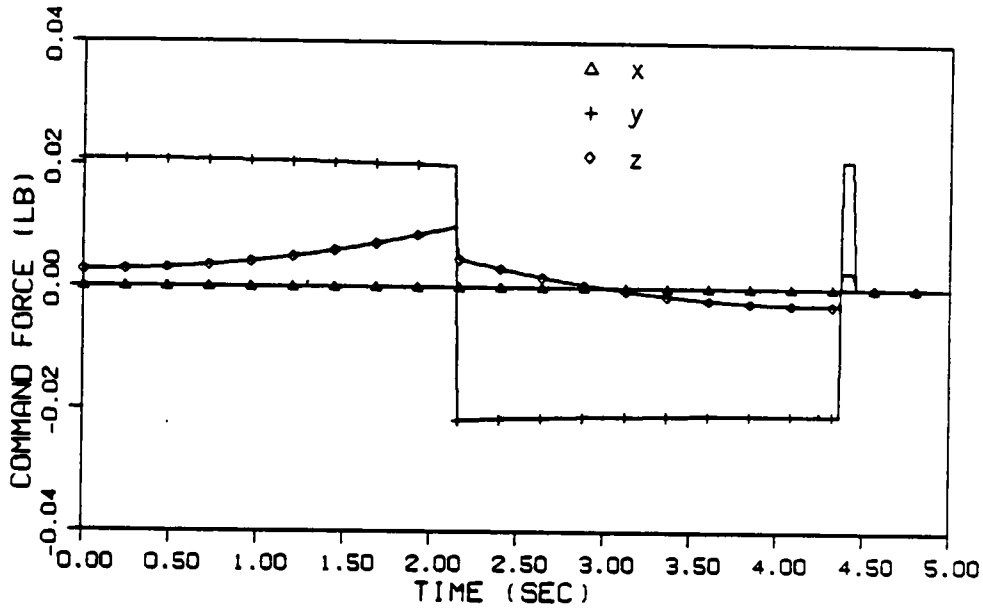

a) Forces at universal joint

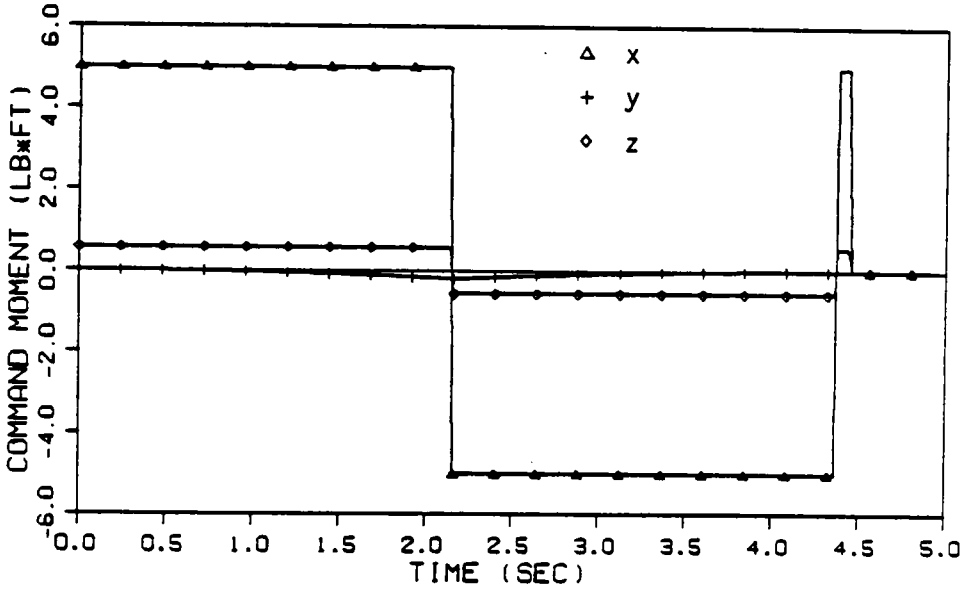

b) Moments about universal joint

Figure 8.21 Force and moment policies for 20° maneuver.

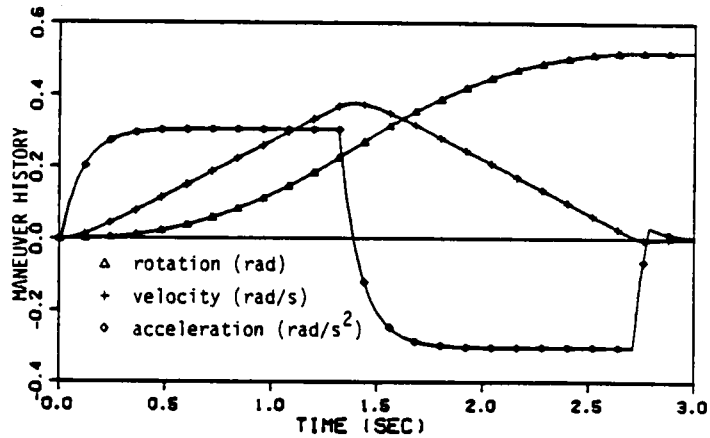

a) 30° roll, M_{max} = 20 ft-lb.

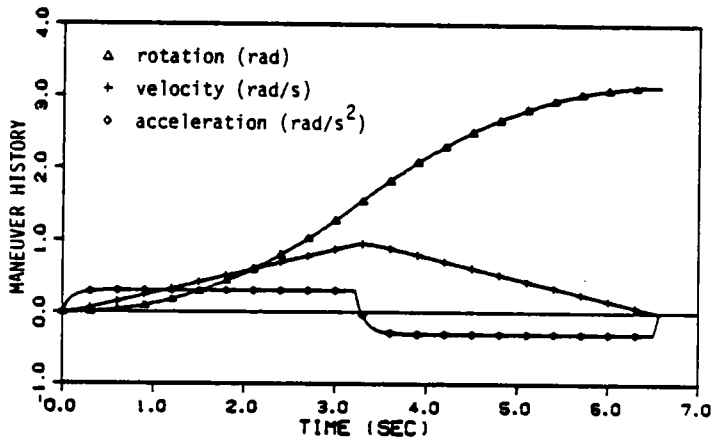

b) 180° roll, M_{max} = 20 ft-lb.

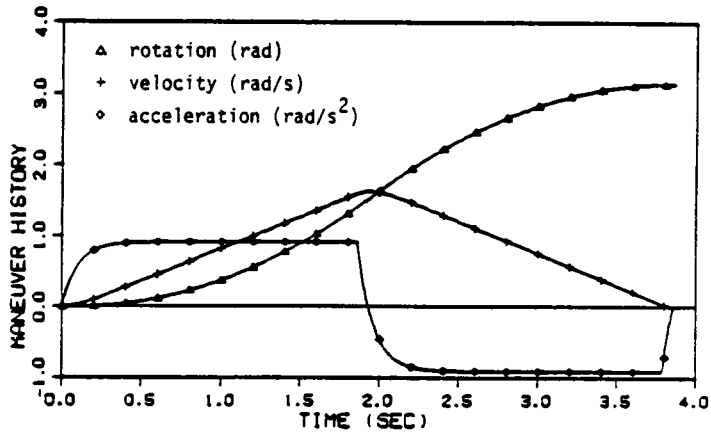

c) 180° roll, M_{max} = 60 ft-lb.

Figure 8.22 Comparison of maneuver strategies.

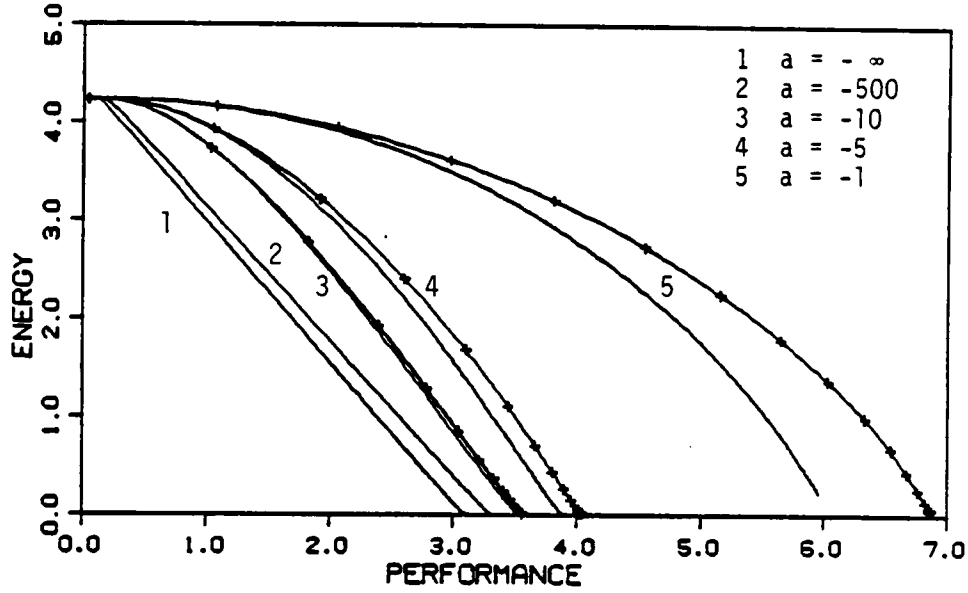

a) R = 0.5, g = 1.0.

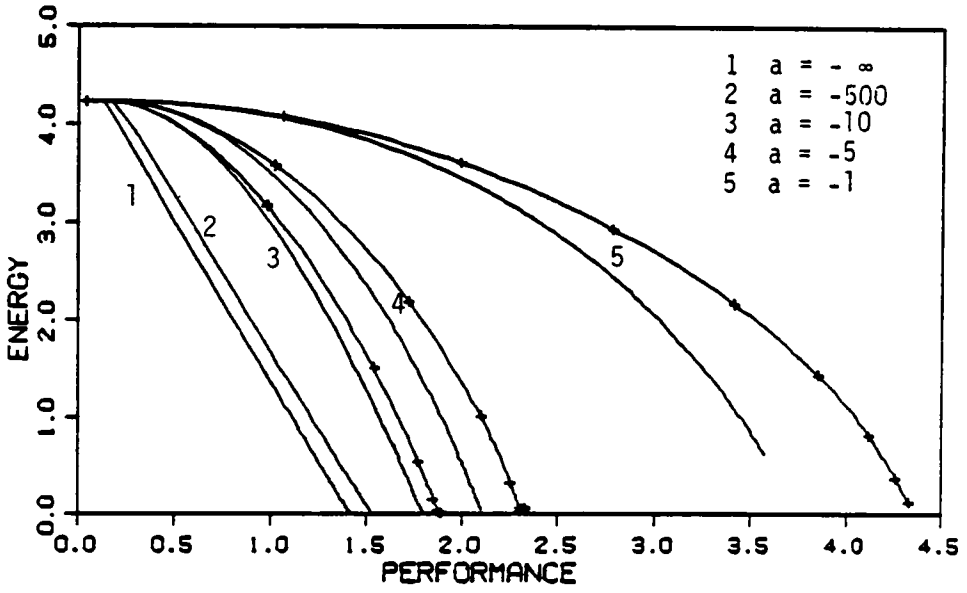

b) R = 0.1, g = 1.0.

Figure 8.23 Natural control of an impulse response with various actuator responses.

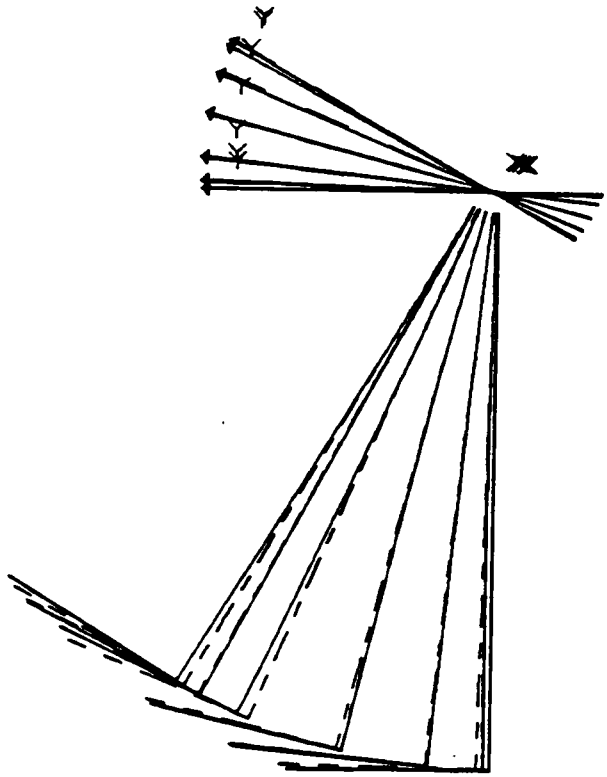

a) Actuators on shuttle

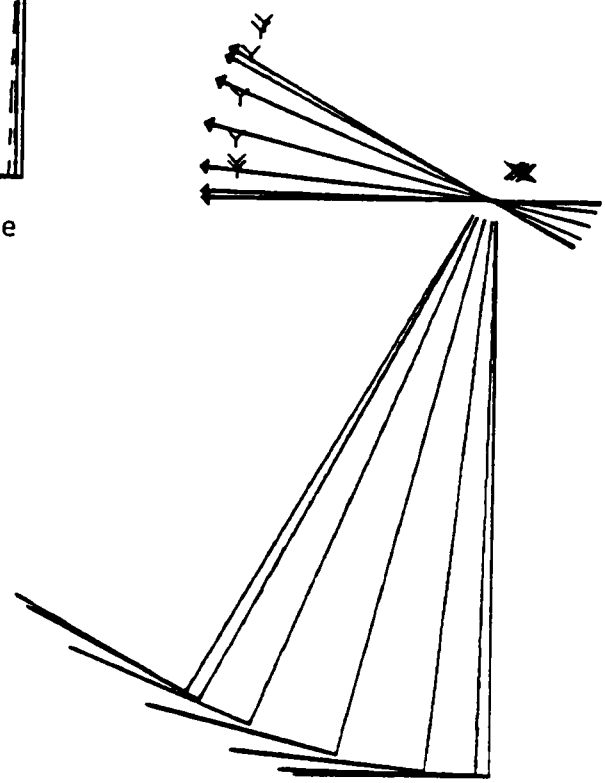

b) Distributed actuators

Figure 8.24 Time-lapse plots of 30° roll maneuver, FACT = 1.0.

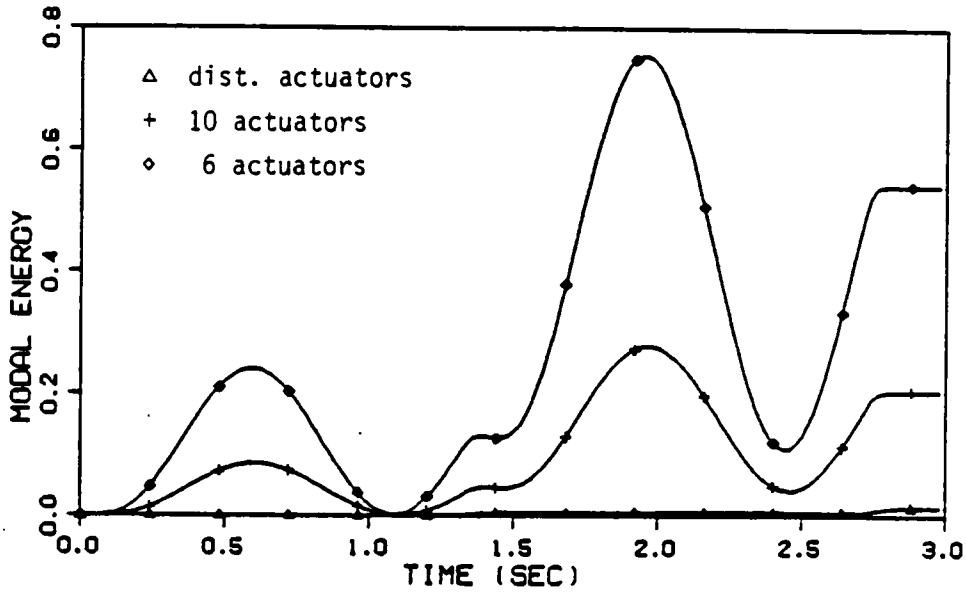

Figure 8.25 Vibration energy during 30° maneuver with various numbers of actuators.

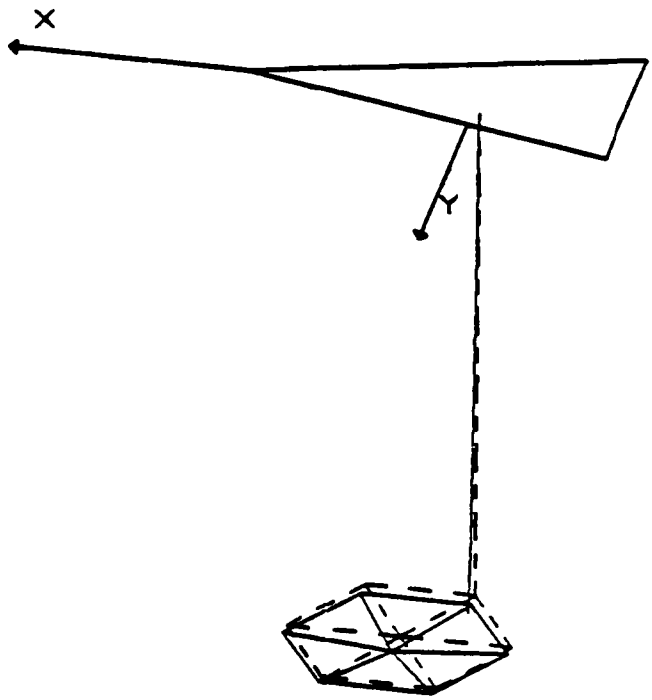

Figure 8.26 Maneuver control force distribution, FACT = 7.5.

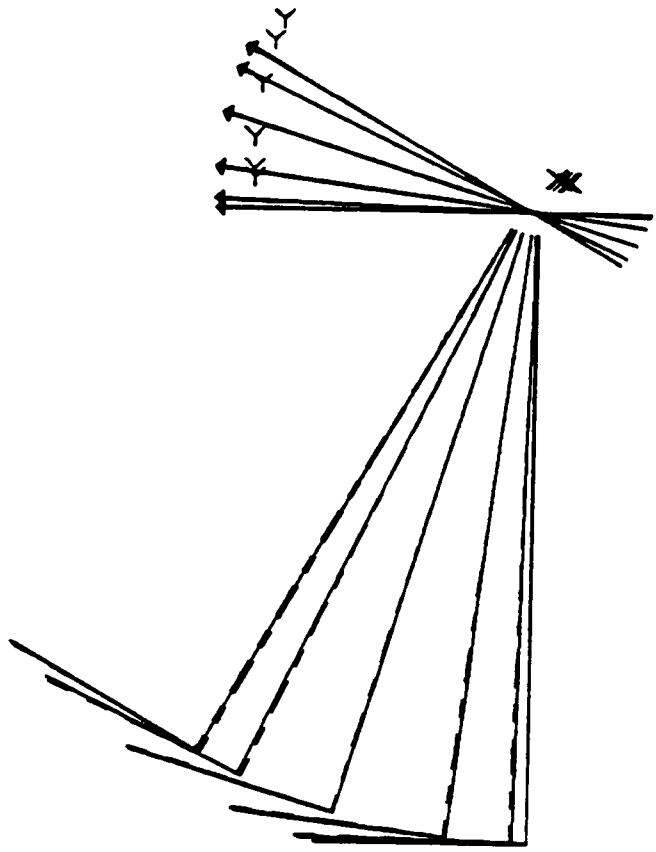

Figure 8.27 Time-lapse plot of 30° roll with uniform damping control using 10 actuators, FACT = 1.0.

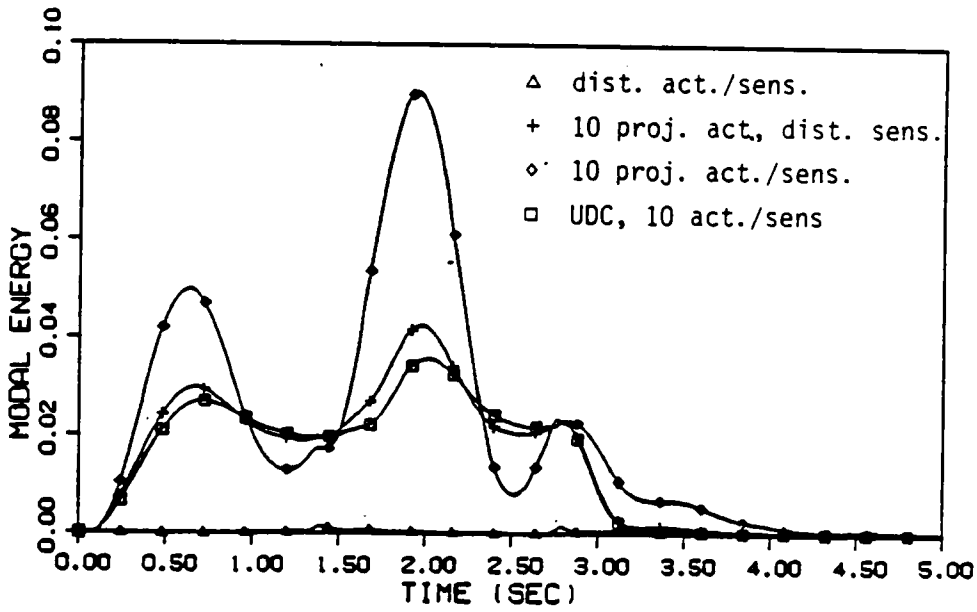

a) Energy

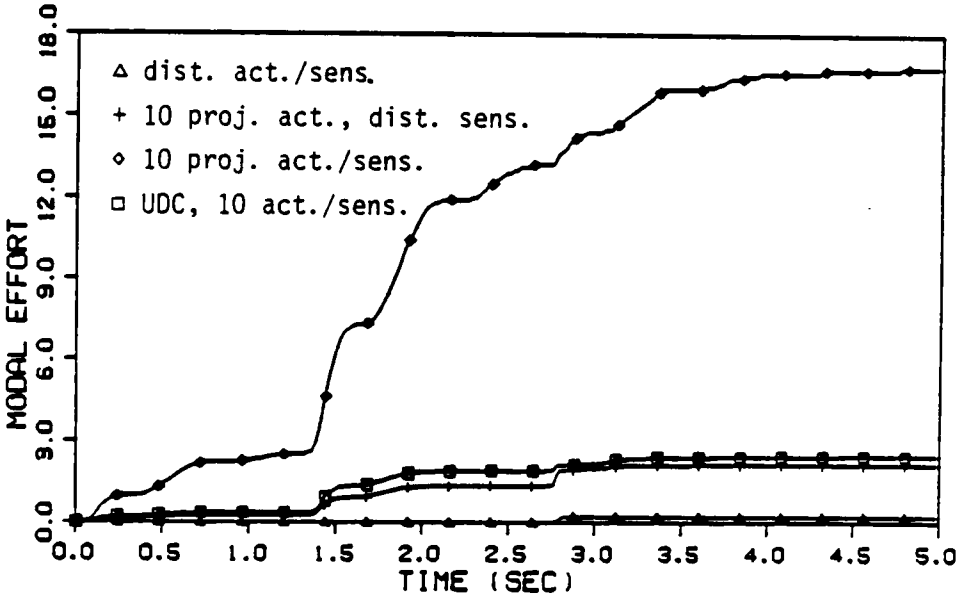

b) Effort

Figure 8.28 Comparison of various control implementations for 30° maneuver.

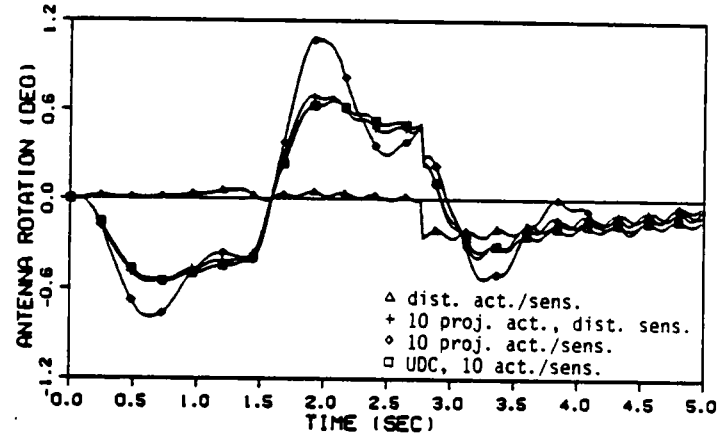

a) x_0 direction

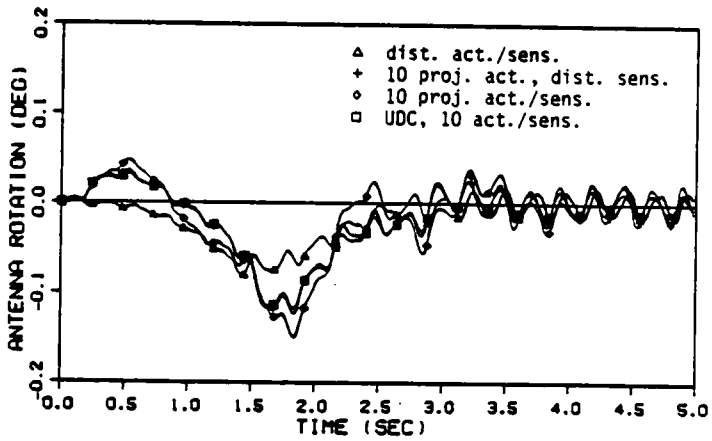

b) y_0 direction

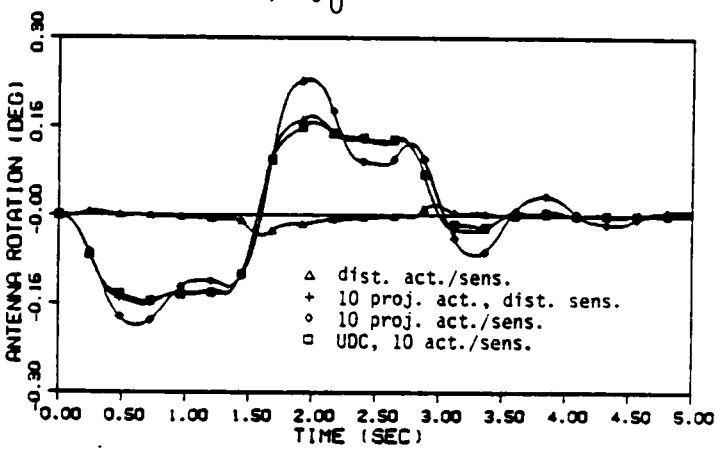

c) z_0 direction

Figure 8.29 Antenna hub rotations during 30° maneuver.

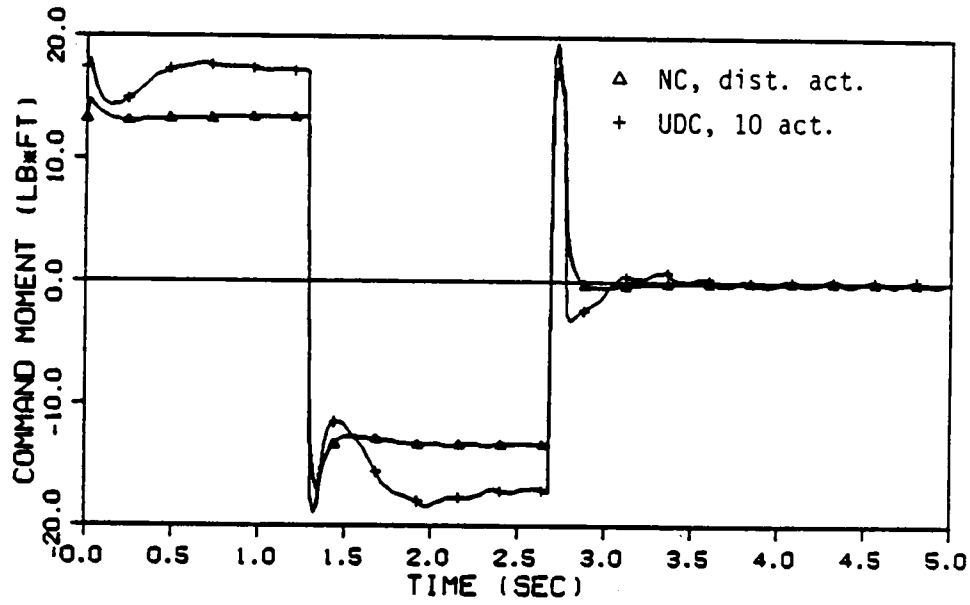

Figure 8.30 Torque on shuttle in x_0 direction during 30° roll.

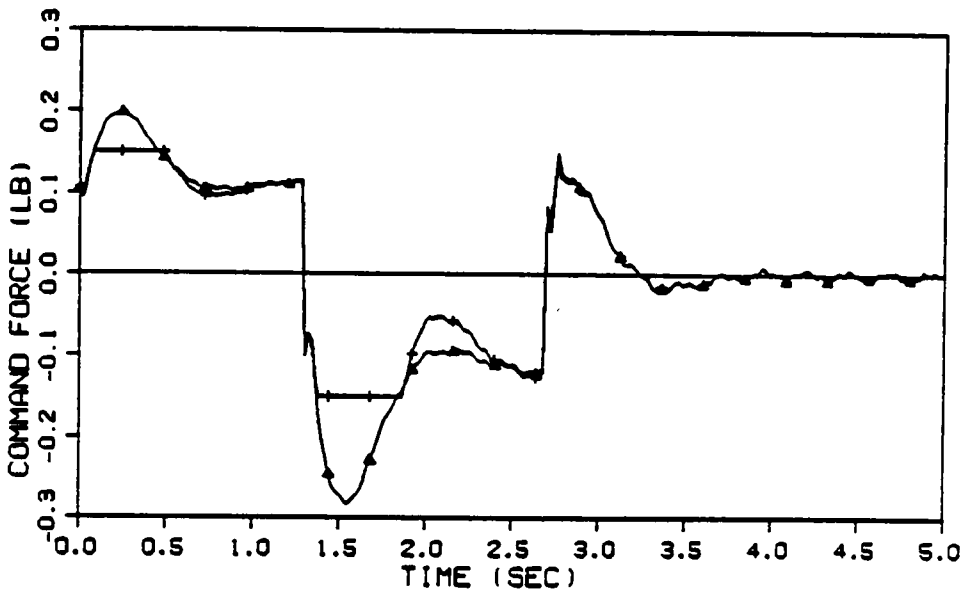

Figure 8.31 Force on antenna hub in y_0 direction, with and without thruster saturation.

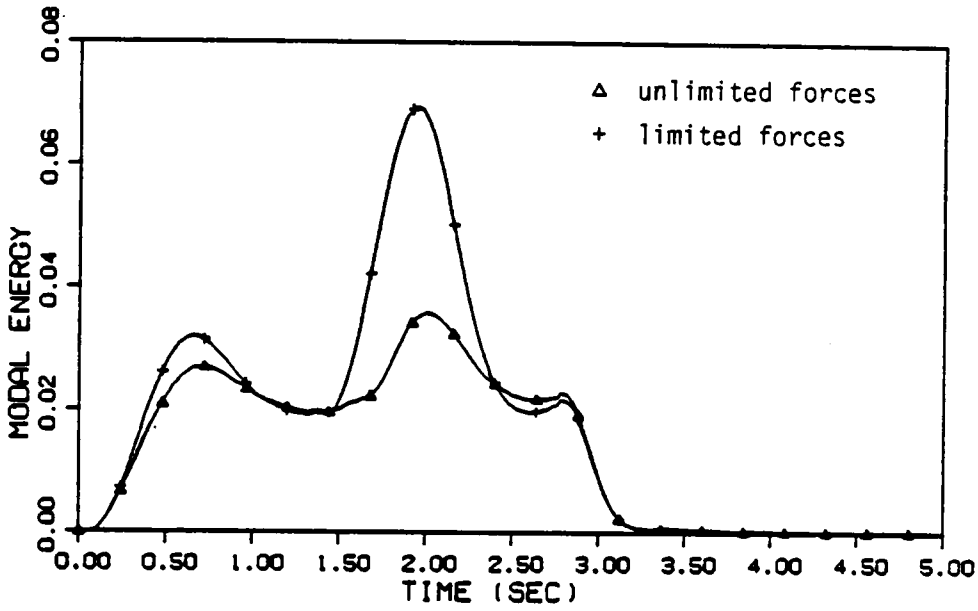

a) Energy

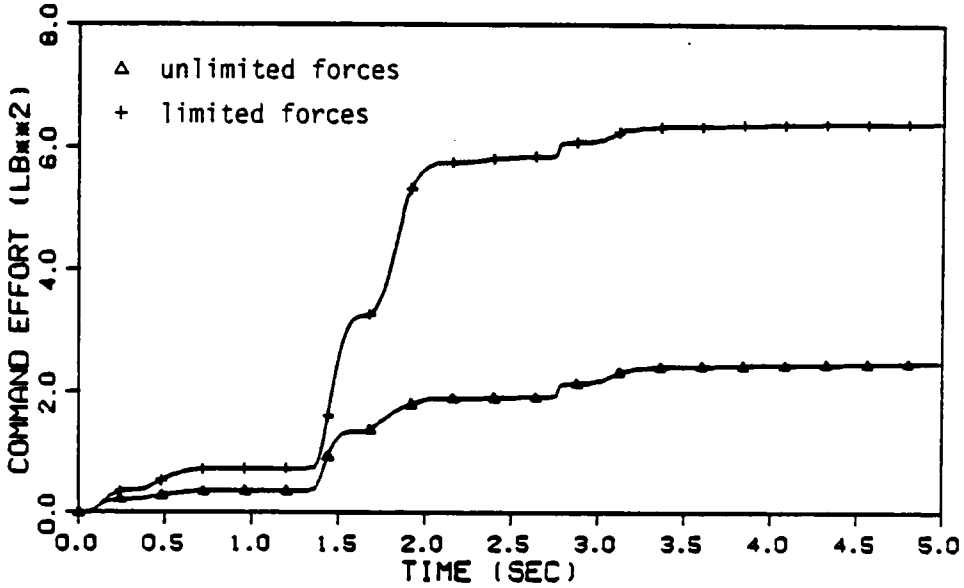

b) Effort

Figure 8.32 Effects of actuator saturation with uniform damping control during 30° maneuver.

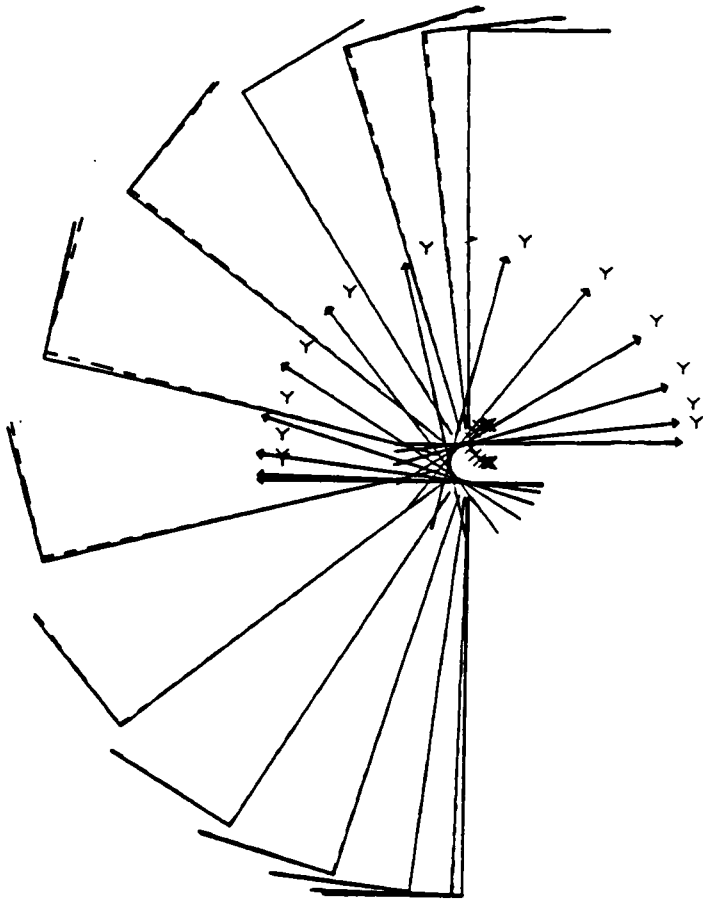

a) Time-lapse plot, FACT = 1.0

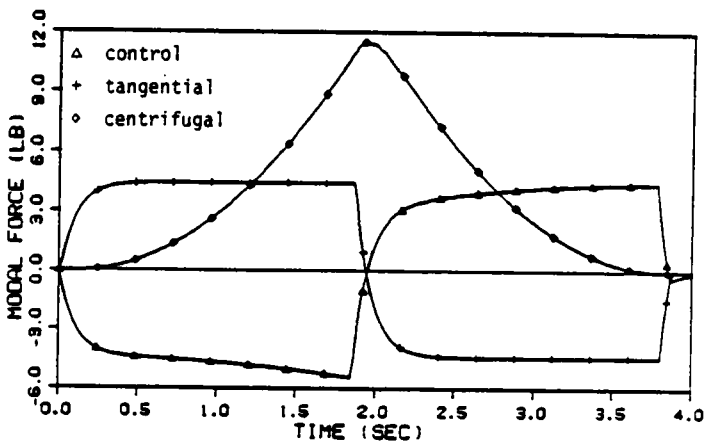

b) Modal disturbance and control forces

Figure 8.33 Excitation of structure by centrifugal force during 180° roll.

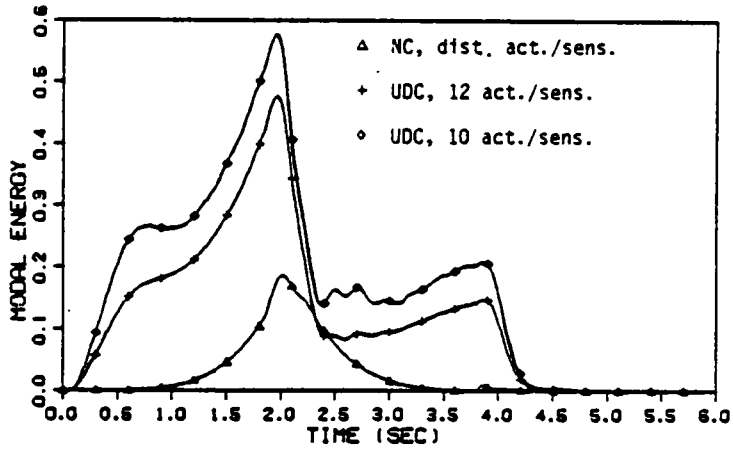

a) Energy

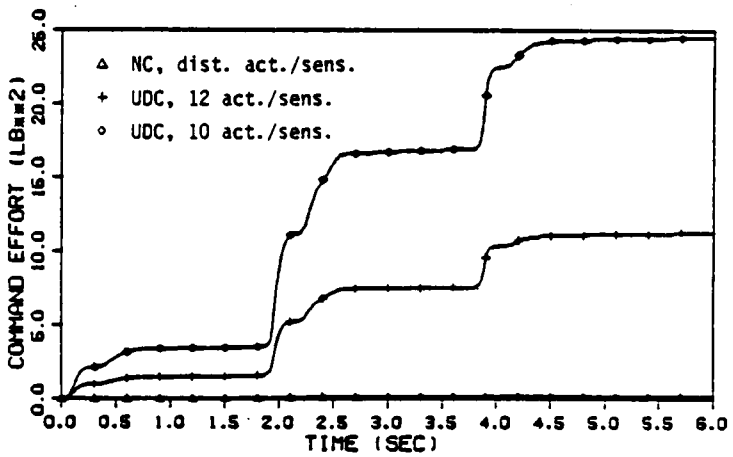

b) Effort

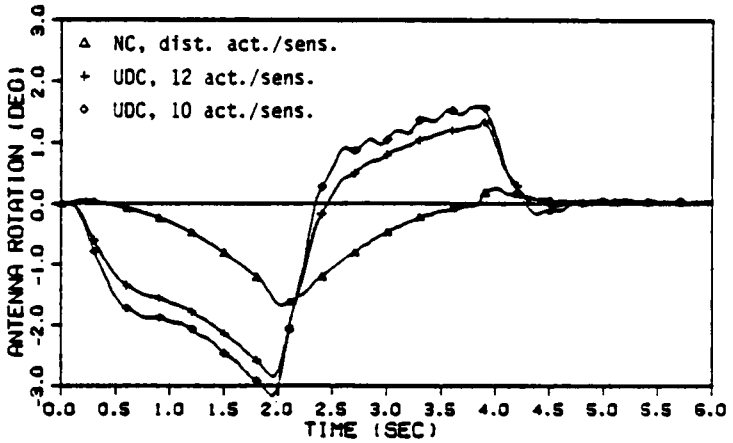

c) Antenna hub rotation in x_0 direction

Figure 8.34 Control of 180° maneuver with various numbers of Actuators.

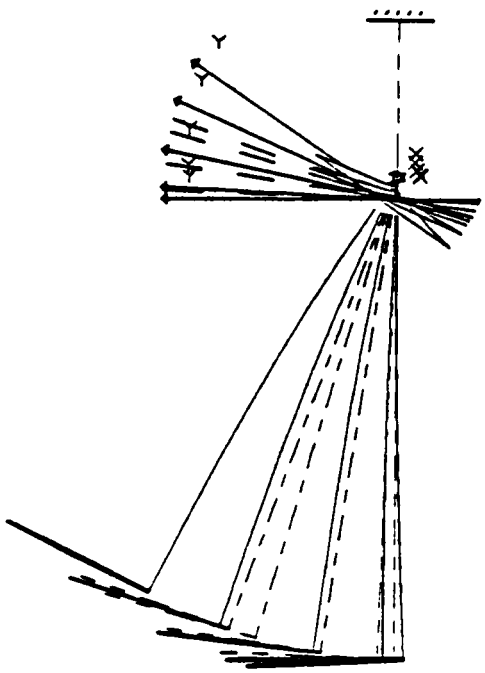

a) Actuators on shuttle, gravity included in maneuver policy

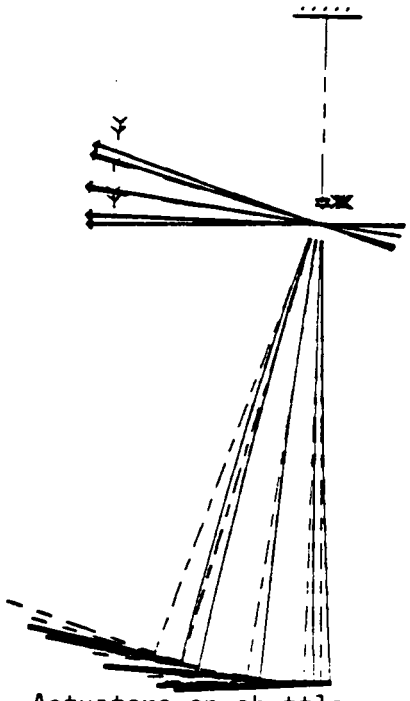

b) Actuators on shuttle, gravity neglected in maneuver policy

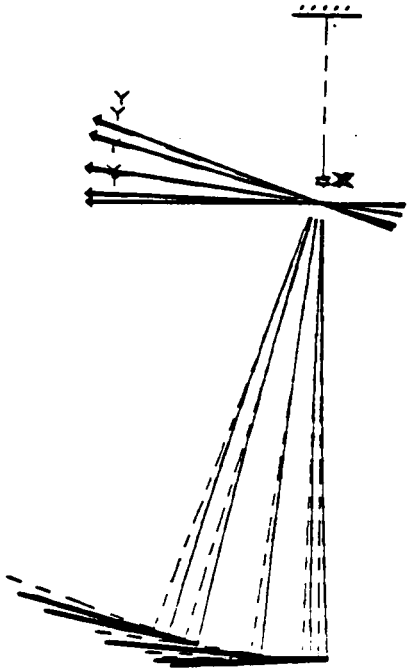

c) Natural control

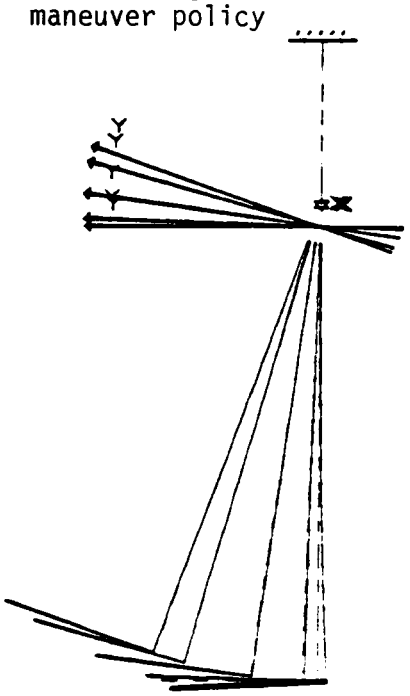

d) Distributed shape and natural controls

Figure 8.35 Time-lapse plots of 20° maneuver in laboratory, FACT = 1.0.

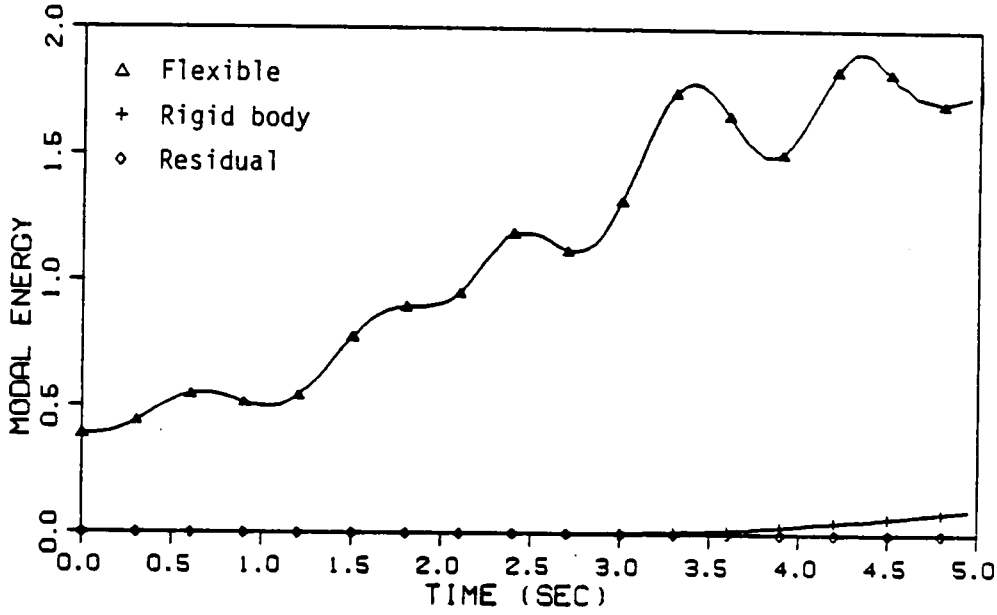

a) Maneuver control only

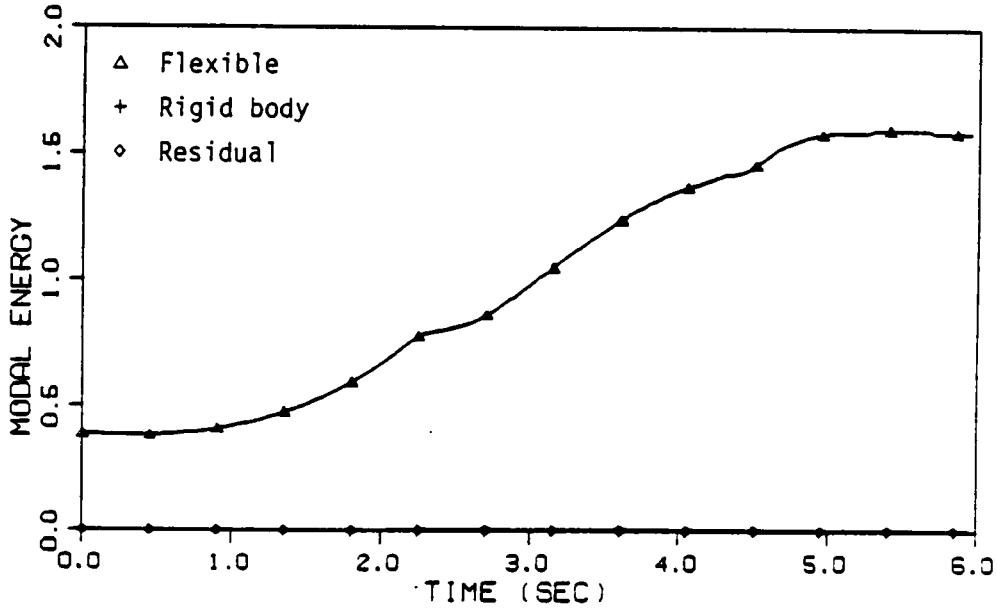

b) Natural control

Figure 8.36 Energy during 20° roll maneuver.

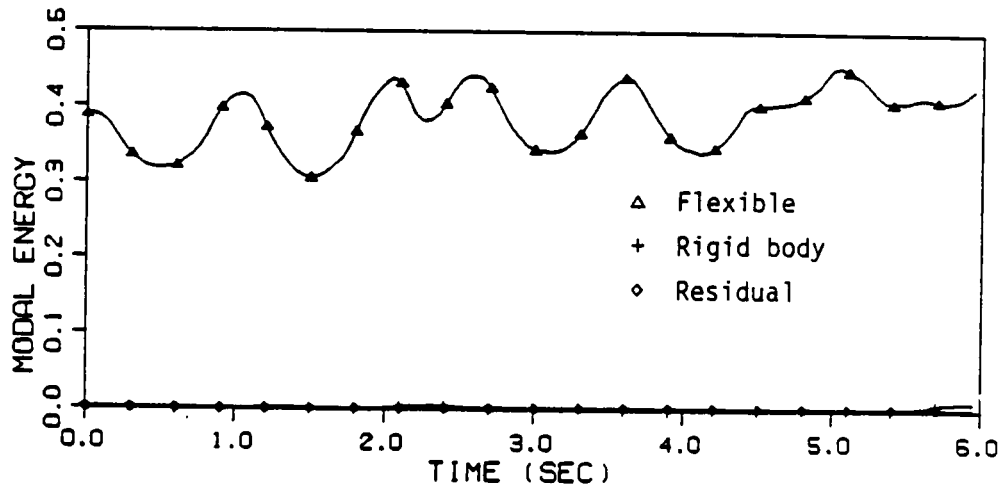

a) Energy

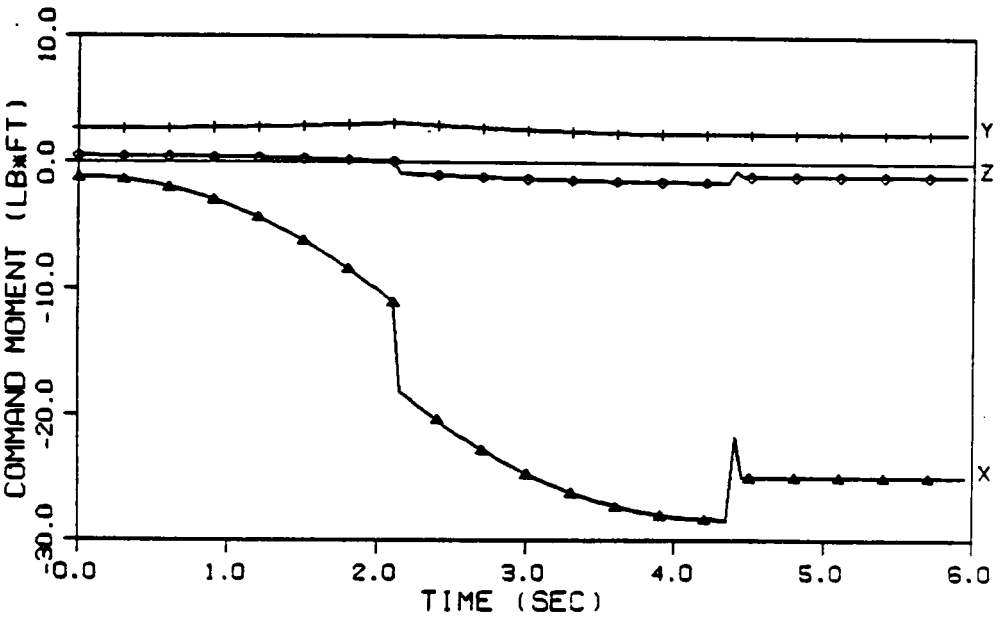

b) Command moments on shuttle

Figure 8.37 Distributed shape control opposing gravity during 20° maneuver.

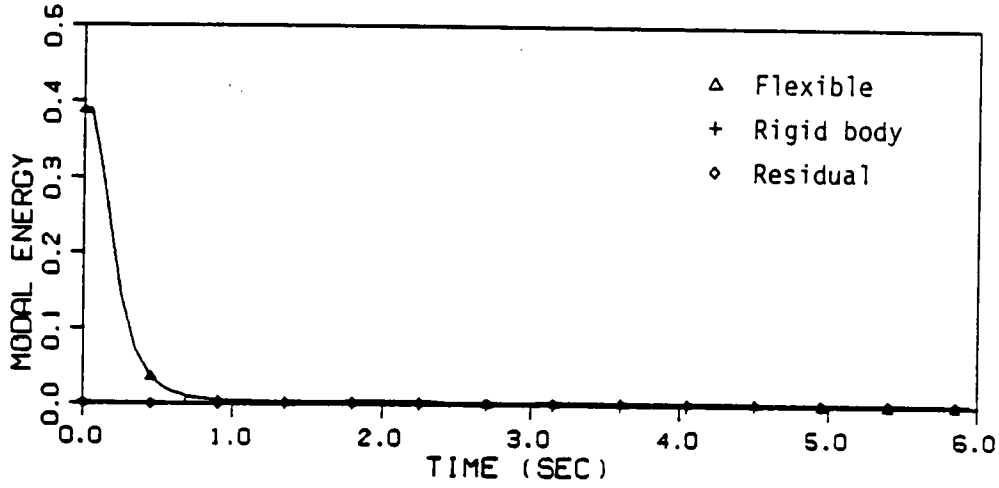

a) Energy

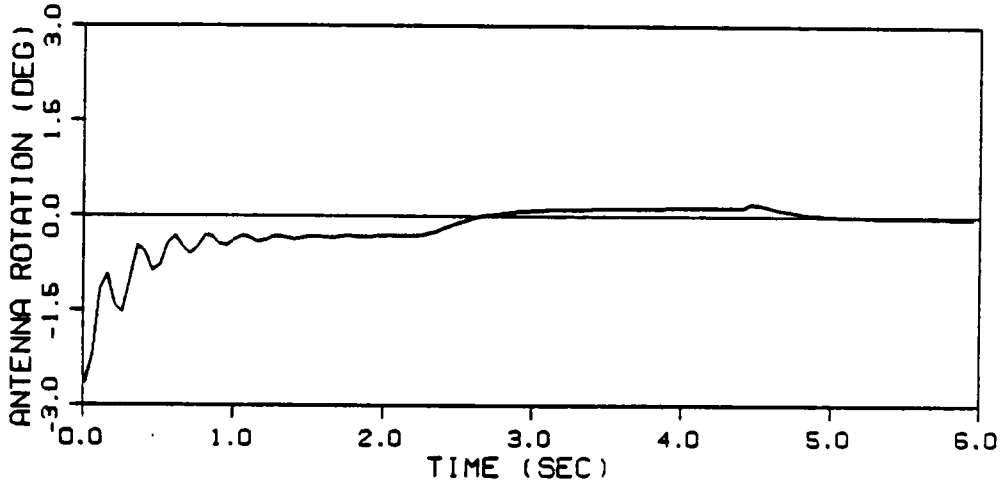

b) Rotation of antenna hub in x_0 direction

Figure 8.38 Distributed shape and natural control applied during 20° maneuver.

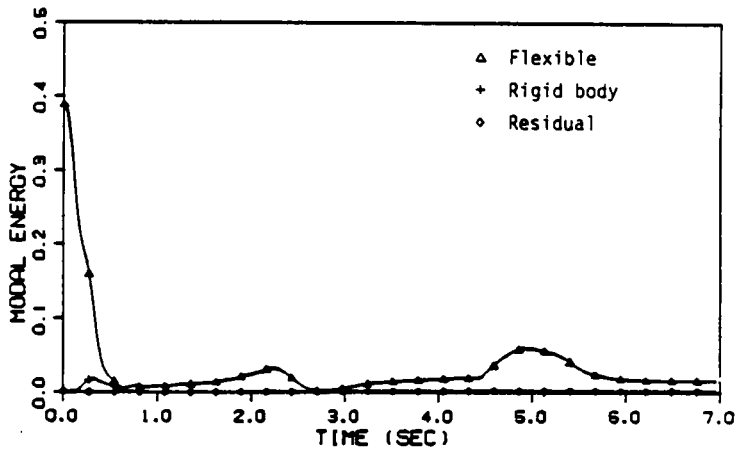

a) Energy

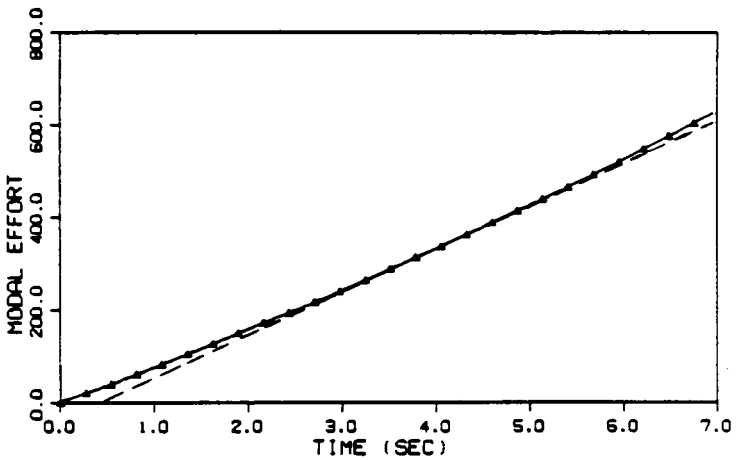

b) Effort

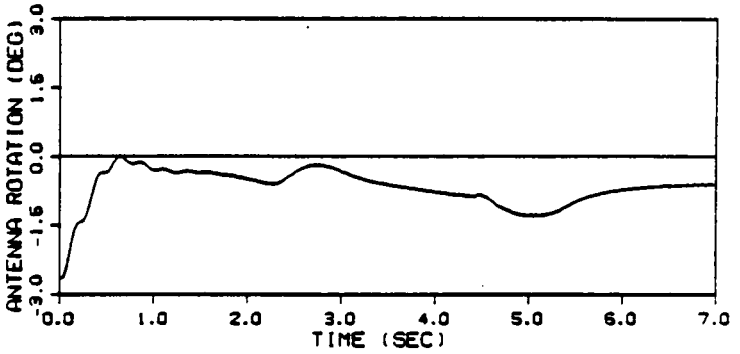

c) Antenna hub rotation in x_0 direction

Figure 8.39 Projected control of 20° roll with R decreased at t=5.0 s.

CHAPTER IX

SUMMARY AND CONCLUSIONS

The equations of motion were developed for a flexible structure undergoing a maneuver both in the space environment and in an earth based laboratory. The equations are nonlinear due to the large rigid-body maneuver. Although the structure is assumed to consist of a rigid-body with a flexible appendage attached, the analysis can be easily extended to include multiple appendages.

Using a perturbation approach, the nonlinear equations of motion are transformed into a set of equations governing the rigid-body motions and a set of time-varying, linear equations governing small deviations from the prescribed rigid-body maneuver. The time-varying coefficients of the first-order equations are known as soon as the rigid-body maneuver history has been determined. The first-order equations are nonself-adjoint. The mass matrix is time invariant for the structure in space and also for the laboratory model if the mass of the tether is neglected. This is equivalent to neglecting the tether's higher bending modes, which is reasonable since the higher bending modes of the cable involve little "spacecraft" participation.

A least-squares approach to substructure synthesis is developed as a method of discretization and truncation of the equations of motion for efficient eigensolution. This method allows for simple, robust and computationally efficient assembly of the global mass and stiffness matrices. The admissible vectors are applied in a least-square sense but connectivity of the substructure is satisfied exactly. A reduction

of system order is accomplished while relative accuracy of the lower modes is maintained.

Adding an admissible vector to a substructure is equivalent to adding a degree of freedom to that substructure. The placement of an admissible vector involves the particular substructure to which it is added as well as the direction of the additional degree of freedom. The placement of admissible vectors is as important for the accuracy of a particular mode as their quantity and type because different modes involve participation of different substructures. A self-adaptive computer technique is recommended to place the admissible vectors to produce the desired accuracy for particular modes with the minimum of degrees of freedom.

A simple open-loop control strategy for minimum-time, single-axis rotational maneuvers of a rigid-body is presented. The control strategy is developed for continuous time and adapted to discrete-time. The discrete-time switching times are chosen to minimize the difference between the trajectories generated from discrete and continuous switching times. If the sampling time is small compared to the total maneuver time the error resulting from the discrete-time switching is small. The maneuver solution need not be stable since the closed-loop vibration control can stabilize the maneuver as well as correct errors arising from the discrete-time switching strategy. If the maneuver strategy is unstable, the zero-order and first-order simulations must be carried out simultaneously. However, the time-varying coefficients of the first-order equations are predetermined in any case.

The maximum available maneuver torques are determined by summing the maximum moments produced by each actuator in each direction. A portion of each actuator's output should be reserved for vibration control, and shape control if needed.

The simulation technique of Chapter 6 is readily programmable and relatively efficient in terms of both computer storage and CPU time. The operations required at each sampling time are minimized by using the fact that the maneuvers are single-axis rotations. The premaneuver eigenvectors are excellent admissible vectors for reduction of system order for both simulation and control of the spacecraft. These vectors do not decouple the equations of motion, but they do reduce the order of the system and diagonalize the mass matrix. Hence, inversion of the mass matrix is trivial, so that formulating the reduced-order equations in state-space form requires little effort.

The vibration problem during the maneuver is nonself-adjoint and the eigensolution is time varying. Physically, this means that the equilibrium configuration does not correspond to the intial configuration during the maneuver and varies with time. A more severe maneuver produces greater fluctuations of the eigenvalues. The maneuver control forces sometime increase and at other times dissipate the vibrational energy while producing the desired rigid-body maneuver. Hence, the vibrational energy fluctuates during the maneuver.

Distinctions have been made between maneuver, vibration and shape controls. Maneuver control is of zero-order and produces large rigid-body motions of the structure. Shape control opposes a steady-state, or

slowly varying force to maintain, approximately, a certain mean configuration. Hence, shape and vibration controls effectively add stiffness and damping to the structure, respectively. Maneuver control can be implemented so that it acts as a shape control, as shown in Chapter 5. Also, typical methods of controlling vibration include feedback on the displacement and, thus, produce some shape control.

There are three types of disturbance forces on the right side of Eq. (3.14), each of which excites the modes of the spacecraft. The first two terms results from tangential and centrifugal accelerations of the body-fixed frame and the last term results from the acceleration due to gravity. If the open-loop maneuver control is implemented with distributed forces proportional to the corresponding rigid-body modes, these forces cancel the tangential force and part of the centrifugal force. Shape control, implemented with distributed actuators, cancels the gravitational disturbance force, which is unique to the laboratory experiment. However, when these controls are implemented with discrete actuators, the tangential and gravitational disturbance forces are not completely cancelled and, along with the remaining portion of the centrifugal force, cause vibration and steady-state error. Hence, closed-loop vibration control must be used to suppress these disturbances.

The force distributions for both the maneuver and the uniform-damping vibration controls depend exclusively on the mass matrix. Since the mass matrix is time-invariant, these control formulations are not affected during the maneuver and, hence, are robust.

The inclusion of actuator dynamics along with the structure's dynamics is beneficial for both maneuver and vibration control. The relative magnitude of the actuator response decay rate compared to the decay rate of vibration control and mean velocity of the maneuver determines the degree of these benefits. If the actuator decay rate is large relative to the control rate, inclusion of the actuator dynamics is not crucial. The actuator dynamics smooths the applied control force history. Hence, the maneuver acceleration history is not discontinuous, which is fortunate in that it causes less excitation of the elastic modes of the structure.

Increasing the number of actuators decreases the amount of vibrational energy input to the structure during a maneuver. In fact, the addition of just a few actuators in optimal locations can greatly reduce the vibrational energy. Independently of this, increasing the number of actuators also decreases the vibration control effort. The smallest number of actuators necessary to control a three-dimensional structure is six. For a particular problem, the performance requirements determine the necessary number of actuators. As these requirements become more stringent, the required number of actuators increases. The placement of the actuators is critical in minimizing the necessary quantity for a particular performance. It was shown that points of maximum inertia are the optimal locations for actuators for the maneuver, shape and uniform-damping vibration controls.

Uniform damping control provides excellent performance for vibration control even during severe maneuvers. This is not surprising

since it is actually an approximation of natural control implemented with discrete actuators and distributed sensors. Uniform damping control has the advantage of being easy to implement, provided that collocated actuators and sensors are available. This control is decentralized so that modal estimation is not necessary, and all modes are controlled so that control spillover is eliminated.

Natural control approximated with distributed actuators remains effective during actuator saturation. However, the price is decreased energy dissipation and increased effort requirements.

Gravity strongly affects the laboratory experiment. The natural frequencies change with the structure's orientation relative to the direction of gravity. For safety, the structure should be stable throughout the maneuver. However, the price of greater stability is increased effort to counteract the gravity torque. Hence, a stability analysis is crucial to determine the optimal universal joint location for the desired maneuver. An alternative to opposing the gravity torque is to maneuver about the axis of the tether.

Shape control applied with discrete actuators results in a steady-state error. After the maneuver has been completed and the vibration has been suppressed, natural control can be used as a supplemental shape control. This is done by increasing the gains incrementally to reduce the steady-state error and lock the antenna on target.

Precise shape control may not be feasible for the laboratory experiment because of the large amount of effort and great number of

actuators required. An alternative is to allow the appendage to deform under gravity, maintaining only vibration control.

In the laboratory experiment, the deformation of the appendage strongly affects the magnitude of the forces necessary to counterbalance gravity. If it is desirable to maintain the shape of the structure during the maneuver, the minimum-time maneuver strategy should be formulated to include gravity. Then, the maneuver force can provide all the necessary shape control.

Shape control of the entire structure has been implemented. Actually, the control task of highest priority is aiming the antenna. The shape of the mast is not critical, provided its deformation remains within reasonable limits. A strategy providing control of the orientation and shape of the antenna only may result in a reduction of the control effort.

The main objective of slewing a three-dimensional spacecraft while maintaining vibration control has been achieved. Since the vibrations are suppressed during the maneuver, terminal constraints need not be imposed. The separation of the maneuver and vibration control formulations annihilates the numerical difficulties encountered by the authors of the papers cited in Sec. 1.2. Hence, there is essentially no limit to the number of modes that can be controlled, permitting more severe maneuvers. Also, since the maneuver strategy is independent of the vibration control, any type of rigid-body maneuver policy is possible.

REFERENCES

1. Arbel, A. and Gupta, N. K., "Robust Collocated Control for Large Flexible Space Structures," Journal of Guidance and Control, Vol. 4, Sept. - Oct. 1981, pp. 480-486.

2. Baruh, H. and Silverberg, L., "Implementation Problems Associated with Simultaneous Maneuver and Vibration Suppression of Flexible Spacecraft," presented at the Fifth VPI&SU/AIAA Symposium, Blacksurg, Virginia, June 1985.

3. Baruh, H. and Silverberg, L., "Maneuver of Distributed Spacecraft," presented at the Guidance and Control Conference, Seattle, WA, Aug. 20-22, 1984.

4. Breakwell, J. A., "Optimal Feedback Slewing of Flexible Spacecraft," Journal of Guidance and Control, Vol. 4, Sept. - Oct. 1981, pp. 472-479.

5. Craig, R. R. and Bampton, M. C. C. "Coupling of Substructures for Dynamic Analysis," AIAA Journal, Vol. 6, No. 7, July 1968, pp. 1313-1319.

6. Dynamics and Control of Large Structures, proceedings of the VPI&SU/AIAA Symposia, held in Blacksburg, Virginia, 1977-85.

7. Hale, A. L. and Rahn, G. A., "Robust Control of Self-Adjoint Distributed-Parameter Structures," Journal of Guidance and Control, Vol. 7, No. 3, 1984, pp. 265-273.

8. Junkins, J. L. and Turner, J. D., "Optimal Continuous Torque Attitude Maneuvers," Journal of Guidance and Control, Vol 3, May - June 1980, pp. 210-217.

9 Junkins, J. L., "Comment on 'Optimal Feedback Slewing of Flexible Spacecraft'," Journal of Guidance and Control, Vol. 5, May - June 1982, pg. 318.

10. Kirk, D. E., Optimal Control Theory, Prentice-Hall, Inc., Englewood Cliffs, NJ, 1970.

11. Meirovitch, L., Analytical Methods in Vibration, The Macmillan Co., New York, NY, 1967.

12. Meirovitch, L., Methods of Analytical Dynamics McGraw-Hill Book Company, New York, 1970.

13. Meirovitch, L., Computational Methods in Structural Dynamics, Sijthoff-Noordhoff Co., The Netherlands, 1980.

14. Meirovitch, L. and Baruh, H., "Control of Self-Adjoint Distributed-Parameter Systems," Journal of Guidance and Control, Vol. 5, Jan. - Feb. 1982, pp. 60-66.

15. Meirovitch, L. and Hale, A. L., "A General Dynamics Synthesis for Structures with Discrete Substructures," Journal of Sound and Vibration, Vol, 85, 1982, pp. 445-457.

16. Meirovitch, L. and Silverberg, L. M., "Globally Optimal Control of Self-Adjoint Distributed Systems," Optimal Control Applications and Methods, Vol. 4, 1983, pp. 365-386.

17. Meirovitch, L. and Baruh, H., "On the Robustness of the Independent Modal-Space Control Method," Journal of Guidance, Control, and Dynamics, Vol. 6, No. 1, 1983, pp. 20-25.

18. Meirovitch, L., Baruh, H. and Oz, H., "A Comparison of Control Techniques for Large Flexible Systems," Journal of Guidance, Control and Dynamics, Vol. 6, No. 4, July-August 1983, pg. 302.

19. Meirovitch, L. and Baruh, H., "On the Implementation of Modal Filters for Control of Structures," AIAA Guidance and Control Conference, August 20-22, 1984, Seattle, WA.

20. Meirovitch, L., Introduction to Dynamics and Control, John Wiley & Sons, Inc., New York, NY, 1985.

21. Meirovitch L. and Silverberg, L., "Control of Non Self-Adjoint Distributed-Parameter Systems," Journal of Optimization Theory and Applications, Vol. 47, No. 1, September 1985.

22. Montgomery, R. C. and Sundarajan, N., "Identification of the Dynamics of a Two-Dimensional Grid Structure Using Least Square Lattice Filters," 1984 American Control Conference, San Diego, CA, June 6-8, 1984.

23. Norris, M. A., "On the Implementation of the Independent Modal-Space Control Method," Masters Thesis, VPI&SU, 1985.

24. Silverberg, L., "Uniform Damping Control of Spacecraft," presented at the Fifth VPI&SU/AIAA Symposium, Blacksburg, Virginia, June 1985.

25. Turner, J. D., "Optimal Large Angle Maneuvers for Large Flexible Space Structures," Ph.D Dissertation, VPI&SU, 1980.

26. Turner, J. D. and Junkins, J. L., "Optimal Large-Angle Single-Axis Rotational Maneuvers of Flexible Spacecraft," Journal of Guidance and Control, Vol. 3, Nov. - Dec. 1980, pp. 578-585.

27. Turner, J. D. and Chun, H. M., "Optimal Distributed Control of a Flexible Spacecraft During a Large-Angle Maneuver," Journal of Guidance and Control, Vol. 7, May - June 1984, pp. 257-264.

The vita has been removed from the scanned document